

https://dspace.org/

Thermodynamic study of carbon nanotube production from greenhouse gases during syngas synthesis

Maphutha, Selby Kwena

2010-07-26T08:27:06Z
http://hdl.handle.net/10539/8302

Downloaded from a DSpace repository. https://dspace.org/

THERMODYNAMIC STUDY OF CARBON NANOTUBE PRODUCTION FROM GREENHOUSE GASES DURING SYNGAS SYNTHESIS

SELBY KWENA MAPHUTHA

A dissertation submitted to the Faculty of Engineering and the Built Environment, University of the Witwatersrand, in fulfilment of the requirement for the Degree of Master of Science in Engineering.

Johannesburg,
2009

DECLARATION

I declare that this dissertation is my own, unaided work. It is being submitted for the degree of Master of Science in the University of Witwatersrand, Johannesburg. It has not been submitted before for any degree or examination in any other University.

_____

(Signature of candidate)

_____ Day of _____

ABSTRACT

Global warming has become a major topic for the public in recent years and many institutions and industries have been pushed to find a ‘cure’ for it. The most wildly known culprit for global warming is carbon dioxide and several methods for the treatment of this gas have been proposed. There is thermal decomposition, capturing methods and chemical decomposition. This study looks at the conversion of carbon dioxide and another greenhouse gas, methane, into carbon nanotubes and syngas (hydrogen and carbon monoxide), which is a precursor to the petroleum compounds in the Fischer-Tropsch process. The study was done experimentally by running a $CO_2\backslash CH_4$ mixture through a CVD reactor, at temperatures ranging from 650 to 950°C, and two catalysts (a lanthanum-nickel alloy and a mischmetal-nickel alloy separately). Theoretically, the thermodynamics of this process were done at temperatures ranging from 600 to 1500 K. The products from the experiment were analysed using a Transmission electron microscope (both normal and high resolution), Raman spectroscopy and Gas chromatography. Using the proposed catalysts, the carbon dioxide and the methane were decomposed, forming carbon nanofibers and carbon nanotubes as shown by the transmission electron microscope images. The carbon nanofibers and nanotubes became less defined and generally fewer in number as the temperature increased. The thermodynamics also showed that the carbon decreased and the syngas increased as the temperature increased. The Gas chromatography showed that there was syngas that was produced during the experimental process. The mischmetal-nickel alloy proved to convert more of the greenhouse gasses into syngas than the lanthanum-nickel alloy.

DEDICATION

This dissertation is dedicated to my family who have stood by me throughout everything.

ACKNOWLEDGEMENTS

The work presented in this thesis was made possible due to the assistance of a number of people and institutions. I would like to express my sincere gratitude to the following:

My family for their unconditional love and support.

Prof. S.E. Iyuke for his support throughout my research.

The NRF and Centre of Excellence - SM for funding my research.

I would also like to thank Sasol Ltd. for their financial support during my postgraduate studies.

The Raman Unit and the Microscopy Unit.

0

Table of Contents

DECLARATION i
ABSTRACT ii
DEDICATION iii
ACKNOWLEDGEMENTS iv
LIST OF FIGURES vii
LIST OF TABLES ix
CHAPTER ONE 1
1.0 Introduction 1
1.1. Background and motivation 1
1.2. Aim and Objectives 2
1.3. Research Questions 2
1.4. Hypothesis 2
1.5 Dissertation outline 3
CHAPTER TWO 4
2.0 Literature Review 4
2.1. Carbon Nanotechnology and Theory 4
2.1.1. Structure of Carbon nanotubes 4
2.1.2. Properties 9
2.1.3. Growth models 10
2.1.4. Production 22
2.1.5. Carbon dioxide decomposition 27
2.1.6. Reforming 28
2.1.7. Analysis Equipment 30
2.2. Thermodynamics 34
2.2.1. Equilibrium Thermodynamics 34
2.2.2. Equilibrium Thermodynamics for system 38
CHAPTER THREE 42
3.0 Methods and Procedure 42
CHAPTER FOUR 47
4.0 Results and Discussion 47
4.1. Results 47
4.1.1. TEM Images of Carbon Nanofibres (CNFs) produced with CO_2 47
4.1.2. TEM images of CNTs produced with Methane 51
4.1.3. Images obtained when CO_2 reforming of CH_4 has taken place 53

4.1.4. Gas Chromatography Analysis 57
4.1.5. Raman Spectrometer Analysis 59
4.1.6. Thermodynamics 61
4.2. Discussion 63
CHAPTER FIVE 66
5.0 Conclusion and Recommendations 66
5.1. Conclusion 66
5.2. Recommendations 66
References 68
Appendix 1: Mathcad calculations 75
Appendix 2: TEM Images 86
Appendix 3: Raman Results 92
Appendix 4: Data for Thermodynamic Plots 98

LIST OF FIGURES

Page
Figure 2. 1: The different structures of carbon. (Hoffman, W. P., 2005) 5
Figure 2. 2: The C_{60} fullerene and carbon nanotube. (Hoffman, W. P., 2005) 5
Figure 2. 3: The different regions of a nanotube. (Daenen et. al., 2003) 6
Figure 2. 4: Graphene sheet being rolled into a nanotube. 6
Figure 2. 5: Chiral vector for a (2, 4) nanotube. (Belin and Epron, 2005) 7
Figure 2. 6: The different models describing nanotubes: a) coaxial cylindrically curved, b) coaxial polygonized and c) scroll. (Belin and Epron, 2005) 7
Figure 2. 7: The different types of CNTs a) zigzag, b) armchair and c) chiral 9
Figure 2. 8: Spherical metal cluster on substrate (Shibuta and Elliot, 2006) 12
Figure 2. 9: Deposition of carbon atoms on surface of SWCNT (Louchev et al., 2004) 13
Figure 2. 10: Long SWCNT where length, L, is higher than the characteristic surface diffusion length, λ_D 14
Figure 2. 11: Illustration of carbon loops and their equivalent form. (Vaezzadeh et al., 2005) 20
Figure 2. 12: Illustration of CNT growth system: a) loop equivalent form; b) growth equivalent form. (Vaezzadeh et al., 2005) 21
Figure 2. 13: Arc discharge setup showing 2 graphite electrodes which are used to produce an electric arc discharge in an inert gas atmosphere. (Popov, 2004) 23
Figure 2. 14: Laser ablation schematic depicting a laser beam which vapourises a target consisting of a mixture of graphite and a metal catalyst. (Popov, 2004) 24
Figure 2. 15: a) Homogenous horizontal CVD b) Heterogeneous horizontal CVD. (Philippe, 2007) 26
Figure 2. 16: a) Standard fluidised bed CVD reactor, b) fluidised bed CVD reactor with gas pre-heating, c) vibro-fluidised-bed reactor. (Philippe, 2007) 26
Figure 2. 17: Phase boundary curves for the dissociation of CO_2. 28
Figure 2. 18: Transmission Electron Microscope with a schematic diagram of the inside. 30
Figure 2. 19: Example of actual Raman data that is characteristic to CNTs. (Dresselhaus et. al., 2004) 31
Figure 2. 20: Simplified schematic representation of a GC. 33

Figure 3. 1: Vertical CVD used for the experiments. 43

Figure 4. 1: CNFs produced at 750°C using Lanthanum-Nickel alloy. 47
Figure 4. 2: CNF produced at 850°C using Lanthanum-Nickel alloy. 47
Figure 4. 3: TEM image of the CNF on the nickel catalyst. 48
Figure 4. 4: CNF produced at 750°C using Platinum on alumina powder. 48
Figure 4. 5: Possible CNT from CO_2 source 48
Figure 4. 6: CNFs and CNTs produced at 650°C using Lanthanum-Nickel alloy. 49
Figure 4. 7: CNTs and CNFs produced at 700°C using Lanthanum-Nickel alloy. 49
Figure 4. 8: CNFs produced at 800°C using Mischmetal-Nickel alloy. 49
Figure 4. 9: CNTs produced at 750°C using Lanthanum-Nickel alloy. 51
Figure 4. 10: High resolution transmission electron microscope (HRTEM) image of the CNTs produced in Figure 4.8 above 51
Figure 4. 11: Very long CNT produced at 650°C using Lanthanum-Nickel alloy. 52
Figure 4. 12: HRTEM image of CNT produced at 650°C using Lanthanum-Nickel alloy. 52
Figure 4. 13: CNTs produced at 750°C using Lanthanum-Nickel alloy. 53

Figure 4. 14: Network of CNTs produced at 750°C using Mischmetal-Nickel alloy. 53
Figure 4. 15: CNT produced at 850°C using Mischmetal catalyst. 54
Figure 4. 16: CNT not fully formed. 54
Figure 4. 17: HRTEM image of the catalyst (dark spot) and the carbon deposition (grey). ... 55
Figure 4. 18: Few CNTs are produced at 950°C. 56
Figure 4. 19: The Raman Shifts of a) CNTs produced at 650°C using CO_2; b) CNTs produced at 750°C using CH_4; c) CNTs produced at 750°C during CO_2 reforming of CH_4. 59
Figure 4. 20: Raman Shift caused by the catalyst particles resembling that caused by the carbon products. 60
Figure 4. 21: Raman shift of sample when CNTs are not formed during reforming. 60
Figure 4. 22: Calculation 2 thermodynamic equilibrium compositions of a) carbon monoxide, b) hydrogen and c) carbon. 61
Figure 4. 23: Calculation 1 thermodynamic equilibrium compositions using different CO_2:CH_4 ratios. 62
Figure 4. 24: Composition of the catalyst particle after reforming. 64

Figure 1: CNFs produced at 750°C using Lanthanum-Nickel catalyst. 86
Figure 2: CNFs produced at 850°C using Lanthanum-Nickel catalyst. 87
Figure 3: a) CNFs; b) possible CNT at 700°C using Lanthanum-Nickel catalyst. 88
Figure 4: Hollow CNF produced at 800°C using Michmetal-Nickel catalyst. 88
Figure 5: Very long CNTs produced at 750°C using Lanthanum-Nickel catalyst. 88
Figure 6: HRTEM image of CNTs produced in Figure 5 above. 89
Figure 7: Long a) CNTs and b) CNF produced at 650°C using Lanthanum-Nickel. 90
Figure 8: HRTEM image of CNT produced at 850°C using Lanthanum-Nickel alloy. 90
Figure 9: Disordered CNTs at 750°C during reforming with Lanthanum-Nickel. 91
Figure 10: a) Network of CNTs b) a long CNT at 750°C during reforming with Mischmetal-Nickel. 91

LIST OF TABLES

Page
Table 2. 1: Potential parameters for carbon-carbon and carbon-metal interactions (Shibuta and Elliot, 2006).....11
Table 2. 2: Potential parameters for metal-metal interactions (Shibuta and Elliot, 2006).....11
Table 2. 3: The number of moles in the system.....39
Table 2. 4: Number of moles in the system for the gaseous species. 40

Table 3. 1: Conditions at which the experiments are carried out.....44
Table 3. 2: Data for the column used in the GC 46
Table 3. 3: Retention time of gasses 46

Table 4. 1: Gas chromatography results 58

Table A. 1: Conditions at which the samples for the Raman spectrometer are produced. 96
Table A. 2: Data for Figure 4.23(a) 98
Table A. 3: Data for Figure 4.23(b) 98
Table A. 4: Data for Figure 4.23(c) 99
Table A. 5: Data for Figure 4.22.....99

CHAPTER ONE

1.0 Introduction

1.1. Background and motivation

Global warming has become a huge topic in the past few years and means have to be found to dispose of or to reuse greenhouse gasses (Zwaan and Gerlagh, 2005). The most common of these gasses is CO_2 which is a very stable gas and has thus posed a problem to industry in how to dispose or decompose this gas. Some ways of getting rid of this gas are thermal decomposition (Kedr et al., 2007), which requires high temperatures, to capture it, which is very expensive at an industrial scale (Alie et al., 2004), or to convert it to something else that would be less harmful and even economically viable, such as methanol (Chiavassa et al., 2008). One such product is carbon nanotubes (CNTs) which can be synthesized by using CO_2 as a carbon source (Xu and Huang, 2007). Carbon nanotubes have become of great interest to many researchers because of their mechanical properties such as exhibiting up to 5 times the elastic modulus (~ 1 TPa) and almost 100 times the tensile strength (~ 150 GPa) of high strength steels (Zhao et al., 2007), tunable electronic behaviour (they can be conducting or semi-conducting) and their unique dimensions (nanometer diameters and a few centimeters long). Because of these properties CNTs have potential applications in many fields, including superconductors, single molecular transistors and magnetic recording devices (Lou et al., 2003).

CO_2 is not the only greenhouse gas that exists. Another gas is methane, which is also possible to use for the production of CNTs by decomposing it (Chai et al., 2007).

What remains is how to use the greenhouse gasses to produce CNTs and it has been found that the most economically viable process to use to produce CNTs at a large scale is by chemical vapour deposition (CVD). An important by-product of using both gasses in the production of CNTs is syngas (H_2 and CO). Syngas is required in the Fischer-Tropsch process used in the production of petro-chemicals. But, this process produces high emissions of CO_2. By capturing the CO_2 and running it together with a methane feed, the amount of CO_2 emissions will be decreased and the efficiency of the process increased.

1.2. Aim and Objectives

The aim of this project is the production of carbon nanotubes from carbon dioxide and methane and the development of the thermodynamics for the process. This aim will be reached via these objectives:

1. Production of CNTs from CO_2 and CH_4 (together and separately).
2. Analysis of product to determine best catalyst for the process.
3. Development of thermodynamic model.

1.3. Research Questions

Some questions will be answered while achieving the final goal of this project and these questions are:

1. What are suitable catalysts for the production of carbon nanotubes from greenhouse gasses?
2. Are carbon dioxide and methane really viable feeds for the production of carbon nanotubes in effort to save the environment?
3. Is there a possibility for this process to be used at an industrial scale?

1.4. Hypothesis

It is thermodynamically possible to produce CNTs (and syngas) from greenhouse gasses (methane and CO_2).

1.5 Dissertation outline

Chapter One

This chapter discusses the background and motivation, the aims, research problems and the hypothesis of the study.

Chapter Two

This chapter looks at the literature that is relevant to this study. The first part discusses the carbon nanotechnology while the second part focuses on the thermodynamics.

Chapter Three

This chapter explains the experimental procedure undertaken to produce the carbon nanotubes and the syngas.

Chapter Four

This chapter discusses all experimental results.

Chapter Five

This chapter includes the conclusion and recommendations of the study.

CHAPTER TWO

2.0 Literature Review

2.1. Carbon Nanotechnology and Theory

Carbon nanotechnology in this context presents the general overview of carbon nanotubes in terms of structure, production, properties, characterization and growth mechanism of carbon nanotubes.

2.1.1. Structure of Carbon nanotubes

Carbon is one of the most important elements in our lives. This is because it can occur in many different forms and thus gives rise to a number of applications. Some of the current uses of carbon are: aircraft brakes, electrodes, high temperature moulds, rocket nozzles and exit cones, tires, ink, nuclear reactors and fuel particles, filters, prosthetics, batteries and fuel cells, airplanes, and sporting equipment. The different forms of carbon occur because carbon has different crystalline forms (called allotropes) which are: diamond, graphite, fullerenes and carbon nanotubes (CNTs), and because these forms come in different crystalline sizes, degrees of purity and density and crystalline perfection. The reason why carbon has the ability to form these allotropes is because of its four valence electrons which enable it to form different kinds of bonds with other carbon atoms.

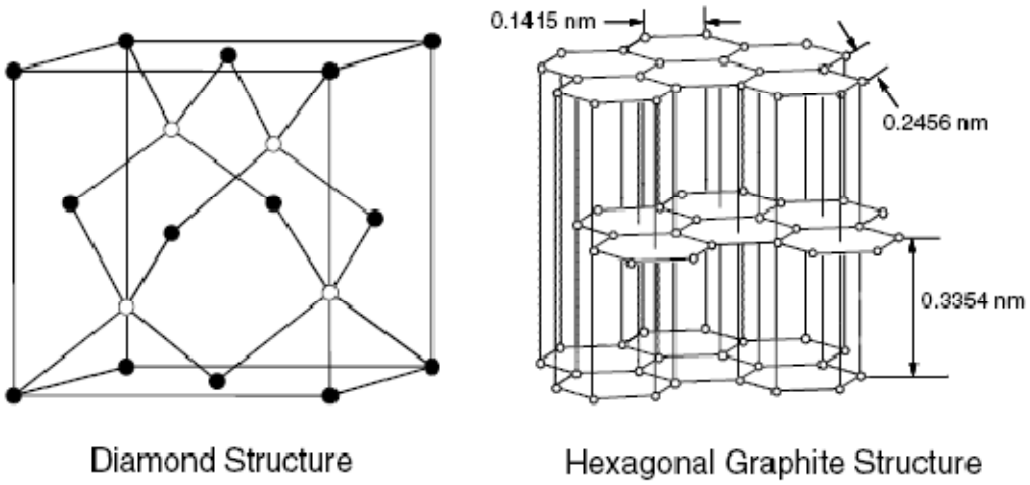

Figure 2. 1: The different structures of carbon. (Hoffman, W. P., 2005)

Figure 2.1 displays the structures of diamond and hexagonal graphite, which are the most abundant allotropes of carbon on the planet. The layered hexagonal structure of the graphite gives it its mechanical, thermal and electrical properties. Figure 2.2 shows the other carbon allotropes, the bucky ball (which is a C_{60} fullerene) and the nanotube.

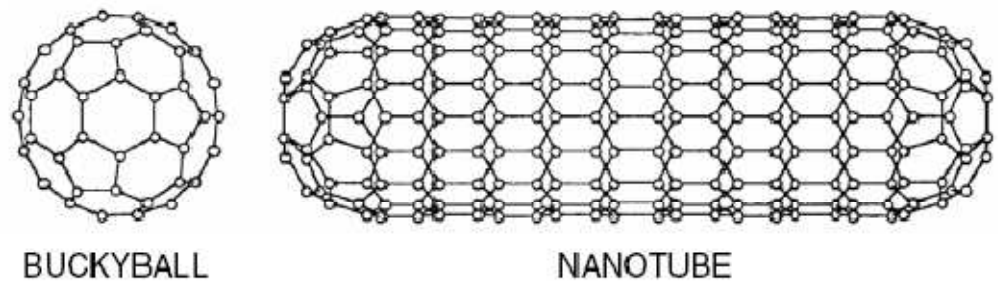

Figure 2. 2: The C_{60} fullerene and carbon nanotube. (Hoffman, W. P., 2005)

Carbon nanotubes were first discovered by Iijima, 1991 although he called them “helical microtubules.” They are considered to be a one dimensional form of fullerenes because their length to diameter ratio is very high. The carbon nanotube can be considered to have two separate regions with differing chemical and physical properties (Figure 2.3).

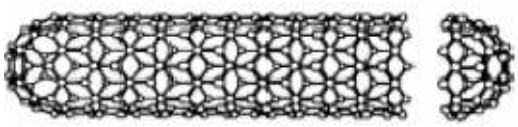

Figure 2. 3: The different regions of a nanotube. (Daenen et. al., 2003)

The “cap” region is the same structure as the C_{60} fullerene but cut into half. The other region is the single wall carbon nanotubes (SWCNTs). It can be considered to be a single, one atom thick, sheet of graphite that has been rolled into a tube (Figure 2.4). A multiwall carbon nanotube (MWCNT) can be likened to a number of SWCNTs of different diameters together.

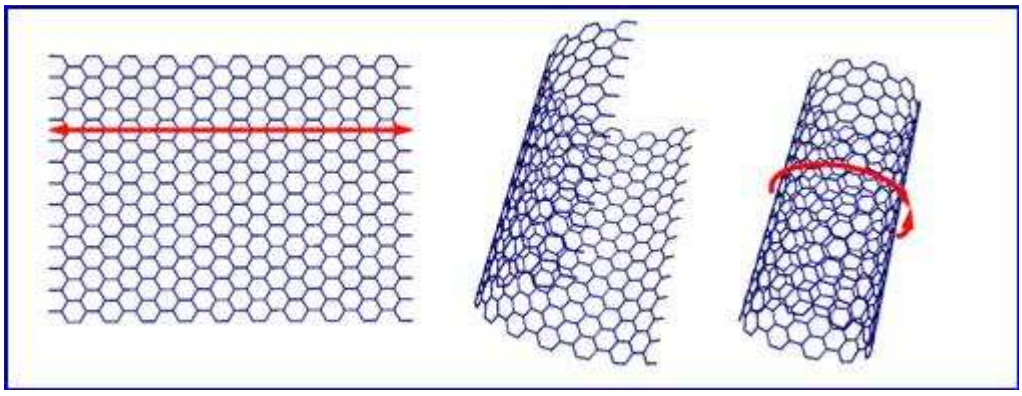

Figure 2. 4: Graphene sheet being rolled into a nanotube.

A single wall nanotube can be completely described, excepting the length, by a chiral vector, $\vec{C}$. If two atoms on the graphene sheet are chosen and one is taken to be the origin, then $\vec{C}$ is the vector pointing from the first atom to the second (Figure 2.5). The equation describing $\vec{C}$ is,

$$\vec{C} = n\vec{a}_1 + m\vec{a}_2 \tag{2.1}$$

where *n* and *m* are integers and $\vec{a}_1$ and $\vec{a}_2$ the unit cell vectors of the two-dimensional lattice formed by the graphene sheets.

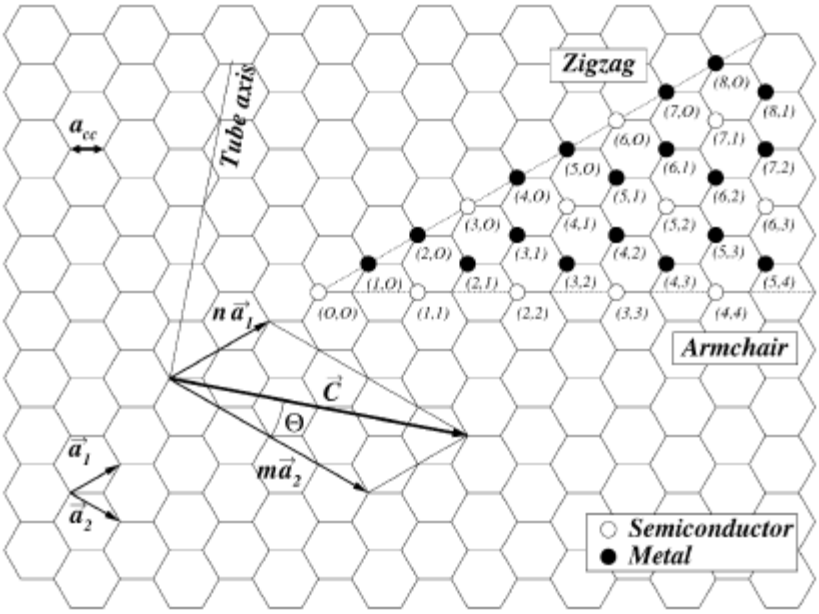

Figure 2. 5: Chiral vector for a (2, 4) nanotube. (Belin and Epron, 2005)

The direction of the nanotube axis is perpendicular to the chiral vector. There are three models that describe the formation of CNTs namely, coaxial cylindrically curved, coaxial polygonized and scrolls graphene sheets (Figure 2.6).

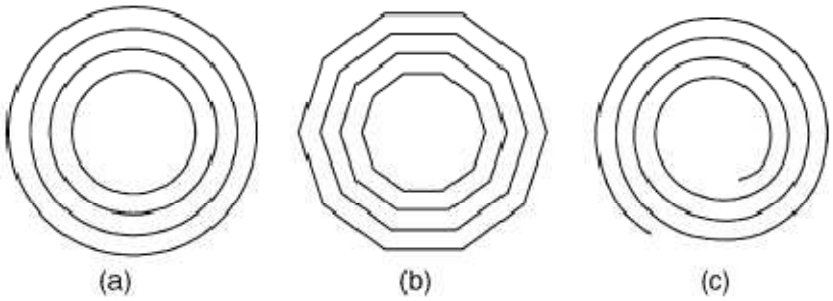

Figure 2. 6: The different models describing nanotubes: a) coaxial cylindrically curved, b) coaxial polygonized and c) scroll. (Belin and Epron, 2005)

The cylindrically curved model is the most widely accepted of the three models. The length of the chiral vector is equal to the circumference of the nanotube and is described by the equation below,

$$c = \left|\vec{C}\right| = a\sqrt{n^2 + nm + m^2} \quad (2.2)$$

where a is the length of the unit cell vector. This a is related to the carbon-carbon bond length by,

$$a = |\overrightarrow{a_1}| = |\overrightarrow{a_2}| = a_{cc}\sqrt{3} \quad (2.3)$$

Where a_{cc} is the carbon-carbon bond length and is equal to 0.1421 nm (Wildoer et. al., 1998). If the curvature of the nanotube is taken into account then a slightly larger value of 0.144 nm should be used (Murakami et. al., 2003, Saito et. al., 2000, Jorio et. al., 2001). The diameter of the nanotube is described by,

$$D = \frac{c}{\pi} \quad (2.4)$$

where c is the circumferential length. The angle between the chiral vector and the "zigzag" nanotube axis is described by

$$\theta = tan^{-1}\left(\frac{m\sqrt{3}}{m+2n}\right). \quad (2.5)$$

Nanotubes are described by the integers (n, m) which are related to the chiral vector. When *n* = *m*, the nanotube is called "armchair" type (θ = 0◦); when *m* = 0, then it is of the "zigzag" type (θ = 30◦). When $n \neq m$, it is a "chiral" tube and θ takes a value between 0◦ and 30◦ (Figure 2.7). The value of (*n*,*m*) determines the chirality of the nanotube and affects the optical, mechanical and electronic properties. Nanotubes with $|n - m| = 3q$ are metallic and those with $|n - m| = 3q \pm 1$ are semiconducting (q is an interger).

a) 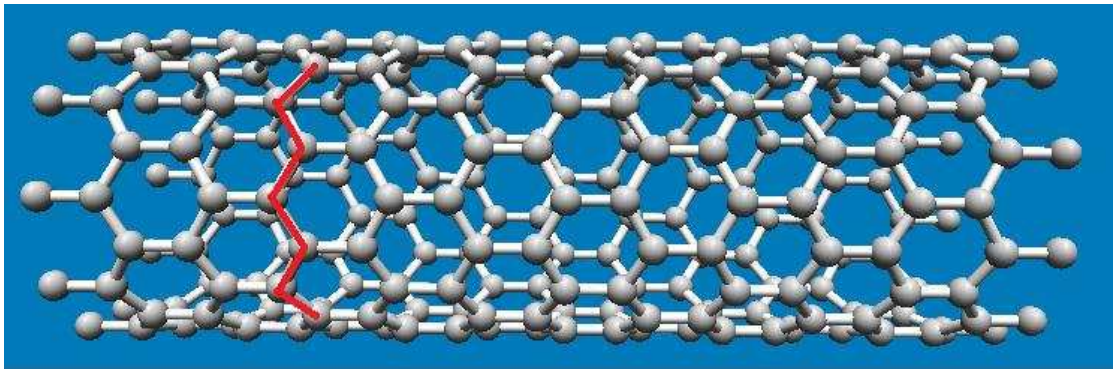

b) 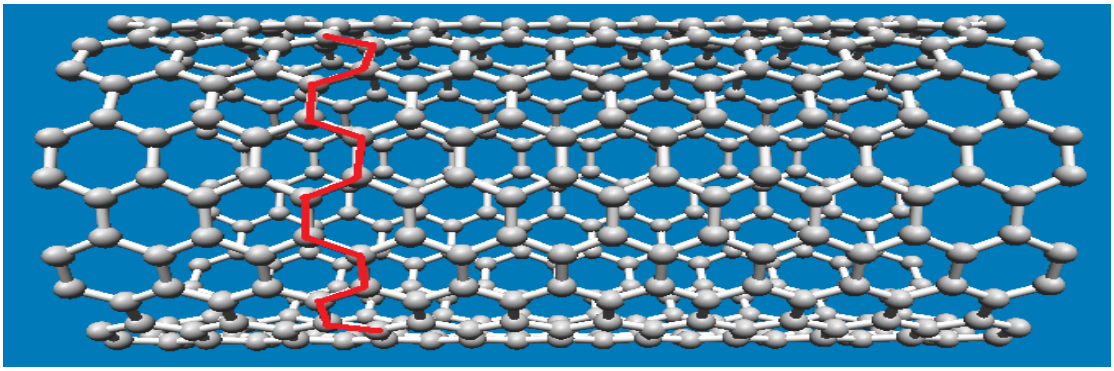

c) 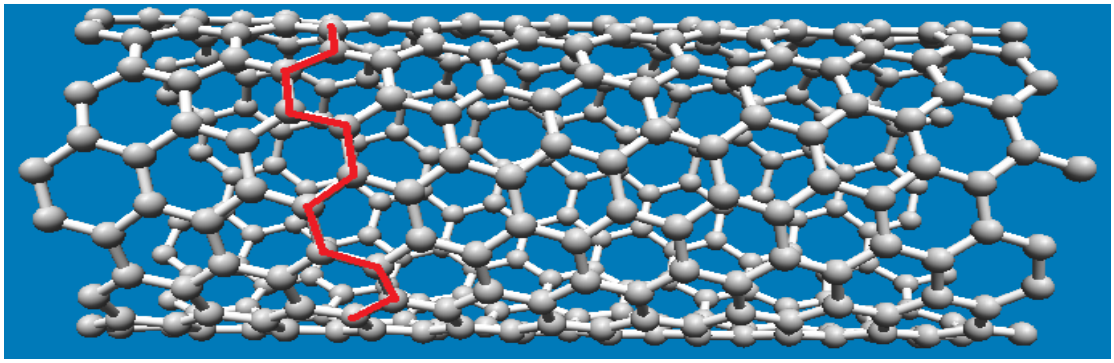

Figure 2. 7: The different types of CNTs a) zigzag, b) armchair and c) chiral.

2.1.2. Properties

Carbon nanotubes are the stiffest and strongest fibre known with a Youngs modulus of approximately 1.4 TPa and a tensile strength of approximately 60 GPa (this is equivalent to a 1mm^2 cable withstanding a 6300 kg mass). This strength occurs because of the sp^2 bonds

between the carbon atoms. The conductivity of a CNT along the tube is very good and the insulating capabilities of the tube axially are also high. The thermal conductivity along the tube is between 1750 and 5800 W/mK (Hone et. al., 1999). As mentioned before the CNTs can be either conducting or semi-conducting depending on the chirality of the carbon nanotube. The conductance of a CNT is predicted to be $2G_0$ independent of the diameter and length, where $G_0 = \frac{2e^2}{h} = \frac{1}{12.9} K\Omega$, which is one unit of the conductance quantum, e is the charge on one electron and h Plank's constant (Frank et. al., 1998). CNTs have been found to conduct current ballistically without dissipating heat. They can also carry the highest current density known of any material, which has been measured as high as 109 A/cm^2.

2.1.3. Growth models

There are many models that exist which describe the growth of CNTs. Some of these models are presented below.

Model 1: Molecular dynamics

A molecular dynamics (MD) method is used by Shibuta and Elliot, 2006 to study the interactions between a metal cluster and a grapheme sheet. A Brenner potential is used to describe the covalent bonds between carbon atoms in the grapheme. A many-body potential function is also used to describe metal-metal and metal-carbon bonding. The parameters that Shibuta and Elliot, 2006 used for the simulation are in the tables below.

Table 2. 1: Potential parameters for carbon-carbon and carbon-metal interactions (Shibuta and Elliot, 2006).

	D_e(eV)	S	β(1/Å)	R_e(Å)	R_1(Å)	R_2(Å)	*b*	δ	a_o	c_o	d_o
C-C	6.325	1.29	1.5	1.315	1.7	2.0	-	0.80469	0.011304	19	2.5
Ni-C	2.4673	1.3	1.8706	1.7628	2.7	3.0	0.0688	0.5351	-	-	-

Table 2. 2: Potential parameters for metal-metal interactions (Shibuta and Elliot, 2006).

	S	β(1/Å)	D_{e1}(eV)	D_{e2}(eV)	C_D	R_{e1}(Å)	R_{e2}(Å)	C_R	R_1(Å)	R_2(Å)
Ni-Ni	1.3	1.57	0.4217	1.0144	0.8268	2.4934	0.1096	0.3734	2.7	3.2

The interactions between metal atoms can be expressed by a one-dimensional average Lennard-Jones potential function as shown below:

$$F(z) = D_e \left\{ \frac{1}{5} \left(\frac{z}{\sigma} \right)^{-10} - \left(\frac{z}{\sigma} \right)^{-4} \right\} \tag{2.6}$$

where:

z – Coordinate normal to the substrate plane

σ - Van der Waals radius of metal atom

D_e – This parameter is varied from 0.5 to 1.5 eV at 0.05 intervals to describe the affinity of the metal cluster for the substrate.

This model states that a metal cluster forms on a substrate and this metal cluster becomes the basis for the formation of the fullerene cap which approximately takes the form of the metal cluster. The entire process is better described below.

The metal cluster binds to the substrate in a certain way and there is a contact angle formed. This contact angle, θ(shown in the Figure 2.8), is estimated by Shibuta and Elliot, 2006 by assuming that the metal cluster that forms on the substrate is spherical.

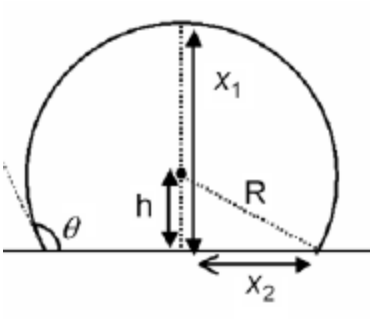

Figure 2. 8: Spherical metal cluster on substrate (Shibuta and Elliot, 2006)

$$\cos\theta = -\frac{h}{R} \tag{2.7}$$

where R is the radius of the metal cluster and h can be seen from Figure 2.3.1 above. The R and the h can be described by the parameters x_1 and x_2 (from Figure 2.8.)

$$\therefore R = \frac{x_1^2 + x_2^2}{2x_1}$$

$$h = \frac{x_1^2 - x_2^2}{2x_1}$$

$$\therefore \theta = \cos^{-1}\left(\frac{x_2^2 - x_1^2}{x_2^2 + x_1^2}\right)$$

The surface area, A, of the metal cluster can be described by,

$$A = 2\pi R^2(1-\cos\theta)$$
$$A = 2\pi\left(x_1^2 + x_2^2\right) \tag{2.8}$$

Model 2: Carbon atom transport

This model considers the catalyzed growth of a SWCNT by the diffusion of carbon atoms on the outer wall of the nanotube. This is depicted in the Figure 2.3.2 below where the dark particle is the catalytic metal particle.

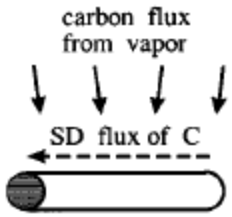

Figure 2. 9: Deposition of carbon atoms on surface of SWCNT (Louchev et al., 2004)

The model assumes that the main role of the catalyst particle is to keep the nanotube open and also that the nucleation of the SWCNT doesn't affect the model in any way as the model considers the post nucleation of the SWCNT. It is assumed that the growth of the SWCNTs is fed by carbon atoms that initially adsorb onto the SWCNT surface then diffuse to the metal particle end. Other assumptions that are made are that carbon atoms dominate in the formation of the SWCNT and that other carbon species impinging on the SWCNT surface also have high surface mobility. If this assumption were not made then the carbon species would restrict movement on the surface of the SWCNT and this would lead to the formation of other layers, meaning that a MWCNT would be formed. It is also assumed that SD flux over the lateral surface dominates over the diffusion through the surface of metal particle and that the growth rate is controlled by SD over the SWCNT surface (Figure 2.10.)

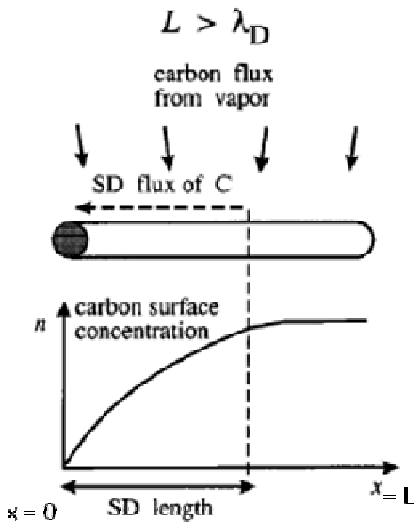

Figure 2. 10: Long SWCNT where length, L, is higher than the characteristic surface diffusion length, λ_D.

The distribution of carbon atom concentration over the SWCNT surface is:

$$\frac{\partial n}{\partial t} + \nabla J_s = Q_c - \frac{n}{\tau_a} \tag{2.9}$$

Q_c – the impinging carbon flux onto SWCNT surface from the vapour

$\tau_a \approx v^{-1} \exp\left(\frac{E_a}{k_b T}\right)$ - adsorbtion time

$v \approx 10^{13} Hz$ - thermal vibration frequency

$E_a \approx 1.8 - 3.6eV$ - adsorbtion energy

J_s – is SD flux of carbon expressed as:

$$J_s = -\frac{nD_s}{k_B T} grad\mu = -D_s gradn + nD_s \ln\left(\frac{n}{n_o}\right) T^{-1} gradT \tag{2.10}$$

where:

$D_s = a_0^2 v \exp\left(\frac{-\partial E_d}{k_B T}\right)$ - SD coefficient including activation energy of surface diffusion

$\partial E_d \approx 0.2 - 1.5eV$

n_o – surface density of adsorbtion sites

n/n_o must be much smaller than 1 for the expression to be true.

At the growth edge (metal catalyst side) of the SWCNT (where x = 0):

$$kn = -J_s$$

$k = k_0 \exp\left(\frac{-\Delta E}{k_b T}\right)$ - Arrhenius-type kinetic constant for incorporation of carbon atoms into SWCNT

ΔE - Activation energy barrier

SWCNT growth rate:

$$V = \frac{dL}{dt} = \Omega J_s \mid_{x=0} \tag{2.11}$$

where:

Ω - specific area per carbon atom

Experiments have shown that the growth of SWCNT by arc discharge and laser ablation only happens in the presence of inert gas (at pressures higher than 10^4 Pa.) Hester and Louchev, 2003 and Louchev et al., 2002 have suggested that the inert gas facilitates effective dissipation of heat released during SWCNT growth. Proper heat dissipation is important as the increase in the SWCNT temperature would lead to it disintegrating. The heat released by the carbon condensation into the SWCNT, E_b, is approximately 7.3eV. The heat released can be divided into two parts. The first is heat released when the carbon chemisorbs onto the SWCNT surface, E_a, and the second is at the metal particle end where the carbon is added to the SWCNT structure $E_{add} = E_b - E_a$.

By using the continuum differential equation for thermally thin shells, the temperature regimes for a growing nanotube can be evaluated by this equation,

$$\rho c \frac{\partial T}{\partial t} + \nabla J_T = \frac{1}{\delta}\left\{ E_a \left(Q_c - \frac{n}{\tau_a} \right) - q_d \right\} \tag{2.12}$$

where:

$\delta \cong 0.2nm$ - wall thickness

q_d – heat dissipation function described below

$J_T = -k_s(T) gradT$ - conduction heat flux along SWCNT wall

$k_s(T) \approx 118 \exp\left(\frac{1500}{T}\right) \frac{W}{m.K}$, for T between 1000K and 2000K

The heat release that occurs at the growth edge (x = 0) can be included by,

$$k_s gradT = (E_b - E_a) \frac{J_s}{\delta} \tag{2.13}$$

At the opposite end of the SWCNT (x = L, Figure 2.10) it is assumed that gradT = 0.

Heat dissipation from the SWCNT by collisions with the inert gas atoms can be described by,

$$q_d = \Delta E_k Q_g \tag{2.14}$$

where:

ΔE_k - energy transferred from the SWCNT per collision

$Q_g = \frac{P_g}{(2\pi m_g k_B T_g)^{1/2}}$ - flux of colliding atoms per surface area unit

P_g - gas pressure

m_g - mass of gas atom

T_g - temperature of gas

Using the strong collision assumption (SCA) by Hinshelwood, 1927, the temperature of the gas atom is the same as the temperature of the SWCNT. Therefore the energy transferred by the collision is expressed by,

$$\Delta E_k = \frac{3}{2} k_B \left(T - T_g\right) \tag{2.15}$$

The SCA overestimates the collision energy transfer, thus a correction factor, α, has to be introduced. The energy transfer then becomes,

$$\Delta E_k = \frac{3}{2} \alpha k_B \left(T - T_g\right) \tag{2.16}$$

where, $0 < \alpha < 1$

Then, $q_d = \frac{3}{2} \alpha Q_g k_B \left(T - T_g\right) = h_g \left(T - T_g\right)$ (2.17)

where, $h_g = \frac{3 \alpha Q_g k_B}{2}$ - heat exchange coefficient.

$$\alpha = \frac{1}{3} \beta \left(\frac{m_g}{m_{ref}} \right)^n \tag{2.18}$$

where, n = 1/3 or n = 1; m_{ref} = mass of xenon; $\beta = 1$ for SWCNTs.

Temperature Variations in SWCNT growth

The temperature of the SWCNT changes its behavior over time. There are four stages that the temperature goes through. The first is that the SWCNT temperature remains constant and uniform over the length of the SWCNT. Secondly, the SWCNT temperature decreases but it remains uniform along the SWCNT. Thirdly, non-uniformity of temperature distribution appears. In the final stage the growth rate and the temperature gradient stabilizes. These stages are caused by the two characteristic length scales of the SWCNT growth. The first one is surface diffusion described by,

$$\lambda_D \approx \sqrt{D_s \tau_a}\,, \tag{2.19}$$

Which describes the length that the carbon atom can travel before desorption. The second is the heat conductance length,

$$\lambda_c \approx \sqrt{\frac{k_s \delta}{h_g}}, \tag{2.20}$$

which is the length that heat can effectively travel along the shell of the SWCNT by conductance k_s when there is heat exchange with the ambient gas (h_g). For the first stage of the SWCNT growth (according to the temperature changes) the SWCNT temperature can be estimated by,

$$T - T_g \approx \frac{Q_c E_b}{h_g} \approx \frac{2}{3} \frac{E_b P_c}{\alpha k_B P_g} \frac{m_g^{1/2}}{m_c^{1/2}} \tag{2.21}$$

P_c - carbon vapour pressure

P_g - vapour pressure of inert gas

m_c - atomic mass of carbon

m_g - atomic mass of inert gas.

The first stage ends when, $L \approx \lambda_D$.

The second stage occurs when the SWCNT length becomes longer than the SD length (Figure 2.10), only the carbon atoms that impinge on the surface, within the SD length from the metallic particle, will contribute to the heat release. For this stage the temperature can be estimated by,

$$T - T_g \approx \frac{Q_c E_b}{h_g} \frac{\lambda_D}{L} \approx \frac{2}{3} \frac{E_b P_c}{\alpha k_B P_g} \frac{m_g^{1/2}}{m_c^{1/2}} \frac{\lambda_D}{L} \tag{2.22}$$

L – SWCNT length.

The SWCNT growth for uniform temperature distribution is given by,

$$\frac{dL}{dt} = -\Omega D_s \frac{dn}{dt} = \frac{\Omega k Q_c \tau_a \sinh\left(L/\lambda_D\right)}{\sinh\left(L/\lambda_D\right) + \left(k\lambda_D/D_s\right)\cosh\left(L/\lambda_D\right)}. \tag{2.23}$$

The temperature of the SWCNT is then described by,

$$Mc\frac{dT}{dt} = 2\pi R\int_0^L E_b[Q_c - n(x)/\tau_a]dx - 2\pi RLh_g(T - T_g), \quad (2.24)$$

where:

M = mass of SWCNT

$n(x) = Q_c\tau_a + C_1 \times \exp(-x/\lambda_D) + C_2\exp(x/\lambda_D)$ - surface concentration distribution of adsorbed carbon.

If $M \approx m_c N$ & $2\pi RL \approx S_a N$, where S_a is the specific surface per atom and N is the number of atoms in the wall, then the approximation for SWCNT temperature then becomes,

$$\frac{dT}{dt} = \frac{S_a}{m_c C}\{E_b Q_c k\tau_a U^* L^{-1} - h_g(T - T_g)\} \quad (2.25)$$

where:

$$U^* = \frac{\exp(L/\lambda_D) - 1 + \exp(2L/\lambda_D)[1 - \exp(-L/\lambda_D)]}{[1 + \exp(2L/\lambda_D)]k\lambda_D/D_s - [1 - \exp(2L/\lambda_D)]}.$$

Model 3: Intermolecular interaction

The interaction between a carbon nanotube (CNT) and the catalyst can be described by van der Waals forces. When the van der Waals force minimizes a carbon atom may deposit between the catalyst and the CNT. For an optimized growth model of a CNT, the phonon vibration amplitude (the catalyst-tube distance) must be equal to the diameter of a carbon atom. Since the phonon vibration is dependent on temperature, the optimum growth mechanism will also only occur at the corresponding optimum temperature (Vaezzadeh et al., 2005). It is common practice to simulate phonon vibration by a spring. For this model Vaezzadeh et al., 2005 assumed that the longitudinal vibrations play a major role in the growth of the CNT but the transversal vibrations do not contribute to the growth. Figure 2.11 below illustrates the spring model.

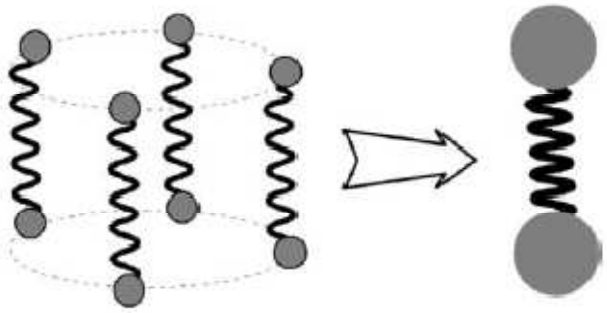

Figure 2. 11: Illustration of carbon loops and their equivalent form. (Vaezzadeh et al., 2005)

Since all forces between the loops are acting in the same direction, the net force between the loops is $-nk$, where the n is the number of carbon atoms in one loop and k is the force between two carbon atoms. Therefore,

$$K = nk \tag{2.26}$$

K – equivalent spring coefficient.

The equivalent form for N(t) loops of the CNT is given in Figure 2.12 below. The M in the diagram is the mass of one loop and M = nm_c where m_c is the mass of a single carbon atom. The equivalent form can be further simplified to the second diagram in Figure 2.12 where the M_T is the total mass of the CNT, K_T is the total spring coefficient and l(t) is the length of the growing nanotube. Thus,

$$M_T = N(t)M\ ,\ K_T = N(t)K \text{ and } l(t) = N(t)\bar{l} = N(t)l_c\,. \tag{2.27}$$

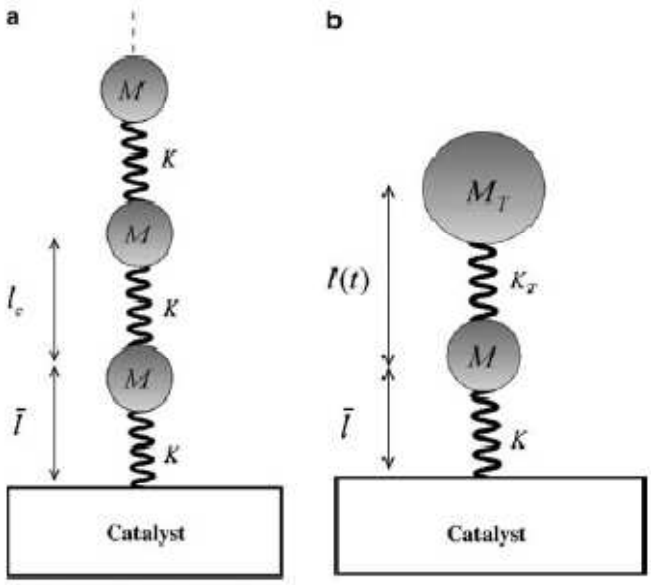

Figure 2. 12: Illustration of CNT growth system: a) loop equivalent form; b) growth equivalent form. (Vaezzadeh et al., 2005)

$$H = \frac{P^2}{2M} + \frac{P_T^2}{2M_T} + V(z) \approx \frac{P^2}{2M} + V(z) \tag{2.28}$$

H = Hamiltonian of the system

If the potential energy of the Hamiltonian maximizes this expression is obtained as:

$$\frac{1}{2}k_B T = \frac{1}{2}K\left(l - \bar{l}\right)^2 + \frac{1}{2}K_T\left(l' - l(t)\right)^2 \tag{2.29}$$

l = unequilibrium length of spring between carbon and catalyst

l' = unequilibrium length of the equivalent spring.

Due to the similarities of phonon vibrations:

$$l - \bar{l} \approx l' - l(t) \equiv z(t)\,. \tag{2.30}$$

Using equations 2.29 and 2.30:

$$k_B T = \left(K + K_T\right)z(t)^2\,, \tag{2.31}$$

And,

$$K = M\varpi^2 \;\&\; K_T = nN(t)K \tag{2.32}$$

ϖ = frequency of CNT vibrations.

For motion in the longitudinal direction (z):

$$z(t) = nN(t)z_{\max}\sin(\varpi t)\,. \tag{2.33}$$

The number of loops can be described by:

$$N(t) = \frac{\varpi}{2\pi}t\,. \tag{2.34}$$

Now the CNT growth in a vacuum is given by:

$$l(t)^5 + \frac{l_c}{n}l(t)^4 - \frac{k_B T l_c^5}{4\pi^2 n^4 m_c z_{\max}^2}t^2 = 0\,.$$

CNT growth while taking into account the effect of the atmosphere and other losses that may affect the system:

$$l(t)^5 + \frac{l_c}{n}\left[l(t)e^{\gamma t}\right]^4 - \frac{k_B T l_c^5}{4\pi^2 n^4 m_c z_{\max}^2}t^2 = 0\,.$$

$z_{\max}$ (vibration amplitude) is not easily obtainable by experiments, but it must be much smaller than l_c (bonding length which is approximately 1.5 $\overset{o}{\text{A}}$.)

Therefore $z_{\max} \approx 0.01 l_c$, can be used.

2.1.4. Production

There are different methods to producing CNTs which include arc discharge, laser ablation and chemical vapour deposition (CVD).

Arc Discharge

It is found, according to Keidar, 2007, that arc discharge is the most practical method for synthesizing single wall nanotubes (SWCNTs). It produces SWCNTs with fewer defects than those methods which operate at low temperature such as CVD. This is believed to be

true due to the fast growth rate of the SWCNTs. In fact compared to the CVD method, which has a slower rate of formation, the CNTs produced are kinked or curved. It is believed to be of a general consensus that the key parameter of nanotube growth in arc discharge is the anode erosion rate. Another factor is the current conductivity across the composite. The diameter and hence the growth rate is determined by the pressure of the atmosphere (composing of helium and argon) around the arc. It is found that the diameter of the SWCNT is dependent on the mole fraction of argon in the helium-argon gas mixture. Figure 2.13 below shows a simplified schematic drawing of arc discharge apparatus.

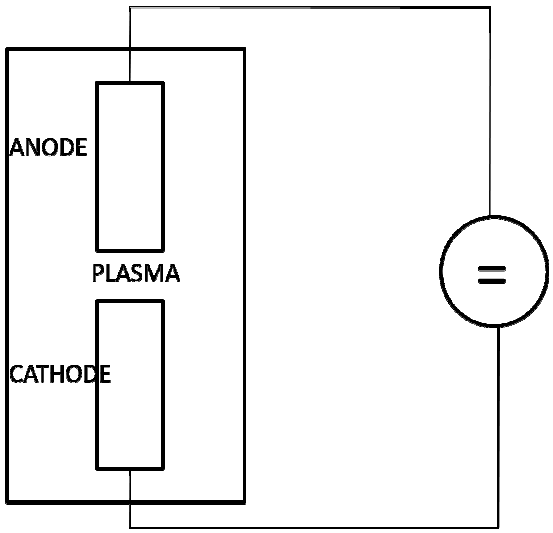

Figure 2. 13: Arc discharge setup showing 2 graphite electrodes which are used to produce an electric arc discharge in an inert gas atmosphere. (Popov, 2004)

Laser Ablation

Laser ablation is a process in which laser pulses heat a carbon target, for example graphite with cobalt and nickel catalyst present, and vapourises them. This high energy vapour expands rapidly and then condenses to form clusters of carbon molecules which can include fullerenes. The catalyst cools at a lower rate and is believed to prevent the caging of the carbon structures and thus forming bulky balls. The SWCNTs then grow off the catalyst until

the catalyst particles become too large or until the rate of diffusion of the carbon molecules sufficiently decrease due to the cooling of the apparatus. The catalyst particle may also become saturated with the carbon molecules and the growth ceases. The diameter of the inner tube is believed to be a very important parameter in SWCNT growth. If the diameter is too large then the carbon molecules which are initially vapourized from the laser can escape the heating effect of the latter laser pulses. Figure 2.14 shows the apparatus used for laser ablation.

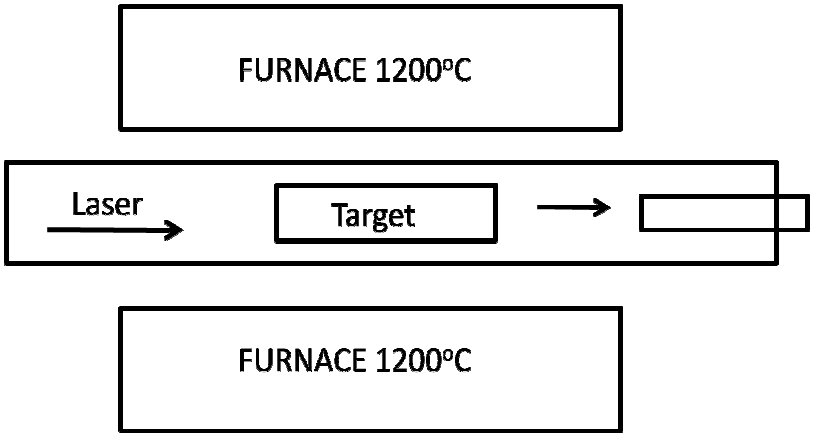

Figure 2. 14: Laser ablation schematic depicting a laser beam which vapourises a target consisting of a mixture of graphite and a metal catalyst. (Popov, 2004)

Chemical vapour deposition

The synthesis of carbon nanotubes by CVD is achieved by essentially cracking a carbon species in the gaseous phase using a heating coil to impart energy to gaseous carbon molecules. Some of the substances used are acetylene, methane, carbon monoxide, pentane, octane, propylene LPGs and ethanol. These reactive radical carbon molecules, produced due to cracking, then react and bond on a catalyst that is generally heated. This catalyst can either be a substrate or can be a floating catalyst. A list of some of the catalysts that are used for the production of nanotubes is given:

Fe/SiO_2, Co/La_2O_3, Ni/Al_2O_3, $Co\text{-}Mo/SiO_2$, Ni/SiO_2, $LaCoO_3$, $LaFeO_3$, $Ni\text{-}Cu/Al_2O_3$ and Fe/Al_2O_3. The selection of the catalyst can also determine the formation of CNTs. The advantage of CVD is that it allows the manufacturer to avoid the process of separating nanotubes from the carbonaceous particulate that often accompanies the other two methods of synthesis (McBride, 2001). The CVD synthesis process consists of essentially two steps: A catalyst preparation step followed by actual synthesis of the nanotubes. The catalyst is generally prepared by sputtering a transition metal onto a substrate and then using either a chemical etch or thermal annealing to induce catalyst particle nucleation. It has been shown that the size and material of the catalyst particles play a vital role during synthesis. There are horizontal CVDs and vertical CVDs. The horizontal CVDs are either homogenous or heterogeneous. The homogeneous CVD processes are based on a homogeneous phase decomposition of two precursors, one for the metal and the other one for the carbon and CNTs can be collected either on a substrate or as a powder in, or at, the exit of the CVD reactor (Figure 2.15a). Heterogeneous processes consist of the decomposition of certain hydrocarbons on small metal particles or thin films deposited on a substrate (Figure 2.15b).

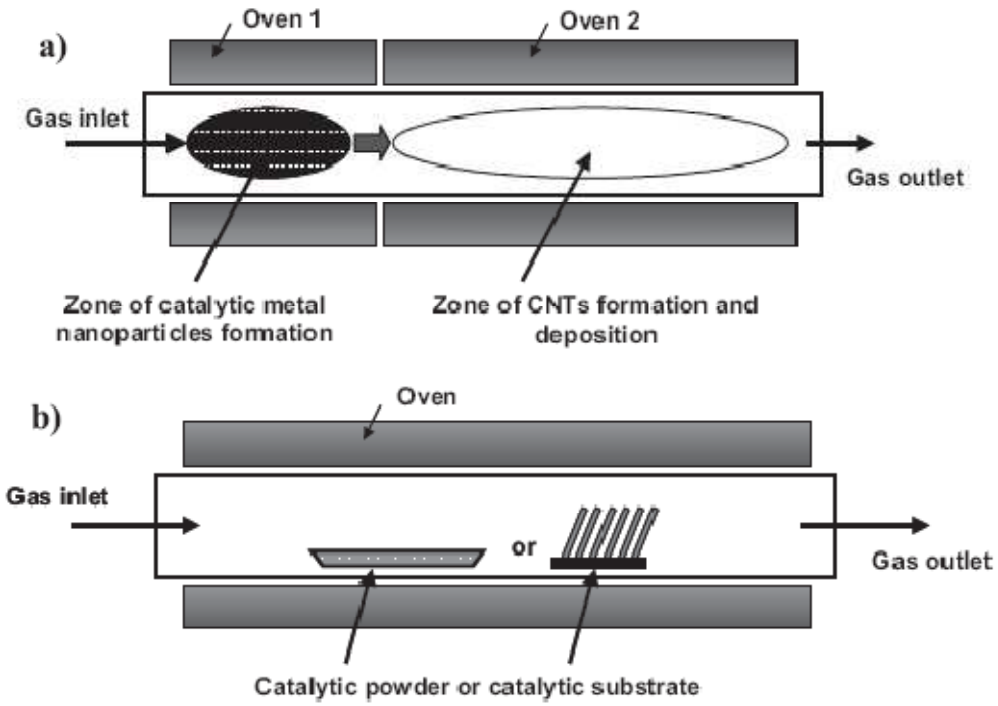

Figure 2. 15: a) Homogenous horizontal CVD b) Heterogeneous horizontal CVD. (Philippe, 2007)

The vertical CVDs are designed to produce CNTs under fluidized bed conditions. Figure 2.16 displays the different types of vertical CVDs.

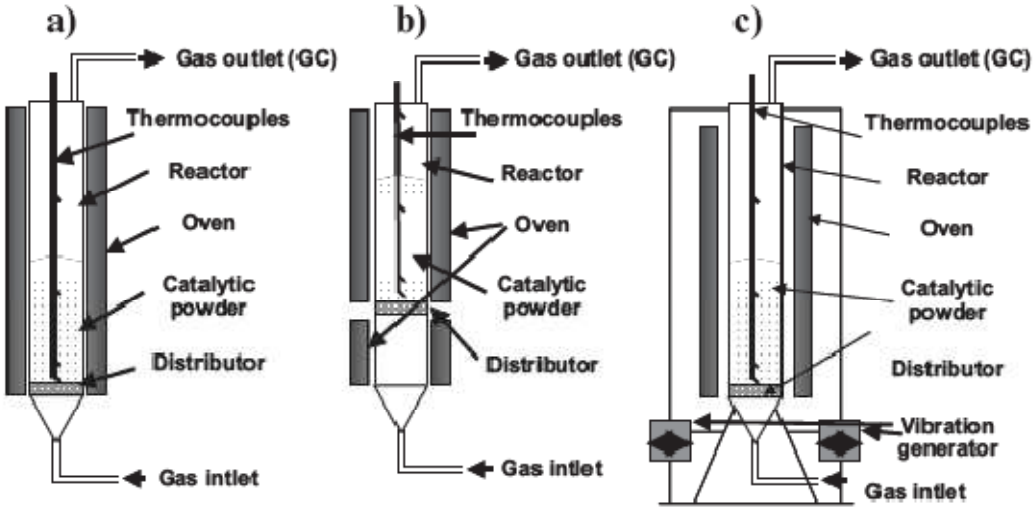

Figure 2. 16: a) Standard fluidised bed CVD reactor, b) fluidised bed CVD reactor with gas pre-heating, c) vibro-fluidised-bed reactor. (Philippe, 2007)

2.1.5. Carbon dioxide decomposition

The decomposition of CO_2 has been found to be very difficult especially if the method used is thermal decomposition. The temperatures necessary for substantial conversion of CO_2 to CO are around the 2500^oC mark which is extremely high. However there are reports of the decomposition and dissociation of CO_2 at lower temperatures using certain catalysts. Lou et. al., 2003 produced CNTs in an autoclave using metallic lithium at 550^oC and 700 atm. Xu and Huang, 2007 were able to produce MWCNTs at 790 and 810^oC using a normal CVD method and a Fe/CaO catalyst. The reaction mechanism followed is that CO_2 reacts to CO and O which is followed by CO disproportionation where 2 CO molecules react with each other to form carbon and CO_2. CO_2 was also found to dissociate on rare earth metals between 823 and 603K at approximately atmospheric pressure (Arakawa et. al., 1988). The dissociation is measured by the increasing resistivity of the various metals. Wustite ($Fe_{0.98}O$) is used to reduce CO_2 at 573K and atmospheric pressure to carbon (Zhang et. al., 1999). The mechanism proposed for the reduction is the conversion of CO_2 to CO and from CO to C. The conversion of CO is faster than the CO_2 conversion and thus the CO is considered to be an intermediate. The thermodynamics of the thermal decomposition of CO_2 have been looked at by Lietzke and Mullins, 1981 and their findings are shown in Figure 2.17.

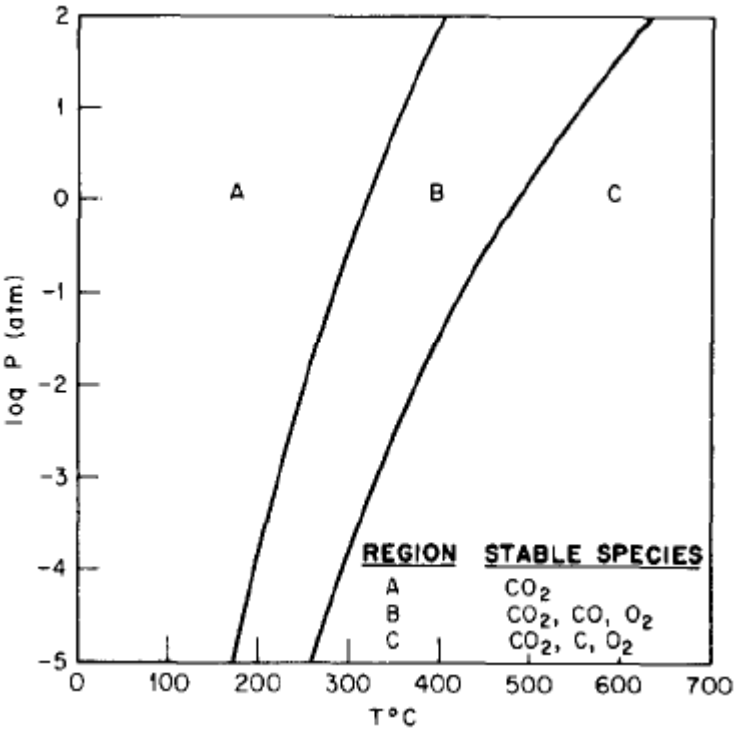

Figure 2. 17: Phase boundary curves for the dissociation of CO_2.

2.1.6. Reforming

The process of carbon dioxide (CO_2) reforming of methane (CH_4) has for the past couple of decades received considerable attention. It utilizes two of the cheapest carbon containing compounds and produces useful chemical products such as syngas (H_2 and CO). Another method for the production of syngas is steam (H_2O) reforming of methane but the use of CO_2 has been found to have a few advantages over this method. Some of these advantages are, the H_2:CO ratio is lower for the CO_2 reforming which is suitable for the Fischer-Tropsch process for the production of higher hydrocarbons, the fact that CO_2, which is considered to be an important greenhouse gas, is used in a more productive manner and it has better use in energy transmission systems (Mc Crary, et. al., 1982, Tokunaga, et. al., 1989). The major problem with using CO_2 is the carbon deposition over the catalyst. Carbon deposition has not only been predicted in thermodynamic studies of the system at industrially desired conditions

(Dibbern et al., 1986, Swaan et. al., 1994) but it has been confirmed to occur on several metal catalysts including nickel (Liu and Au, 2003, Gadalla and Bower, 1988) which is considered to be the best catalyst for this system. Carbon formation on the catalyst does not only cause catalyst deactivation but it can also degrade the catalyst. There can also be a build up of carbon deposits and degraded catalyst which can plug up the reactor and cause a complete process shut down. Noble metal (Ru, Rh, Pt, Pd and Ir) catalysts have been found to coke less than the nickel based catalysts (Gadalla and Bower, 1988, Gadalla and Sommer, 1989, Richardson and Paripatyadar, 1990, Rostrup-Nielsen and Back-Hansen, 1993). The high cost of these noble metals has restricted their use and thus has caused researchers to find nickel based catalysts which resist coking (Fei et. al., 2004, Hou et. al., 2005). A list of the reactions that are expected to take place during CO_2 reforming of methane are:

Carbon dioxide reforming:

$$CH_4 + CO_2 \Leftrightarrow 2CO + 2H_2$$

Reverse water gas shift:

$$H_2 + CO_2 \Leftrightarrow CO + H_2O$$

Steam reforming:

$$CH_4 + H_2O \Leftrightarrow CO + 3H_2$$

Boudouard reaction:

$$2CO \Leftrightarrow C + CO_2$$

Methane decomposition:

$$CH_4 \Leftrightarrow C + 2H_2$$

Coke gasification:

$$C + H_2O \Leftrightarrow CO + H_2$$

2.1.7. Analysis Equipment

Transmission Electron Microscope

The Transmission Electron Microscope (TEM) (Figure 2.17) works on the same basic principal as a light microscope but instead of using light it uses electrons. What can be seen with a light microscope is limited by the wavelength of the light but utilising electrons as the "source of light" and because of their lower wavelength it is possible to get resolutions a thousand times better than a light microscope. TEMs allow for us to see objects to the order of a few angstrom (10^{-10} m) and allow the study of materials done to near atomic levels, which makes it suitable for CNT analysis. A "light source" at the top of the microscope emits electrons that travel in a vacuum through the column of the microscope. Electromagnetic lenses are used to focus the electrons into a very thin beam instead of the glass lenses used in light microscopes. The beam of electrons travels through the specimen to be studied and depending on the density of the specimen some of the electrons will be scattered and lost. The electrons that make it through hit the fluorescent screen and give rise to a shadow image of the specimen and the different parts are displayed in varying darkness according to their density. The image can be studied by an operator or photographed.

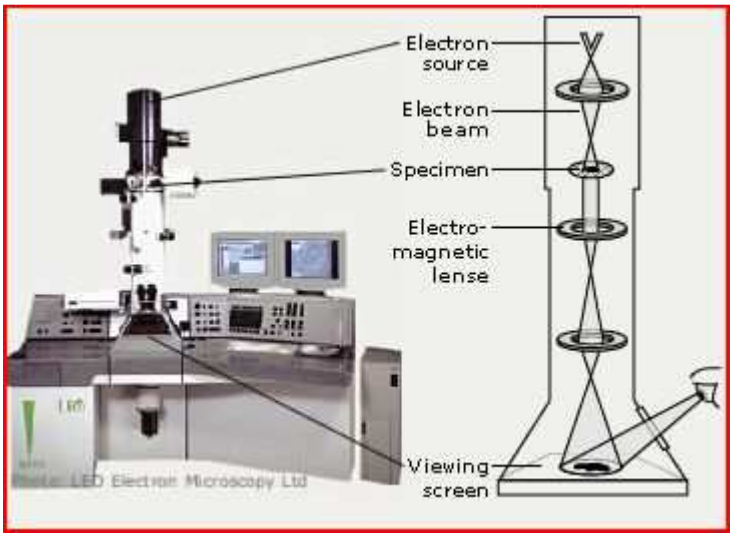

Figure 2. 18: Transmission Electron Microscope with a schematic diagram of the inside.

Raman Scattering

Raman Scattering is a powerful light scattering technique used to characterise the internal structure of molecules and crystals. In a light scattering experiment light of a known frequency and polarisation is scattered from a sample. Raman scattered light is frequency shifted with respect to the excitation frequency but the magnitude of the shift is independent of the excitation frequency. This Raman shift is an intrinsic property of the sample. A definite Raman shift corresponds to the excitation energy of the given sample but only some parts of the sample are "Raman active" which means only some parts take part in the Raman scattering process. Therefore the frequency spectrum of the Raman scattered light maps out only part of the excitation spectrum. There are other techniques available, such as IR absorption that can map the non-Raman active excitations. Additional information can be obtained by the polarisation dependence of the Raman scattered light. The shape of the excitation pattern in the material and polarisation dependence of the scattering is determined by the equilibrium structure of the material due to the rules of group theory. Because of this unambiguous structural information from the Raman polarisation dependence can be obtained. A diagram of the result of Raman testing is shown below.

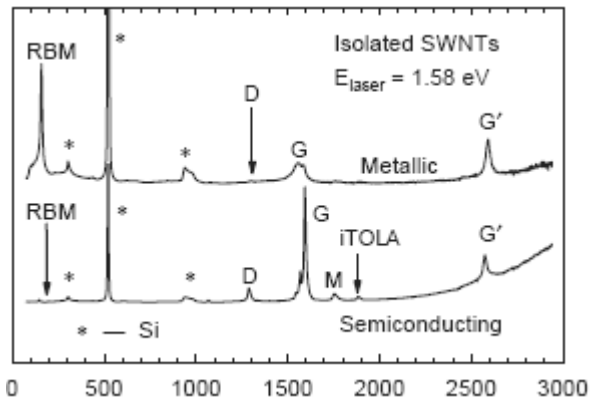

Figure 2. 19: Example of actual Raman data that is characteristic to CNTs. (Dresselhaus et. al., 2004)

All the allotropes of carbon are Raman active and can thus be characterised. The most common features of CNTs on the Raman shift are: (i) low frequency peak < 200 cm^{-1} dependent on the diameter of tube (where RBM is radial breathing mode); (ii) a large structure (1340 cm^{-1}) assigned to residual ill-organized graphite; (iii) a high-frequency bunch (between 1500 and 1600 cm^{-1}) called the G band; (iv) a second order observed mode between 2450 and 2650 cm^{-1} assigned to the first overtone of the D mode and often called G' mode; (v) a combination mode of the D and G modes between 2775 and 2950 cm^{-1} (Belin and Epron, 2005).

Gas Chromatography

Gas chromatography (GC) (Figure 2.19) is equipment which separates a gas mixture into its individual components. It works by a carrier gas transporting the gas mixture into a tube (called a column) which contains a specific column filling (column support). The constituents of the sample gas pass through the column at different rates due to their properties and their interaction with the filling. As the individual constituents exit the column they are detected and identified electronically. The function of the filling is to separate the constituents by differentiating their flow rates and thus the different components exit the column at different times (retention time). The exit gas is collected during the experiments and is injected into the GC. This determines whether or not the input gasses have been broken done and to what extent they are decomposed.

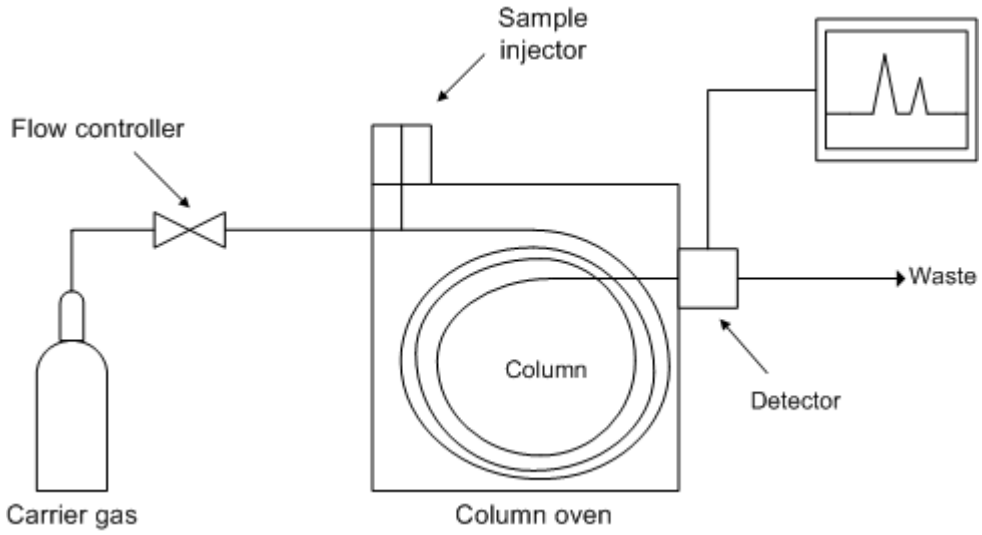

Figure 2. 20: Simplified schematic representation of a GC.

2.2. Thermodynamics

2.2.1. Equilibrium Thermodynamics

Since reforming chemical equations is dealt with in this work, the notation for chemical reactions will have to be established. The reaction,

$\alpha A + \beta B + \cdots \rightleftharpoons \rho R + \cdots$

where $\alpha, \beta,$ ... are molar stoichiometric coefficients such that,

$\rho R + \cdots - \alpha A - \beta B - \cdots = 0$

or

$$\sum_i v_i I = 0 \tag{2.35}$$

where v_i is the stoichiometric coefficient of species I, defined such that v_i is positive for products and negative for the reactants. If N_i is the number of moles of species i at a time t and $N_{i,0}$ is the initial number of moles for species I then N_i and $N_{i,0}$ are related by equation 2.36 as,

$$N_i = N_{i,0} + v_i X \tag{2.36}$$

where X is the molar extent of the reaction. The reason why X is introduced is because it is the same value for each molecular species which takes part in the reaction. This means that given the initial mole numbers of all the species and X at time t, all the other mole numbers in the system can be easily calculated. Thus the change in all mole numbers in the system can be given by the value of X. Considering a single chemical reaction in a closed system occurring at constant temperature and pressure and in a single phase, then the total Gibbs energy for the system is,

$$G = \sum_{i=1}^{C} N_i \bar{G}_i = \sum_{i=1}^{C} \left(N_{i,0} + v_i X\right) \bar{G}_i \tag{2.37}$$

For a closed system at constant temperature and pressure the condition which has to be met for equilibrium is,

$$\left(\frac{\partial G}{\partial X}\right)_{T,P} = 0 \tag{2.38}$$

which works out to,

$$0 = \sum_{i=1}^{C} v_i \bar{G}_i \tag{2.39}$$

since $\sum_i^C N_i \left(\frac{\partial \bar{G}_i}{\partial X}\right)_{T,P} = 0$, according to the Gibbs-Duhem equation. G_i is the partial molar Gibbs energy of the species i at the system conditions.

The chemical reaction system that is looked at in the reforming of methane by carbon dioxide consists of a number of reactions and thus the thermodynamics for a multiple reaction system must be introduced. For this to be done the term of independent chemical reactions is introduced. This term is used to describe the smallest collection of reactions, by forming linear combination variations, which are able to describe all the other chemical reactions among the species present. Because of this description of a set of independent chemical reactions, none of the reactions in this set can be a linear combination of the others. For a multiple reaction, closed, single-phase, constant temperature and pressure system, the number of species at any time is given by,

$$N_i = N_{i,0} + \sum_{j=1}^{\mathcal{M}} v_{ij} X_j \tag{2.40}$$

where the summation is over a set of $\mathcal{M}$ independent reactions. X_j is defined as the molar extent of reaction for the jth independent reaction and v_{ij} is the stoichiometric coefficient for species I in the jth reaction. The Gibbs energy for this system is given by,

$$G = \sum_{i=1}^{C} N_i \overline{G}_i = \sum_{i=1}^{C} \left(N_{i,0} + \sum_{j=1}^{\mathcal{M}} v_{ij} X_j \right) \overline{G}_i \tag{2.41}$$

For chemical equilibrium G must be a minimum or dG = 0 at constant temperature and pressure. Therefore,

$$\left(\frac{\partial G}{\partial X_j} \right)_{T,P,X_{i \neq j}} = 0 \tag{2.42}$$

and thus,

$$\left(\frac{\partial G}{\partial X_j} \right)_{T,P,X_{i \neq j}} = 0 = \sum_{i=1}^{C} v_{i,j} \overline{G}_i + \sum_{i=1}^{C} N_i \left(\frac{\partial \overline{G}_i}{\partial X_j} \right)_{T,P,X_{k \neq j}} \tag{2.43}$$

Since the summation $\sum_{i=1}^{C} N_i \left(\frac{\partial \overline{G}_i}{\partial X_j} \right)_{T,P,X_{k \neq j}}$ disappears because of the Gibbs-Duhem equation the equilibrium criteria is,

$$0 = \sum_{i=1}^{C} v_{i,j} \overline{G}_i \tag{2.44}$$

for all independent reactions j = 1, 2, …, $\mathcal{M}$.

The final concept that needs to be introduced for chemical equilibrium is the equilibrium constant. The standard state definition of the Gibbs energy is,

$$\begin{aligned}\overline{G_i}(T,P,x) &= \overline{G_i^o}(T,P=1bar,x_i^o) \\ &\quad + [\overline{G_i}(T,P,x) - \overline{G_i^o}(T,P=1bar,x_i^o)] \\ &= \overline{G_i^o}(T,P=1bar,x_i^o) + RT\ln\left\{\frac{\overline{f_i}(T,P,x)}{\overline{f_i}^{\circ}(T,P=1bar,x_i^{\circ})}\right\} \\ &= \overline{G_i^o}(T,P=1bar,x_i^o) + RT\ln a_i\end{aligned} \tag{2.45}$$

The a_i is the activity of species I and it is the ratio of the fugacity of species I in the mixture to the fugacity of the species in its standard state. The activity can be described by equation 2.46,

$$\begin{aligned}a_i &= \frac{\overline{f_i}(T,P,x)}{\overline{f_i}^{\circ}(T,P=1bar,x_i^{\circ})} \\ &= exp\left(\frac{\overline{G_i}(T,P,x) - \overline{G_i^o}(T,P=1bar,x_i^o)}{RT}\right)\end{aligned} \tag{2.46}$$

At equilibrium,

$$\begin{aligned}0 = \sum_{i=1}^{C} v_{i,j}\overline{G_i} &= \sum_{i=1}^{C} v_i\overline{G_i^o}(T,P=1bar,x_i^o) + RT\sum_{i=1}^{C} v_i\ln a_i \\ &= \Delta_{rxn}G^{\circ} + RT\sum_{i=1}^{C} v_i\ln a_i\end{aligned} \tag{2.47}$$

$$-\frac{\Delta_{rxn}G^{\circ}}{RT} = \ln\prod_{i=1}^{C} a_i^{v_i} \tag{2.48}$$

where $\Delta_{rxn}G^{\circ}$ is used to describe the term $\sum_{i=1}^{C} v_i\overline{G_i^o}(T,P=1bar,x_i^o)$.

The equilibrium constant is equated to equation 2.48 as,

$$K_a(T) = exp\left(-\frac{\Delta_{rxn}G^{\circ}}{RT}\right) \quad (2.49)$$

and thus

$$K_a(T) = \ln \prod_{i=1}^{C} a_i^{v_i} \quad (2.50)$$

2.2.2. Equilibrium Thermodynamics for system

The reactions taking place during the carbon dioxide reforming of methane are listed as:

$CH_4 + CO_2 \Leftrightarrow 2CO + 2H_2$ (reaction 1)

$H_2 + CO_2 \Leftrightarrow CO + H_2O$ (reaction 2)

$CH_4 + H_2O \Leftrightarrow CO + 3H_2$ (reaction 3)

$2CO \Leftrightarrow C + CO_2$ (reaction 4)

$CH_4 \Leftrightarrow C + 2H_2$ (reaction 5)

$C + H_2O \Leftrightarrow CO + H_2$ (reaction 6)

This set of chemical reactions (reactions 1 to 6) can be reduced by taking into consideration only the independent chemical reactions for the species. The method used to find the independent reactions is Denbigh's method. All the species that are taking part in the reaction system are identified. These species are: H_2O, CO_2, CO, CH_4 and H_2. Denbigh's method requires that the chemical reactions describing the formation of the molecular species in the system be formulated.

$2H + O \Rightarrow H_2O$ (reaction 7)

$C + 2O \Rightarrow CO_2$ (reaction 8)

$C + O \Rightarrow CO$ (reaction 9)

$C + 4H \Rightarrow CH_4$ (reaction 10)

$2H \Rightarrow H_2$ (reaction 11)

Since neither atomic hydrogen nor atomic oxygen are present at the reaction conditions, these species must be eliminated by the process of addition and/or subtraction. Using reaction 11 and 7 ($H = ½\ H_2$ & $O = H_2O - H_2$) which yields the following set of independent reactions:

$CO_2 + 2H_2 \Rightarrow C + 2H_2O$ (reaction 12)

$C + H_2O \Rightarrow CO + H_2$ (reaction 13)

$CH_4 \Rightarrow C + 2H_2$ (reaction 14)

In order to calculate the number of moles at equilibrium Table 2.3 is used, where the molar extent of the reactions 12 to 14 are X_1, X_2 and X_3 respectively.

Table 2. 3: The number of moles in the system.

	Initial	**Final**	**Equilibrium mole fraction**
H_2O	0	$2X_1 - X_2$	$(2X_1 - X_2)/\sum$
CO_2	Ni_{CO2}	$Ni_{CO2} - X_1$	$(Ni_{CO2} - X_1)/\sum$
CO	0	X_2	$X_2/\sum$
H_2	0	$-2X_1 + X_2 + 2X_3$	$(-2X_1 + X_2 - 2X_3)/\sum$
CH_4	Ni_{CH4}	$Ni_{CH4} - X_3$	$(Ni_{CH4} - X_3)/\sum$
C	0	$X_1 - X_2 + X_3$	$(X_1-X_2+X_3)/\sum$
Total	$Ni_{CO2} + Ni_{CH4}$	$\sum = Ni_{CO2} + Ni_{CH4} + 2X_3$	

Table 2.4 shows the number of moles table if the carbon is not considered because it does not appear in the gaseous phase.

Table 2. 4: Number of moles in the system for the gaseous species.

	Initial	**Final**	**Equilibrium mole fraction**
H_2O	0	$2X_1 - X_2$	$(2X_1 - X_2)/\sum$
CO_2	Ni_{CO2}	$Ni_{CO2} - X_1$	$(Ni_{CO2} - X_1)/\sum$
CO	0	X_2	$X_2/\sum$
H_2	0	$-2X_1 + X_2 + 2X_3$	$(-2X_1 + X_2 + 2X_3)/\sum$
CH_4	Ni_{CH4}	$Ni_{CH4} - X_3$	$(Ni_{CH4} - X_3)/\sum$
Total	$Ni_{CO2} + Ni_{CH4}$	$\sum = Ni_{CO2} + Ni_{CH4} - X_1 + X_2 + X_3$	

Using Table 2.4 as the number of moles in the system, the three equilibrium coefficients are:

$$K_{a,1} = \frac{y_{H_2O}^2}{y_{CO_2} y_{H_2}^2} \tag{2.51}$$

$$K_{a,2} = \frac{y_{CO} y_{H_2}}{y_{H_2O}} \tag{2.52}$$

$$K_{a,3} = \frac{y_{H_2}^2}{y_{CH_4}} \tag{2.53}$$

If carbon is included in the equilibrium system, then:

$$K_{a,1} = \frac{y_c y_{H_2O}^2}{y_{CO_2} y_{H_2}^2} \tag{2.54}$$

$$K_{a,2} = \frac{y_{CO} y_{H_2}}{y_c y_{H_2O}} \tag{2.55}$$

$$K_{a,3} = \frac{y_c y_{H_2}^2}{y_{CH_4}} \tag{2.56}$$

where y is the molar fraction of the component.

The Ka's for the independent reactions are obtained using a program by Sandler, 2006. The extents of the reactions can then be found by solving the equations. Mathcad is used to obtain

the roots of this system. The feed ratio from the experiments of the CH_4 and CO_2 is calculated as:

CH_4:

$$0.487\frac{l}{min} \times 0.717\frac{g}{l} \div 16.043\frac{g}{mol} = 0.02177\frac{mol}{min}$$

CO_2:

$$0.487\frac{l}{min} \times 1.98\frac{g}{l} \div 44.01\frac{g}{mol} = 0.02191\frac{mol}{min}$$

The molar feed ratio is:

$$\frac{N_{CH_4}}{N_{CO_2}} = \frac{0.9936}{1} \approx 1$$

The Gibbs free energies can also be used to calculate the equilibrium compositions. Equations 2.57, 2.58 and 2.59 are the set of equations that must be solved simultaneously to get the equilibrium compositions.

$$y_i = \frac{N_{io} + \sum_j v_{i,j}\varepsilon_j}{N_o + \sum_j v_j\varepsilon_j} \tag{2.57}$$

Where, $v_{i,j}$ is the stoichiometric coefficient of species i in reaction j and ε_j is the equilibrium reaction coordinate for reaction j (similar to the extent of reaction above).

$$exp\frac{-\sum_i v_i G_i^o}{RT} \equiv K_j \tag{2.58}$$

Where, K is the equilibrium constant.

$$\prod_i (y_i)^{v_{i,j}} = \left(\frac{P}{P^o}\right)^{v_j} K_j \tag{2.59}$$

Where, P is operating pressure and P^o is atmospheric pressure.

These equations are solved using Mathcad as shown in Appendix 1.

CHAPTER THREE

3.0 Methods and Procedure

A catalytic CVD is used for the production of the carbon nanotubes and nanofibres in this study. The gasses used in these experiments are all Ultra High Purity (UHP) gasses and they were supplied by AFROX (African Oxygen) Ltd. The catalysts (Table 3.1) used are all obtained from Sigma Aldrich and were used as received with no extra preparation or enhancements done on them. The amount of catalyst used is approximately 10 g for every experiment done (unless otherwise stated). The catalyst is placed on top of quartz wool which is located approximately 28 cm inside the tube, from the bottom. The tube used is a mullite tube of diameter 50 mm and length 1050 mm which is placed vertically inside of an electric furnace (Figure 3.1).

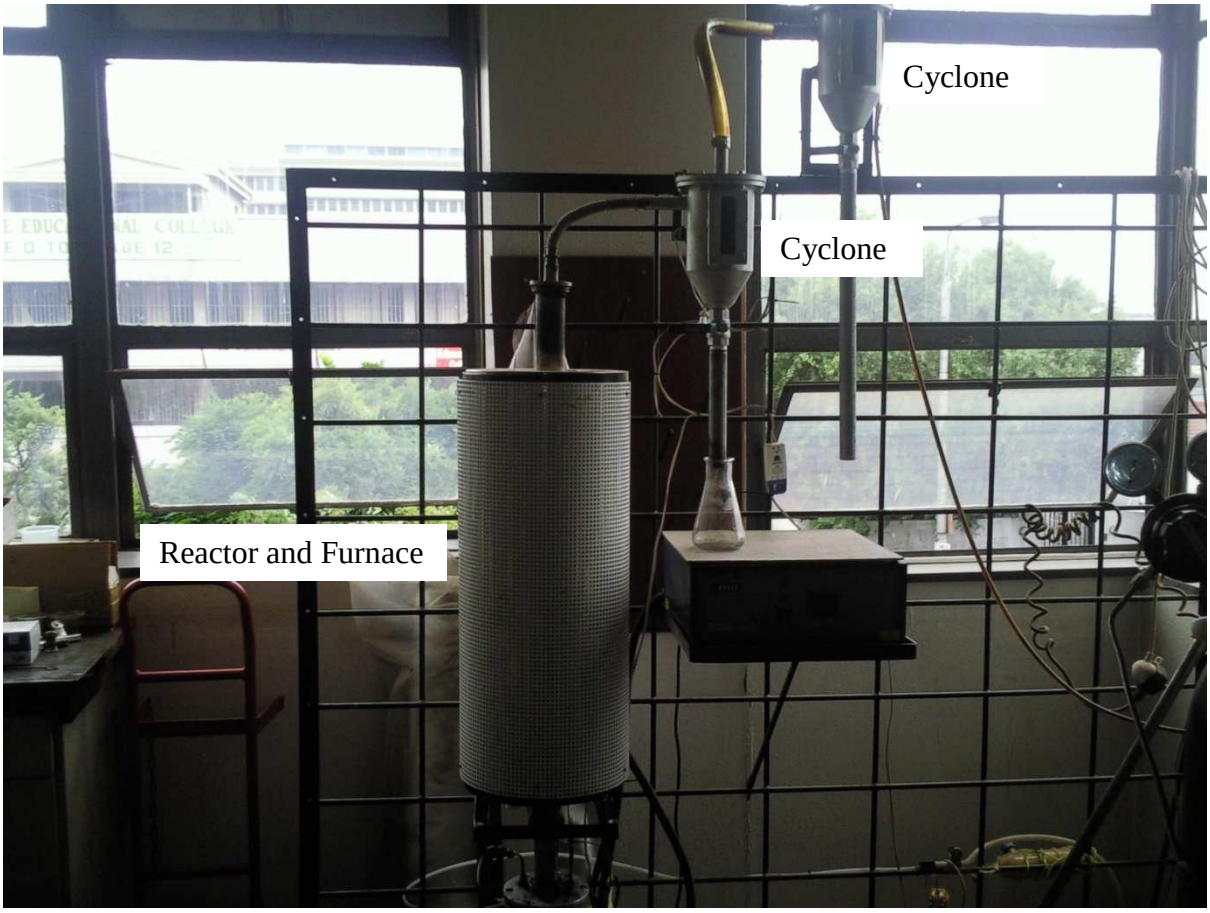

Figure 3. 1: Vertical CVD used for the experiments.

Before the start of each experiment argon is passed through the system in order to detect leaks, purge any gasses which may still be in the system and prevent the formation of nitrites (Kuwana et. al., 2005). The argon is also allowed to remain flowing throughout the experiment (at 487 ml/min). Table 3.1 lists the experiments which are considered in this work and the conditions at which they were carried out. The temperatures are based on the acceptable temperature ranges for carbon dioxide reforming of methane. The CO_2 decomposition temperatures are chosen because of the temperatures suggested in section 2.1.5.

Table 3. 1: Conditions at which the experiments are carried out.

No.	CO_2 (ml/min)	CH_4 (ml/min)	Temperature (^oC)	Catalyst	Time of Reaction (min)
1	487		750	$LaNi_5$ alloy	20
2	487		850	$LaNi_5$ alloy	20
3	248		750	1% Pt. on Alumina (2.5 g)	30
4	487		750	Ni (2.5 g) & LaO_5 (2.5 g)	20
5	487		650	$LaNi_5$ alloy	45
6	487		700	$LaNi_5$ alloy	20
7	487		800	Mischmeta-Nickel alloy	15
8		248-487	750	$LaNi_5$ alloy	12
9		487	650	$LaNi_5$ alloy	28
10		487	850	$LaNi_5$ alloy	17
11	487	487	750	$LaNi_5$ alloy	41
12	487	487	850	$LaNi_5$ alloy	18
13	487	487	750	Mischmetal-Nickel alloy	30
14	487	487	850	Mischmetal-Nickel alloy	25
15	487	487	950	$LaNi_5$ alloy	38
16	487	487	950	Mischmetal-Nickel alloy	31
17	487	487	750	Ni (4 g) & LaO_5 (8 g)	29

From experiment 7-17 Argon is no longer used while the experiment is taking place because the product does not get carried out of the system to the cyclones. The carbon products are characterised using a low magnification transmission electron microscope (TEM), Joel JEM 100S, operating at 80 kV. 5 ml of methanol is added to the sample which is then placed in a sonic bath for 10 min. A few drops of the suspension are then dropped onto a holey carbon film with a copper grid which is placed into the microscope. For the high resolution images the CM 200 microscope is used. A Raman spectrometer is also used to characterise the samples obtained. The equipment used is the Jobin-Yvon T6400 Raman spectrometer operated in single spectrograph mode with micro-Raman attachment. The laser used is a 514.5 nm line of an argon ion laser. The characterisation is done at the standard room temperature and the power of the sample is kept low (approximately 1.2 mW) in order to minimise local heating of the sample.

The gas that comes out of the system is collected and analysed using the Agilent 6820 gas chromatography (GC). The carrier gas used is argon because the GC operates on the gas stream's Thermal Conductivity Differences and argon has a low thermal conductivity because of its inert properties. Table 3.2 gives the description of the column used. The argon flow is kept at 10 psi for the duration of the gas analysis. The initial temperature used is 35°C and the oven is kept at this temperature for 5 minutes before the ramping program is started. The temperature is increased at a rate of 20°C per minute to the maximum temperature of 150°C. The oven is kept at this temperature for 3 more minutes. The complete cycle takes 13.75 minutes to complete. The approximate retention times of the reforming gasses are found in Table 3.3.

Table 3. 2: Data for the column used in the GC

Column material	**Stainless steel**
Length	2 m
Outer diameter	1/8 inch (3.175 mm)
Internal diameter	2.2 mm
Support	Carboxen-1000
Mesh range	60/80

Table 3. 3: Retention time of gasses

Component	**Approximate time (min)**
H_2	< 0.41
CO	1.2 – 1.8
CH_4	4.8 – 5.3
CO_2	8.3 – 8.8

CHAPTER FOUR

4.0 Results and Discussion

4.1. Results

4.1.1. TEM Images of Carbon Nanofibres (CNFs) produced with CO_2

The TEM images below are those obtained from the experiments done. More images of experiments done at these conditions are available in the appendix.

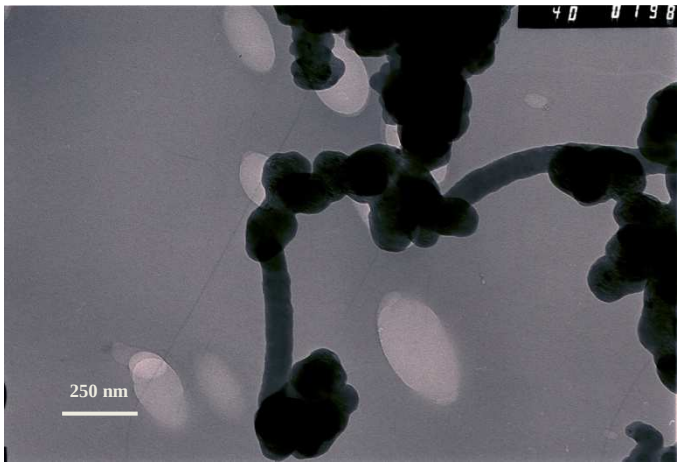

Figure 4. 1: CNFs produced at 750°C using Lanthanum-Nickel alloy.

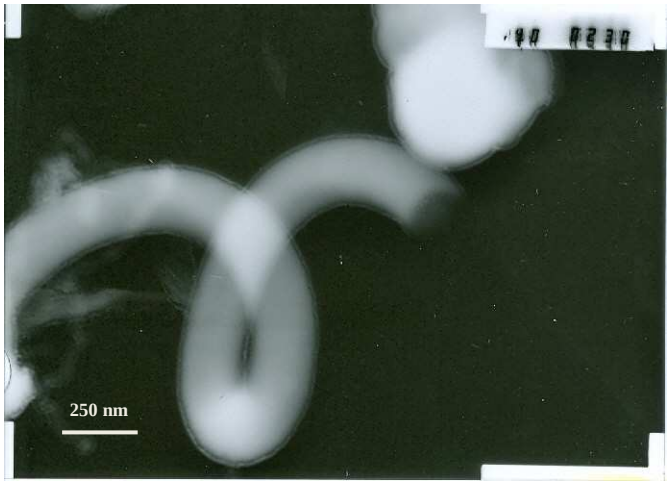

Figure 4. 2: CNF produced at 850°C using Lanthanum-Nickel alloy.



Figure 4. 3: TEM image of the CNF on the nickel catalyst.

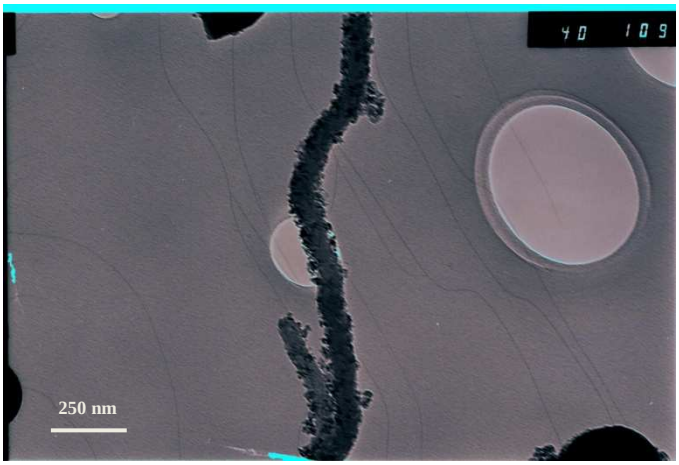

Figure 4. 4: CNF produced at 750°C using Platinum on alumina powder.

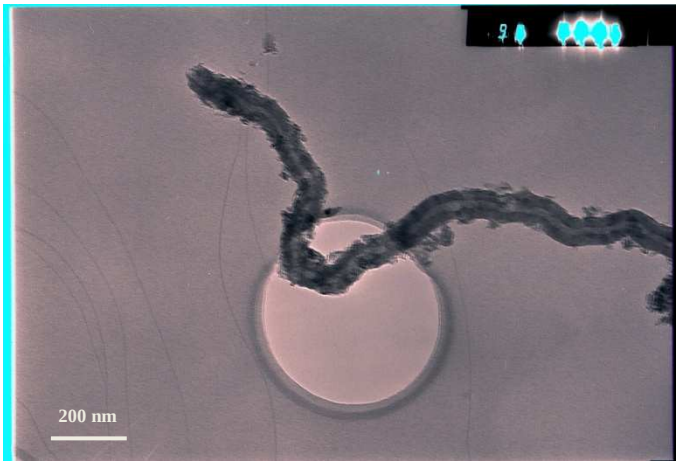

Figure 4. 5: Possible CNT from CO_2 source.

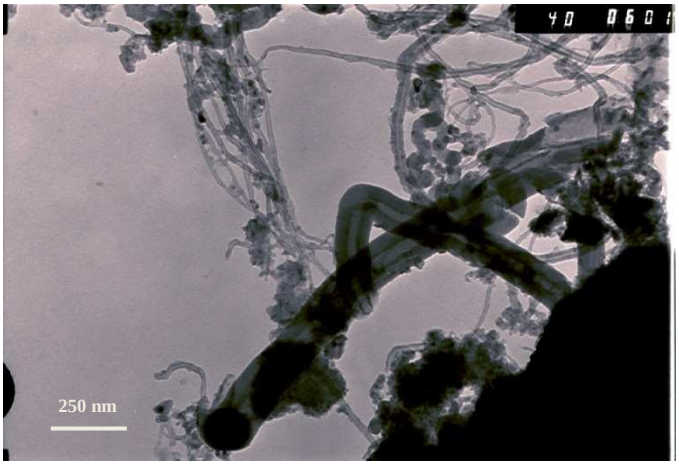

Figure 4. 6: CNFs and CNTs produced at 650°C using Lanthanum-Nickel alloy.

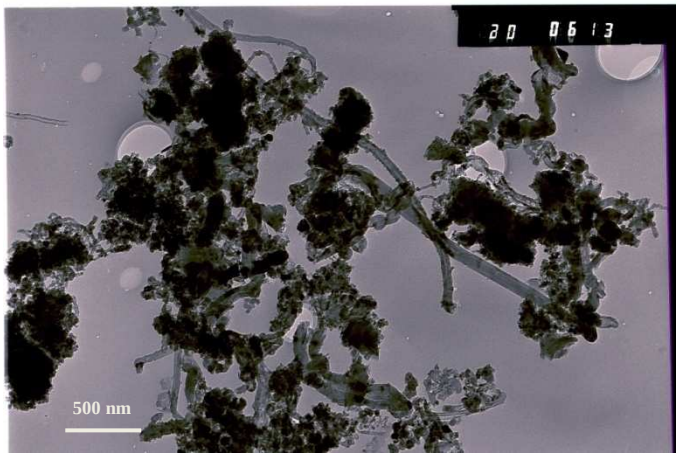

Figure 4. 7: CNTs and CNFs produced at 700°C using Lanthanum-Nickel alloy.

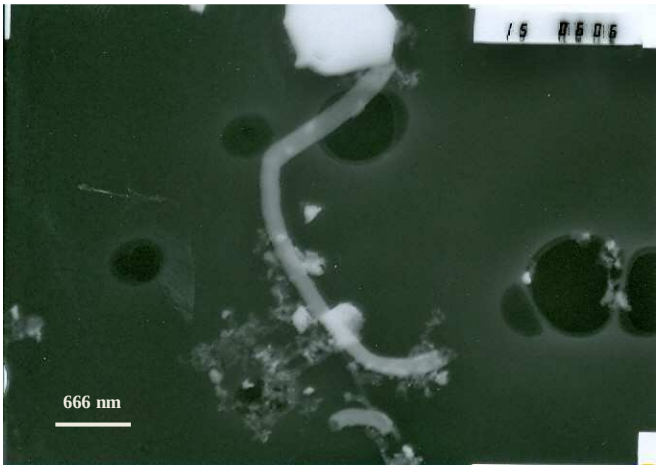

Figure 4. 8: CNFs produced at 800°C using Mischmetal-Nickel alloy.

At 750°C CNFs are produced using $LaNi_5$ catalyst (Figure 4.1). These fibres are attached to the catalyst particles (bright white on the TEM image) on their ends. The diameter of the fibre in this image is 72.5 nm. In Figure 4.2 the CNF has a diameter of 217.5 nm and does not seem to have any catalyst particles embedded inside its structure. The CNF also displays the circular structure that is expected. This CNF is produced at 850°C using $LaNi_5$. The CNF in Figure 4.3 is produced at the same conditions as Figure 4.2. This TEM image displays the catalyst particle at the beginning of the fibre and that the catalyst has the same diameter as the CNF. Figure 4.4 is a CNF approximately 1.44 μm and does not have any catalyst particles inside its structure and at the end of the fibre. This CNF is produced at 750°C using a platinum and alumina powder catalyst. At these conditions there may be CNTs being formed (Figure 4.5). Figure 4.6 clearly shows that Carbon Nanotubes (CNTs) are formed at 650°C using $LaNi_5$ as a catalyst. Some of the CNTs and CNFs grow from the large catalyst particle in the image. The CNFs and CNTs in Figure 4.7 are produced at 700°C using $LaNi_5$ as the catalyst. The longest of the fibres in the TEM image is approximately 2.3 μm. The catalyst particles are visible in the image and other carbon. Figure 4.8 displays CNFs produced at 800°C using a mischmetal-nickel alloy as the catalyst. The fibres are relatively free of any catalyst particles in their structure and the longest one is 3.6 μm.

4.1.2. TEM images of CNTs produced with Methane

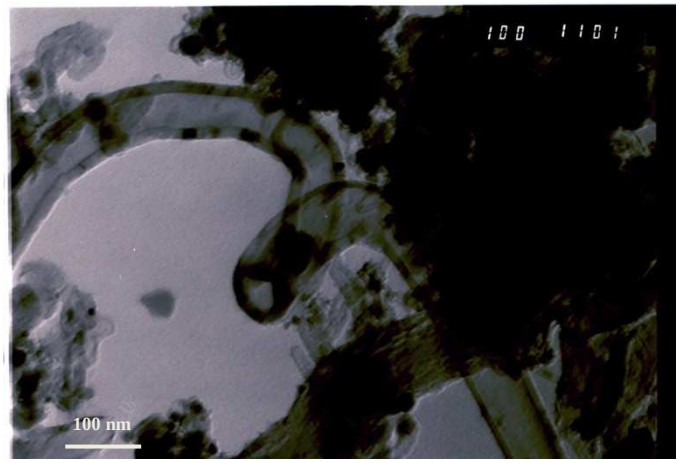

Figure 4. 9: CNTs produced at 750°C using Lanthanum-Nickel alloy.

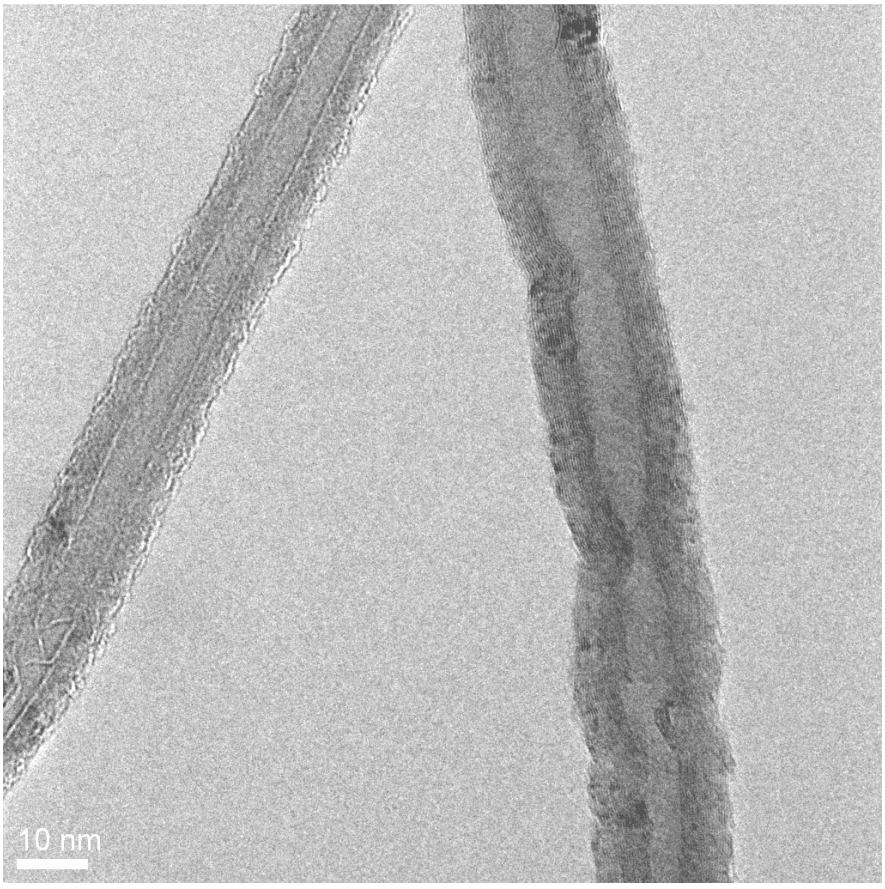

Figure 4. 10: High resolution transmission electron microscope (HRTEM) image of the CNTs produced in Figure 4.8 above.

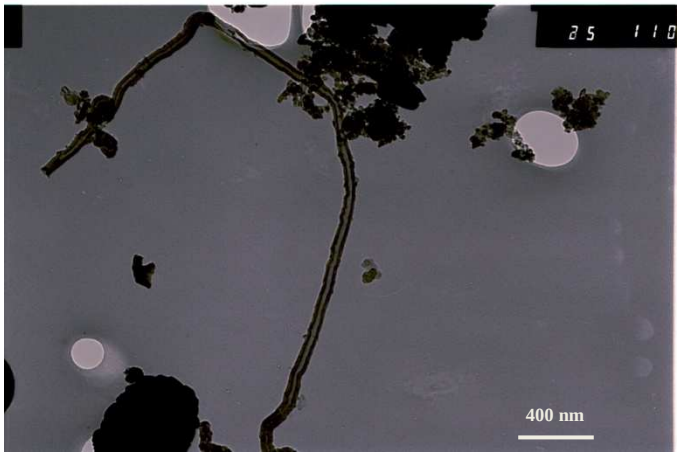

Figure 4. 11: Very long CNT produced at 650°C using Lanthanum-Nickel alloy.



Figure 4. 12: HRTEM image of CNT produced at 650°C using Lanthanum-Nickel alloy.

Figure 4.9 and 4.10 are produced at 750°C using $LaNi_5$ as the catalyst. Figure 4.9 clearly shows the hollow structure of the nanotube and Figure 4.10 shows the multiple wall structure of the nanotubes produced. Figure 4.11 and 4.12 display CNTs produced at 650°C using $LaNi_5$ as the catalyst. The CNT in Figure 4.9 is approximately 3.5 μm in length and most of it is uncontaminated by the catalyst. The HRTEM image shows the multiple walls forming the multi wall carbon nanotube (MWCNT).

4.1.3. Images obtained when CO_2 reforming of CH_4 has taken place



Figure 4. 13: CNTs produced at 750°C using Lanthanum-Nickel alloy.

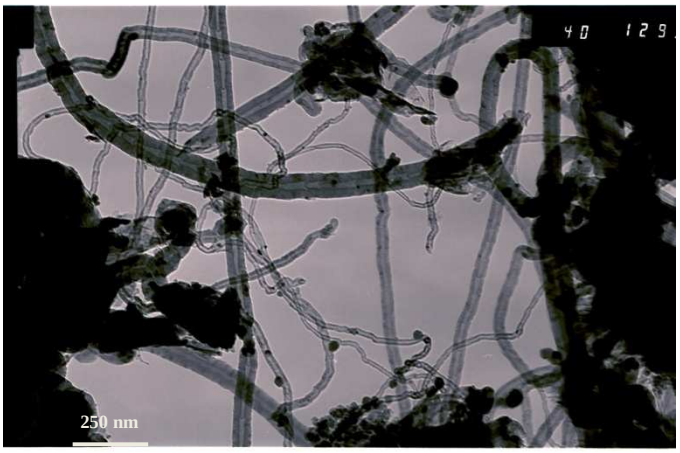

Figure 4. 14: Network of CNTs produced at 750°C using Mischmetal-Nickel alloy.



Figure 4. 15: CNT produced at 850°C using Mischmetal catalyst.

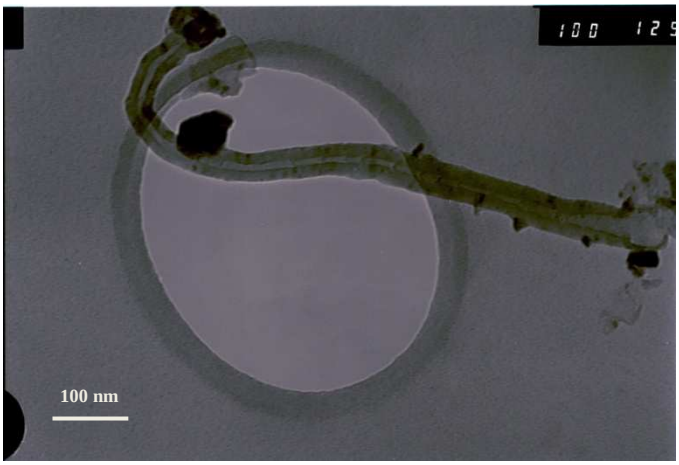

Figure 4. 16: CNT not fully formed.

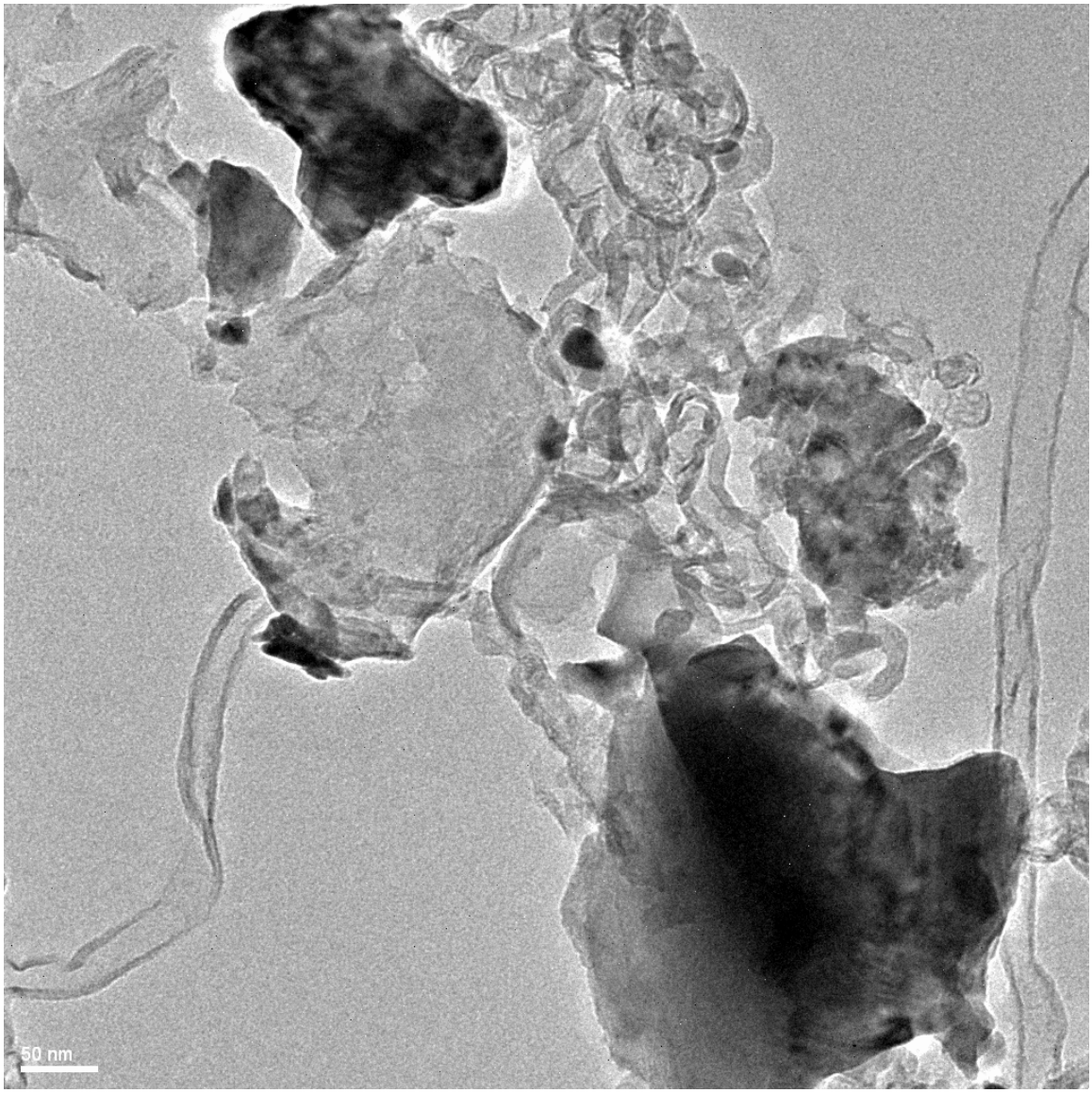

Figure 4. 17: HRTEM image of the catalyst (dark spot) and the carbon deposition (grey).

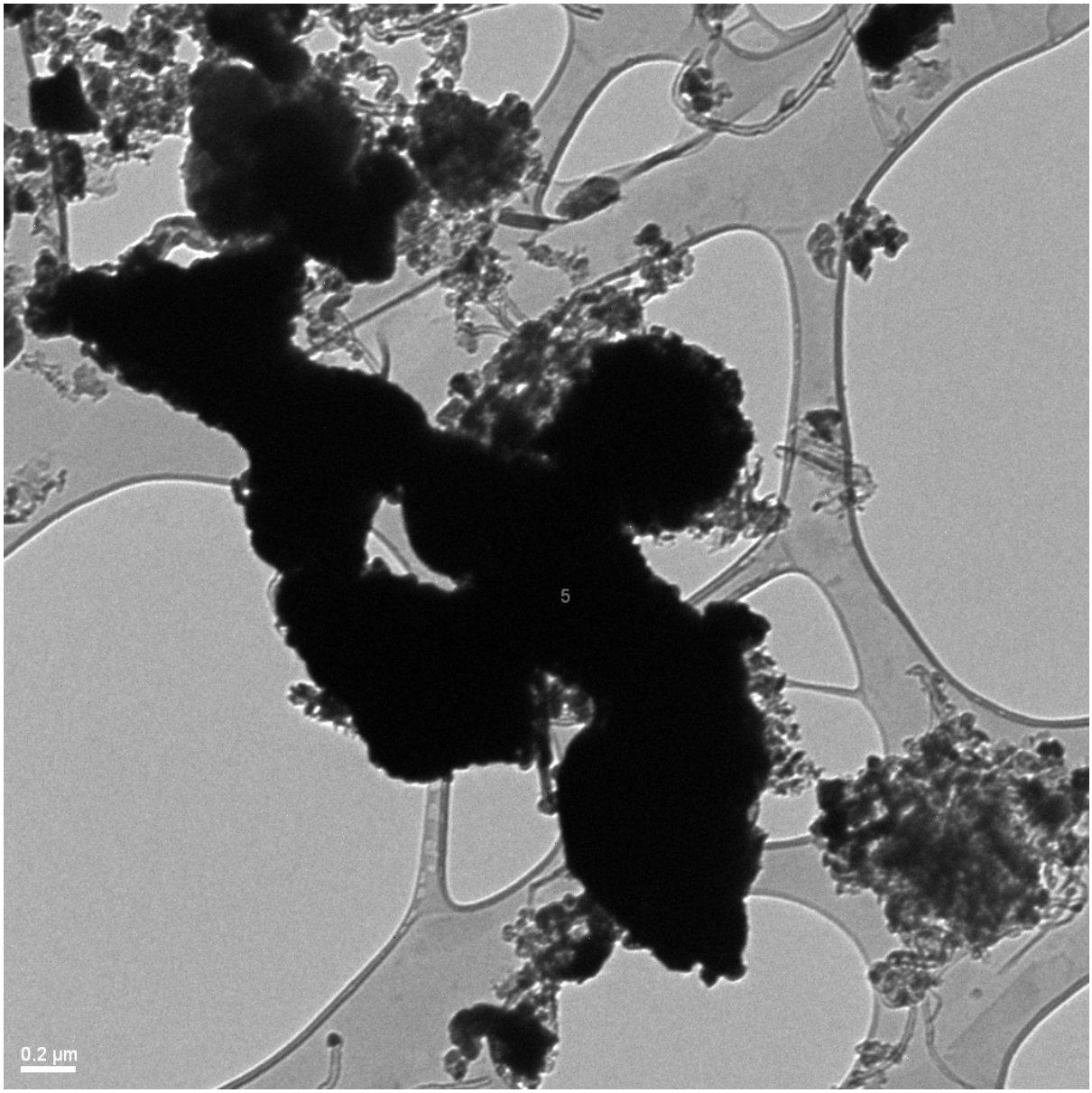

Figure 4. 18: Few CNTs are produced at 950°C.

Figure 4.13 and 4.14 show that CNTs have been formed when dry reforming takes place at 750°C and the catalysts used are $LaNi_5$ and mischmetal-nickel alloy respectively. The CNTs produced with mischmetal have a much better structure than the ones formed with the Lanthanum. Figure 4.15 and 4.16 show carbon nanotubes produced at 850°C using the mischmetal catalyst. Some of the CNTs lose their circular shape before the completion of their growth (Figure 4.16). At 950°C using the mischmetal catalyst very few CNTs are

formed as displayed in Figure 4.18. Figure 4.17 shows filamentous carbon and carbon deposits but no CNTs.

4.1.4. Gas Chromatography Analysis

The results for the GC runs done on some of the samples are tabulated according to the conditions that the experiments were carried out. The unknown gasses are those that are not calibrated for before the GC runs. Table 4.1 shows that CO_2 is decomposed during the experiments at 650 and 750°C to O_2 and CO. There is also a decomposition of CH_4 to H_2 and other hydrocarbons that were not calibrated for. The results also show that reforming does take place for the temperature range tested (750°C – 950°C). The best reforming result occurred at 950°C using Mischmetal-nickel alloy as the catalyst as there is a higher percentage of syngas in the outflow.

Table 4. 1: Gas chromatography results

Inlet Gas	**Catalyst**	**Time of Reaction (min)**	**Temperature (^{o}C)**	**Output Gas**
CO_2	Ni & LaO_5 powder	20	750	0.06% O_2 12.03% CO 87.91% CO_2
CO_2	$LaNi_5$	35	650	5.33% O_2 2.02% CO 92.65% CO_2
CH_4	$LaNi_5$	12	750	13.65% H_2 28.02% unknown 58.33% CH_4
CH_4	$LaNi_5$	30	850	17.52% H_2 15.02% unknown 67.46% CH_4
CH_4 CO_2	$LaNi_5$	30	750	10.27% H_2 11.3% CO 35.59% CH_4 42.84% CO_2
CH_4 CO_2	$LaNi_5$	18	850	11.66% H_2 5.83% CO 34.51% CH_4 48% CO_2
CH_4 CO_2	Mischmetal-Nickel alloy	30	750	14.18% H_2 9.67% CO 8.97% CH_4 67.18% CO_2
CH_4 CO_2	Mischmetal-Nickel alloy	31	950	49.51% H_2 25.21% CO 8.61% CH_4 16.67% CO_2

4.1.5. Raman Spectrometer Analysis

The Raman spectres for some of the samples are displayed below. The rest of the Raman graphs are given in the Appendix.

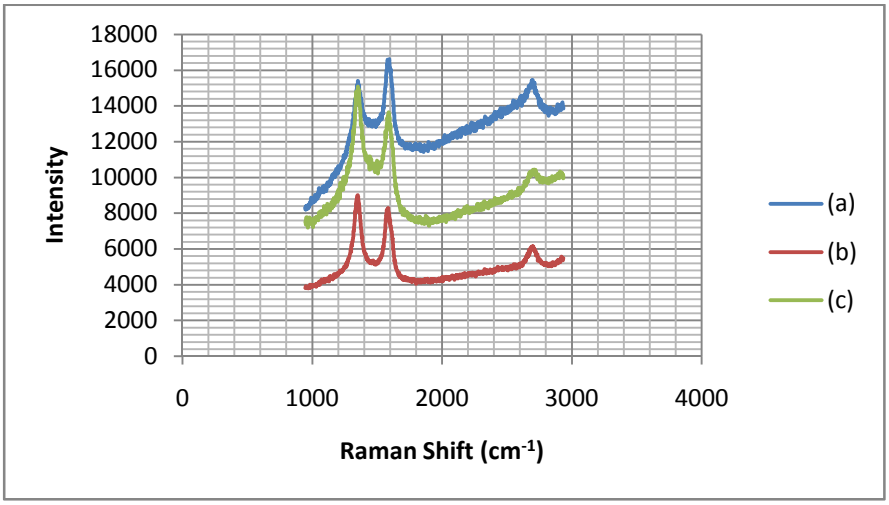

Figure 4. 19: The Raman Shifts of a) CNTs produced at 650°C using CO_2; b) CNTs produced at 750°C using CH_4; c) CNTs produced at 750°C during CO_2 reforming of CH_4.

From all three images in Figure 4.19 it can be seen that the peaks correspond to those that signify the presents of carbon nanotubes. The first peak is between 1300 and 1400 cm^{-1} (D-band), the second is just before 1600 cm^{-1} (G-band) and the last at 2700 cm^{-1} (G'-band). These Raman readings are taken from the carbon product. The Raman spectres of the images in Figure 4.20 below are taken from the catalyst particles.

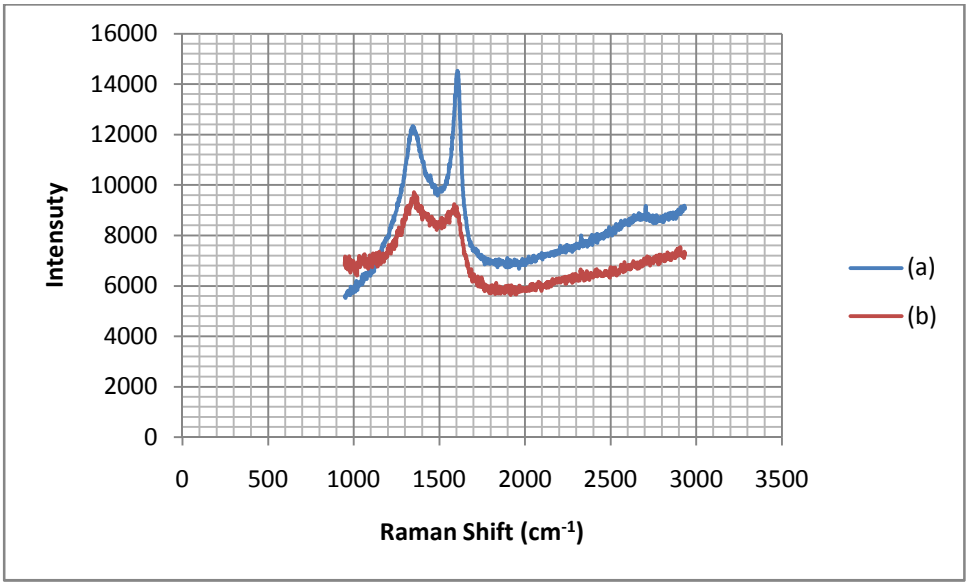

Figure 4. 20: Raman Shift caused by the catalyst particles resembling that caused by the carbon products.

Figure 4.20 shows that the Raman shift due to the carbon product appears on the catalyst as well. The graphs themselves are not as well defined as those in Figure 4.19.

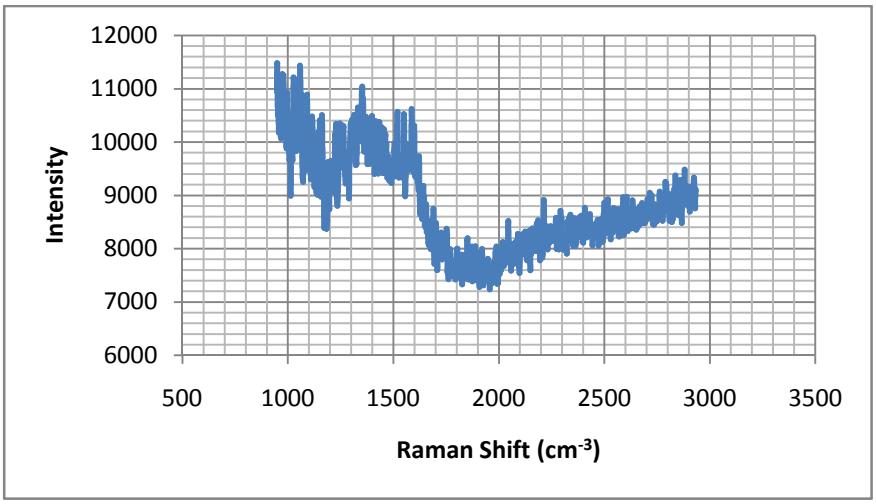

Figure 4. 21: Raman shift of sample when CNTs are not formed during reforming.

Figure 4.21 is from a sample which did not display any CNTs being formed on the TEM images. This is re-affirmed by the Raman Shift peaks not following the same pattern as the ones in Figure 4.19.

4.1.6. Thermodynamics

The following graphs are generated using the data obtained from the Mathcad calculations.

Figure 4.23 is obtained from calculation 1 and Figure 4.22 from calculation 2 in the appendix.

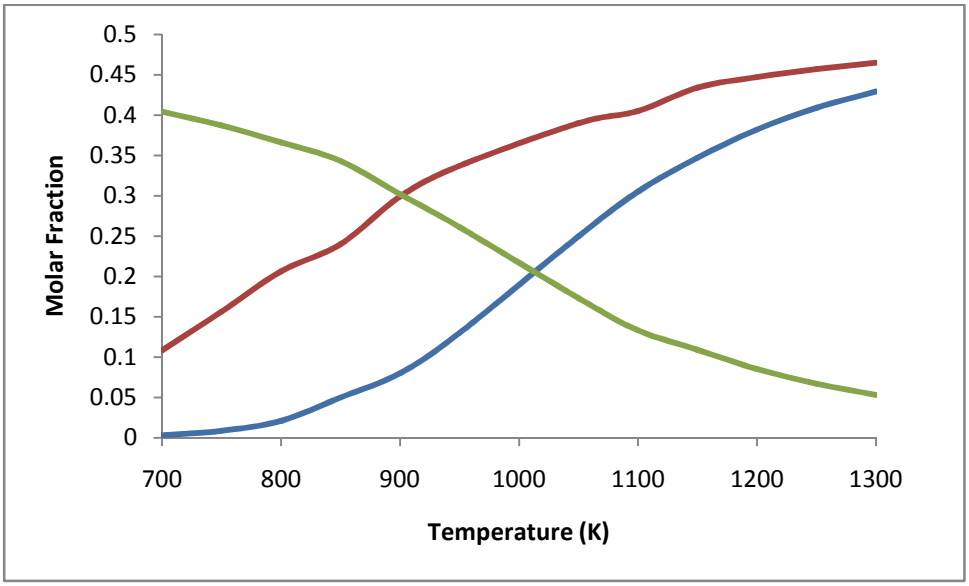

Figure 4. 22: Calculation 2 thermodynamic equilibrium compositions of a) carbon monoxide, b) hydrogen and c) carbon.

a)

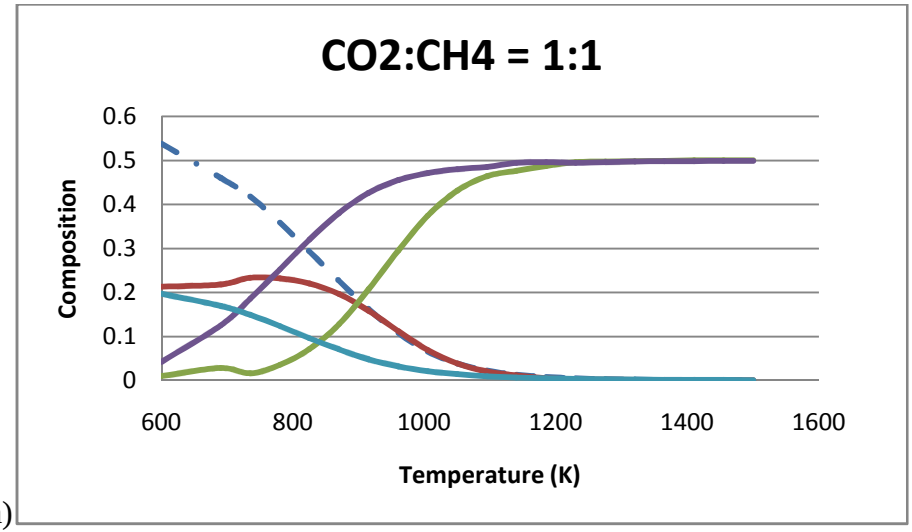

b)

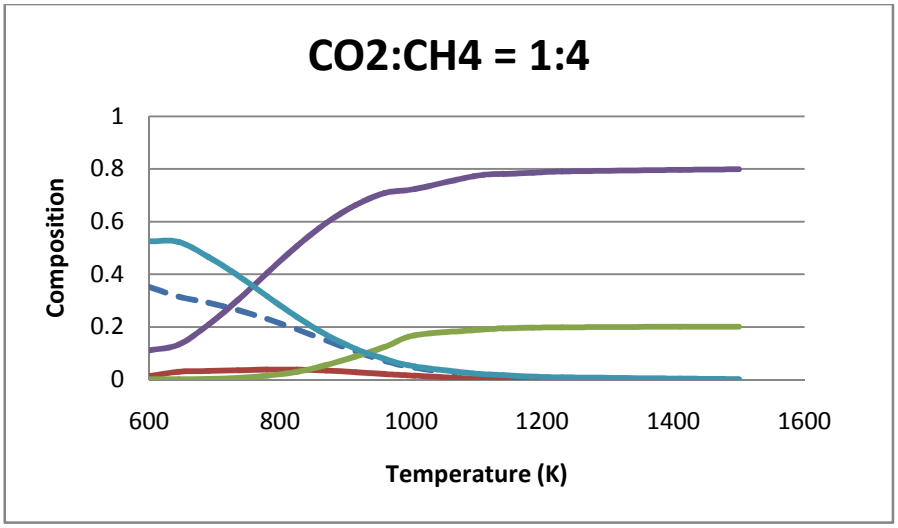

c)

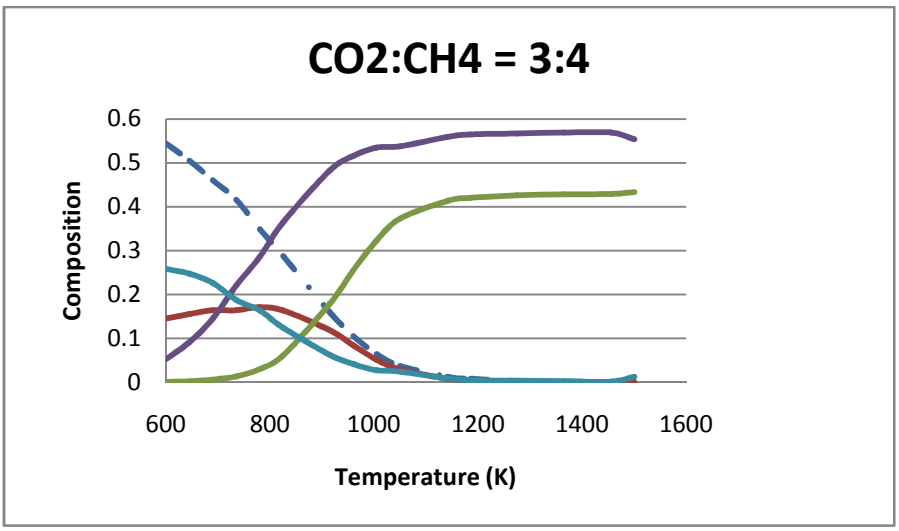

Figure 4. 23: Calculation 1 thermodynamic equilibrium compositions using different CO_2:CH_4 ratios.

4.2. Discussion

From Figure 4.1 to Figure 4.8 it is easy to see that CNFs are produced using CO_2 at temperatures from 650 to 850^oC. At 650 and 700^oC there are CNTs being produced (Figure 4.6 and 4.7). This means that at the relatively low temperatures it is possible to produce CNTs from CO_2 alone. The CNFs become more distinct as the temperature increases as can be seen at 800 and 850^oC. The reason for the breakdown of the CO_2 is because of the catalysts used. Lanthanum is part of the rare earth metal group which are able to chemically decompose CO_2 into CO, C and O_2 (as shown in section 2.1.5.) Mischmetal on the other hand is a combination of rare earth metals and a few other transition metals (which also encourage the production of CNTs) and thus also retains the ability to decompose CO_2. Methane produces well defined CNTs at all tested temperatures as it has already been documented (Chai et al., 2007). The most commonly used catalyst in the decomposition of methane to CNTs is nickel (He et al., 2006 and Qian et al., 2004). Because of this reason methane is decomposed easily enough by the two catalysts used. During the reforming of methane by carbon dioxide CNTs and CNFs are produced at 750^oC but these carbon species become less defined at 850^oC (Figure 4.17) and they are almost non-existent at 950^oC. From the TEM images it seems that hydrogen does play a role in the selection of the carbon species that will be produced. When using CO_2 alone to produce CNFs it is possible to produce CNTs at relatively lower temperatures but they will not be as clearly defined as those that are produce with CH_4. At higher temperatures it is only possible to produce CNTs when hydrogen is involved in any form. From the GC results it is shown that CO_2 and CH_4 are both broken down during the experiments. The Raman spectra show that CNTs are produced during all the experiments that are done including those of CO_2. This may be true but in the case of the CO_2 the CNTs would have to have been few and far between as they did not register on the TEM images. The Raman shifts of the catalyst particles are also taken into account. For most

of the samples they show that there are CNFs growing on the catalyst except in Figure 4.21 where there is clearly no carbon graphite product detected by the Raman laser. This could be true since less carbon products are found in the TEM images. A probe mechanism in the HRTEM is used to determine the compounds in Figure 4.18 on the dark part. Figure 4.24 below gives the data that is obtained.

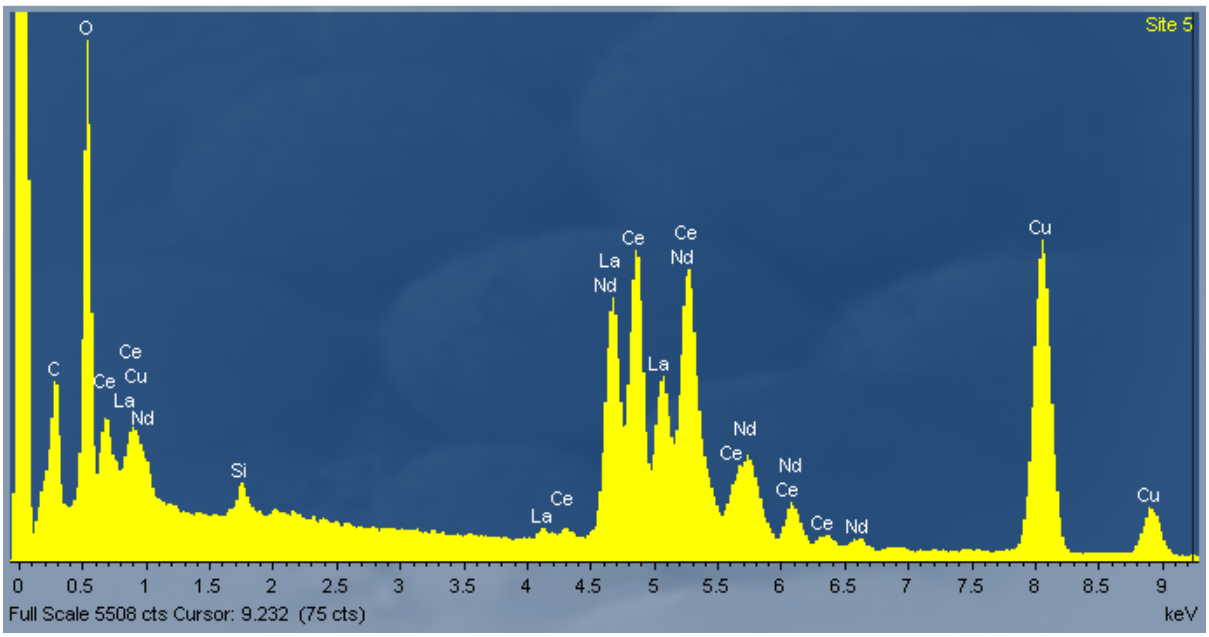

Figure 4. 24: Composition of the catalyst particle after reforming.

From Figure 4.24 it is clear that some carbon is on the catalyst particle but it is very small. This means that at high temperatures the $LaNi_5$ and to a higher extent the Mischmetal-Nickel alloy do not coke as readily as some reforming catalysts and thus will be effective for the dry reforming of methane by carbon dioxide. The thermodynamics are checked for the effect of temperature and the effect of the feed stream concentrations. The increase in temperature does two things. First it decreases the amount of water produced by the reactions until around 1200 K where it becomes negligible. At lower temperatures there is a large quantity of water being produced. The second is that the yield of syngas increases till it approaches 100% at the

high temperatures. Figure 4.22 displays the same trend given by Figure 4.23 and it also shows the carbon fraction at different temperatures. This carbon data agrees with the notion passed above that the carbon deposition on the catalyst (and thus CNT and CNF production) decreases as the temperature increases. The change of the initial CO_2:CH_4 ratio changes the final CO:H_2 ratio. The change in the final ratio is by approximately the same factor that the initial ratio is changed. Since the most desirable ratio in reforming is the CO:H_2 = 1:1 the thermodynamic model that will be used is where CO_2:CH_4 = 1:1.

The thermodynamic model does not match the results given by the GC exactly because of the reaction mechanisms that take place and the thermodynamics only takes into account the effect of temperature on the system. The production of carbon on the catalyst deactivates the catalyst and thus the most accurate account of the system will only be obtained when the kinetics of the system are taken into account. Another problem is that the Gibbs free energy of carbon nanotubes is not equal to that of carbon (as assumed in this study). Although this assumption is used widely (especially when reforming is considered where the carbon is taken as coke formation) the CNTs are not just graphite (Li et al., 2008). Their curvature, length, diameter and chirality influence their Gibbs free energy which is used for thermodynamic calculations. Because the experimental setup of this work is such that the length, diameter and chirality of the CNTs cannot be determined before hand and because approximately all CNTs produced have different lengths, diameters and chirality, there will be a near infinite number of Gibbs free energies for the carbon species.

CHAPTER FIVE

5.0 Conclusion and Recommendations

5.1. Conclusion

The aim of this work was to produce carbon nanofibres and syngas from the greenhouse gasses carbon dioxide and methane. Carbon nanofibres (and carbon nanotubes) are produced using CO_2, CH_4 and CO_2/CH_4 mixture. This means that carbon dioxide can be decomposed at reasonable temperatures and its products used in a number of ways. During the CO_2 reforming of CH_4, CO_2 is still decomposed and syngas is produced at relatively high temperatures. This process has existed for some time but always had a problem with fast catalyst degradation. The catalyst used can withstand coking at high temperatures without being treated or prepared. This means the catalyst can be reused with very little treatment in between. A suitable catalyst for the dry reforming of methane is a Mischmetal-nickel alloy and the conditions should be temperatures in the 900^oC range. Methane has already been established as a viable feed to the production of carbon nanotubes and is often used. Carbon dioxide on the other hand is not. Although it is possible to produce CNTs using CO_2 it would be very costly to do it at an industrial scale as one would need a huge recycle stream (which increases costs.)

5.2. Recommendations

For a more accurate comparison between the experimental results and theory it is recommended that the kinetics of the system have to be taken into account. The kinetics will also include the effect that catalyst deactivation has on the system. For the thermodynamics

to be more accurate, detailed studies on the effect that the curvature and the chirality of the CNTs have on the Gibbs energy will have to be done.

References

Alie, C., Backham, L., Croiset, E., Douglas, P.L., 2005, Simulation of CO_2 capture using MEA scrubbing: a flowsheet decomposition method, Energy Conversion and Management 46 475–487.

Arakawa, T., Suezawa, N., Adachi, G., Shiokawa, J., 1988, Dissociation of CO_2 on some rare earth metal thin films, Applied Surface Science 33/34 286-291.

Belin, T., Epron, F., 2005, Characterization methods of carbon nanotubes: a review, Materials Science and Engineering B 119 105–118.

Chai, S., Hussein, S., Zein, S., Mohamed, A.R., 2007, Synthesizing carbon nanotubes and carbon nanofibres over supported-nickel oxide catalysts via catalytic decomposition of methane, Diamond and Related Materials 16 1656 - 1664.

Chiavassa, D. L., Barrandeguy, J., Bonivardi, A. L., Baltana´s, M. A., 2008, Methanol synthesis from CO2/H2 using Ga2O3–Pd/silica catalysts: Impact of reaction products, Catalysis Today.

Daenen, M., de Fouw, R.D., Hamers, B., Janssen, P.G.A., Schouteden, K., Veld, M.A.J., 2003, The Wondrous World of Carbon Nanotubes ‘a review of current carbon nanotube technologies’, Eindhoven University of Technology.

Dibbern, H.C., Olesen, P., Rostrup-Nielsen, J.R., Tottrup, P.B., Udengaard P.B., 1986, Make low hydrogen/carbon monoxide syngas using sulfur passivated reforming, Hydrocarbon Process 1 71.

Dresselhaus, M.S., Dresselhaus, G., Saito, R., Jorio, A., 2004, Raman spectroscopy of carbon nanotubes, Physics reports.

Fei, J., Hou, Z., Zheng, X., Yashima, T., 2004, Doped Ni catalysts for methane reforming with CO_2, Catalysis Letters Vol. 98, No. 4.

Frank, S., Poncharal, P., Wang, Z.L., Heer, W.A., 1998, Carbon nanotube quantum resistors, Science 280, 1744–6.

Gadalla, A.M., Bower, B., 1988, The role of catalyst support on the activity of nickel for reforming methane with carbon dioxide, Chem. Eng. Sci. 43 3049.

Gadalla, A. M., Sommer, M. E., 1989, Carbon dioxide reforming of methane on nickel catalysts, Chem Eng. Sci., *44*, 2825.

He, C., Zhao, N., Shi, C., Du, X., Li, J., 2006, Carbon nanotubes and onions from methane decomposition using Ni/Al catalysts, Materials Chemistry and Physics 97 109–115.

Hester, J. R., Louchev, O. A., 2002, Nanoparticle-templated carbon nanotube ring nucleus formation, Appl. Phys. Lett. 80, 2580.

Hinshelwood, C. N., 1927, Proc. R. Soc. London, Ser. A 113, 230.

Hoffman, W. P., 2005, Material Science of Carbon, Air Force Research Laboratory, Edwards, CA, USA.

Hone, J., Whitney, M., Piskoti, C., Zettl, A., 1999, Thermal conductivity of singlewalled carbon nanotubes, Phys Rev B 59(4).

Hou, Z., Zheng, X., Yashima, T., 2005, High coke-resistance of K-Ca-promoted Ni/α-Al_2O_3 catalyst for CH_4 reforming with CO_2, React. Kinet. Catal. Lett. Vol. 84, No. 2, 229-235.

Iijima, S., 1991, Helical microtubules of graphitic carbon, Letters to Nature.

Jorio, A., Saito, R., Hafner, J., Lieber, C., Hunter, M., McClure, T., Dresselhaus, G., Dresselhaus, M., 2001, Structural (*n*, *m*) Determination of Isolated Single-Wall Carbon Nanotubes by Resonant Raman Scattering, Phys. Rev. Lett. 86 1118.

Keidar, M., 2007, Factors affecting synthesis of single wall carbon nanotubes in arc discharge, Department of Aerospace Engineering, University of Michigan, Ann Arbor, MI 48109, USA.

Khedr, M.H., Bahgat, M., Nasr, M.I., Sedeek, 2007, E.K., CO_2 decomposition over freshly reduced nanocrystalline Fe_2O_3, Colloids and Surfaces A: Physicochem. Eng. Aspects 302 517–524.

Kuwana, K., Endo, H., Saito, K., Qian, D., Andrews, R., Grulke, E.A., 2005, Catalyst deactivation in CVD synthesis of carbon nanotubes, Carbon. Volume 43 253-260.

Li, Y., Wang, Y., Zhang, X., Mi, Z., 2008, Thermodynamic analysis of autothermal steam and CO_2 reforming of methane, International journal of hydrogen energy 33 2507-2514.

Lietzke, M. H., Mullins, C., 1981, The thermal decomposition of carbon dioxide, Journal of inorganic nuclear chemistry 43 1769 - 1771.

Liu, B.S., Au C.T., 2003, Carbon deposition and catalyst stability over La2NiO4/γ-Al2O3 during CO2 reforming of methane to syngas, Applied Catalysis A: General 244 181–195.

Lou, Z., Chen, Q., Wang, W., Zhang, Y., 2003, Synthesis of carbon nanotubes by reduction of carbon dioxide with metallic lithium, Carbon 41 3063 - 3074.

Louchev, O.A., Hester, J. R., 2003, Kinetic pathways of carbon nanotube nucleation from graphitic nanofragments, J. Appl. Phys. 94 2002.

Louchev, O. A., Sato, Y., Kanda, H., 2002, Mechanism of thermokinetical selection between carbon nanotube and fullerene-like nanoparticle formation,J. Appl. Phys. 91, 10074.

Louchev, O.A., Kanda, H., Rosen, A., Bolton, K., 2004, Thermal physics in carbon nanotube growth kinetics, Journal of chemical physics 121, 446-456.

Mc Bride, W.S., 2001, Synthesis of Carbon Nanotubes by Chemical Vapor Deposition (CVD), Williamsburg, Virginia.

Mc Crary, J.H., Mc Crary, G.E., Chubb, T.A., Nemecek, J.J., Simmons, D.E., 1982, Sol. Energy, 29, 141.

Murakami, Y., Miyauchi, Y., Chiashi, S., Maruyama, S., 2003, Direct synthesis of high-quality single-walled carbon nanotubes on silicon and quartz substrates, Chem. Phys. Lett. 377 49.

Philippe, R., Morançais, A., Corrias, M., Caussat, B., Kihn, Y., Kalck, P., Plee, D., Gaillard, P., Bernard, D., Serp, P., 2007, Catalytic Production of Carbon Nanotubes by Fluidized-Bed CVD, Chem. Vap. Deposition 13, 447–457.

Popov, V.N., 2004, Carbon nanotubes: properties and application, Materials Science and Engineering R 43 61–102.

Qian, W., Liu, T., Wang, Z., Wei, F., Li, Z., Luo, G., Li, Y., 2004, Production of hydrogen and carbon nanotubes from methane decomposition in a two-stage fluidized bed reactor, Applied Catalysis A: General 260 223–228.

Richardson, J.T., Paripatyadar S.A., 1990, CO_2 reforming of CH_4 with supported Rh, Appl. Catal. *61*, 293.

Rostrup-Nielsen, J.R., Back Hansen J.H., 1993, $C0_2$ reforming of methane over transition metals, J. Catal., 144, 38.

Saito, R., Dresselhaus, G., Dresselhaus, M., 2000, Trigonal warping effect of carbon nanotubes, Phys. Rev. B 6 2981.

Sandler, S. I., 2006, Chemical, Biochemical and Engineering Thermodynamics, John Wiley & Sons Inc.

Shibuta, Y., Elliot. J.A., 2006, A molecular dynamics study of the carbon-catalyst interaction energy for multi-scale modelling of single wall carbon nanotube growth, Chem. Phys. Letters 427, 365-370.

Swaan, H.M., Kroll, V.C.H., Martin, G.A., Mirodatos, C., 1994, Deactivation of supported nickel catalysts during reforming of methane by carbon dioxide, Catalysis Today 21 571-578.

Tokunaga, O., Osada, Y., Ogasawara, 1989, S., Fuel, 68, 990.

Vaezzadeh, M., Noruzifar, E., Atashzar, S.F., Vaedazeh, M., Ahmadi, M., 2005, Simulation of carbon nanotube growth at optimized temperature, Chem. Phys. Letters 419, 154-157.

Wildoer, J., Venema, L., Rinzler, A., Smalley, R., Dekker, C., 1998, Electronic structure of atomically resolved carbon nanotubes, Nature 391 59.

Xu, X., Huang, S., 2007, Carbon dioxide as a carbon source for synthesis of carbon nanotubes by chemical vapor deposition, materials letters 61 4235 - 4237.

Zhao, N., Cui, Q., He, C., Shi, C., Li, J., Li, H., Du, X., 2007, Synthesis of carbon nanostructure with different morphologies by CVD of methane, Materials Science and Engineering A 460 – 461 255 - 260.

Zhang, C., Li, S., Wu, T., Peng Shao-Yi., 1999, Reduction of carbon dioxide into carbon by the active wustite and the mechanism of the reaction, Materials Chemistry and Physics 58 139 - 145

Zwaan, B., Gerlagh, R., 2006, Climate sensitivity uncertainty and the necessity to transform global energy supply, Energy 31 2571–2587.

Appendix 1: Mathcad calculations

Calculation 1

To find the equilibrium compositions during the reforming of methane with carbon dioxide equations 2.51, 2.52 and 2.53 are solved simultaneously in Mathcad as shown:

Ka =

600	645	690	735	780	825	870	915
7.59E+02	1.99E+02	6.16E+01	2.19E+01	8.69E+00	3.80E+00	1.80E+00	9.14E-01
4.83E-05	3.17E-04	1.64E-03	6.93E-03	2.49E-02	7.77E-02	2.16E-01	5.44E-01
1.04E-02	3.34E-02	9.29E-02	2.30E-01	5.18E-01	1.07E+00	2.07E+00	3.77E+00

960	1005	1050	1095	1140	1185	1230	1275
4.93E-01	2.80E-01	1.67E-01	1.03E-01	6.62E-02	4.39E-02	3.00E-02	2.10E-02
1.26E+00	2.69E+00	5.41E+00	1.03E+01	1.85E+01	3.19E+01	5.28E+01	8.42E+01
6.51E+00	1.07E+01	1.70E+01	2.59E+01	3.83E+01	5.51E+01	7.73E+01	1.06E+02

1320	1365	1410	1455	1500
1.50E-02	1.10E-02	8.23E-03	6.25E-03	4.83E-03
1.30E+02	1.95E+02	2.86E+02	4.08E+02	5.69E+02
1.42E+02	1.87E+02	2.43E+02	3.09E+02	3.89E+02

$Nico2 := 3$

$Nich4 := 4$

$X1 := 1$

$X2 := 1$

$X3 := 1$

$yh2o := 0.2$

$yco2 := 0.2$

$yco := 0.2$

$yh2 := 0.2$

$ych4 := 0.2$

$i := 20$

Given

$$yh2o = \frac{(2X1 - X2)}{(Nico2 + Nich4 - X1 + X2 + X3)} \qquad 1 > yh2o > 0$$

$$yco2 = \frac{(Nico2 - X1)}{(Nico2 + Nich4 - X1 + X2 + X3)} \qquad 1 > yco2 \geq 0$$

$$yco = \frac{(X2)}{(Nico2 + Nich4 - X1 + X2 + X3)} \qquad 1 > yco > 0$$

$$yh2 = \frac{(-2X1 + X2 + 2X3)}{(Nico2 + Nich4 - X1 + X2 + X3)} \qquad 1 > yh2 > 0$$

$$ych4 = \frac{(Nich4 - X3)}{(Nico2 + Nich4 - X1 + X2 + X3)} \qquad 1 > ych4 > 0$$

$$Ka_{1,i} = \frac{\left(yh2o^2\right)}{\left(yco2 \cdot yh2^2\right)} \qquad Nico2 - X1 \geq 0 \qquad X3 > 0$$

$$Nich4 - X3 \geq 0$$

$$Ka_{2,i} = \frac{(yco \cdot yh2)}{(yh2o)} \qquad X2 + 2X3 \geq X1$$

$$Ka_{3,i} = \frac{\left(yh2^2\right)}{(ych4)}$$

$$yh2o + yco2 + yco + yh2 + ych4 \leq 1$$

$$answer := Minerr(X1, X2, X3, yh2o, yco2, yco, yh2, ych4)$$

$$been := \left(answer_3 \;\; answer_4 \;\; answer_5 \;\; answer_6 \;\; answer_7\right)$$

$$been = \left(4.217\times 10^{-4} \;\; 1.199\times 10^{-4} \;\; 0.433 \;\; 0.554 \;\; 0.012\right)$$

$$\sum been = 1$$

Calculation 2

Equations 2.57 to 2.59 are solved using the following Matlab code:

$$Gibbs := \begin{pmatrix} 0 & 600 & 700 & 800 & 900 & 1000 & 1100 & 1200 & 1300 \\ 1 & -22690 & -12476 & -1993 & 8677 & 19475 & 30358 & 41294 & 52258 \\ 2 & -395152 & -395367 & -395558 & -395724 & -395865 & -395984 & -396081 & -396159 \\ 3 & -164480 & -173513 & -182494 & -191417 & -200281 & -209084 & -217829 & -226518 \\ 4 & 0 & 0 & 0 & 0 & 0 & 0 & 0 & 0 \\ 5 & -214008 & -208814 & -203501 & -198091 & -192603 & -187052 & -181450 & -175807 \\ 6 & 0 & 0 & 0 & 0 & 0 & 0 & 0 & 0 \end{pmatrix}$$

j

$$i \qquad v := \begin{pmatrix} -1 & 0 & 1 & -1 & 0 & -1 & 0 \\ -1 & -1 & 0 & 0 & 1 & 0 & 0 \\ 2 & 1 & -1 & 1 & -2 & 0 & 1 \\ 2 & -1 & -3 & 3 & 0 & 2 & 1 \\ 0 & 1 & 1 & -1 & 0 & 0 & -1 \\ 0 & 0 & 0 & 0 & 1 & 1 & -1 \end{pmatrix} \begin{matrix} CH_4 \\ CO_2 \\ CO \\ H_2 \\ H_2O \\ C \end{matrix}$$

$Temp := 750$ In Kelvin

$G00 := \text{linterp}\left(\left(Gibbs^T\right)^{\langle 0 \rangle}, \left(Gibbs^T\right)^{\langle 1 \rangle}, Temp\right)$

$G01 := \text{linterp}\left(\left(Gibbs^T\right)^{\langle 0 \rangle}, \left(Gibbs^T\right)^{\langle 2 \rangle}, Temp\right)$

$G02 := \text{linterp}\left(\left(Gibbs^T\right)^{\langle 0 \rangle}, \left(Gibbs^T\right)^{\langle 3 \rangle}, Temp\right)$

$G03 := \text{linterp}\left(\left(Gibbs^T\right)^{\langle 0 \rangle}, \left(Gibbs^T\right)^{\langle 4 \rangle}, Temp\right)$

$G04 := \text{linterp}\left(\left(Gibbs^T\right)^{\langle 0 \rangle}, \left(Gibbs^T\right)^{\langle 5 \rangle}, Temp\right)$

$G05 := \text{linterp}\left(\left(Gibbs^T\right)^{\langle 0 \rangle}, \left(Gibbs^T\right)^{\langle 6 \rangle}, Temp\right)$

$i := 0 .. 5$

$j := 0 .. 6$

$$gibbs := \begin{pmatrix} G00 \\ G01 \\ G02 \\ G03 \\ G04 \\ G05 \end{pmatrix} \qquad \varepsilon rec := \begin{pmatrix} 1 \\ 1 \\ 1 \\ 1 \\ 1 \\ 1 \\ 1 \end{pmatrix}$$

$Rconst := 8.314$

$Press := 1$

$Press0 := 1$

$$n := \begin{pmatrix} 1 \\ 1 \\ 0 \\ 0 \\ 0 \\ 0 \end{pmatrix} \qquad \begin{matrix} CH_4 \\ CO_2 \\ CO \\ H_2 \\ H_2O \\ C \end{matrix} \qquad y := \begin{pmatrix} 1 \\ 1 \\ 1 \\ 1 \\ 1 \\ 1 \end{pmatrix} \qquad Keq := \begin{pmatrix} 1 \\ 1 \\ 1 \\ 1 \\ 1 \\ 1 \\ 1 \end{pmatrix}$$

Given

$$y_0 = \frac{n_0 + \sum_j \left(v_{0,j}\, \varepsilon rec_j\right)}{\sum n + \sum_j \left[\left(\sum v^{\langle j \rangle}\right) \varepsilon rec_j\right]} \qquad y_0 > 0$$

$$y_1 = \frac{n_1 + \sum_j \left(v_{1,j}\, \varepsilon rec_j\right)}{\sum n + \sum_j \left[\left(\sum v^{\langle j \rangle}\right) \varepsilon rec_j\right]} \qquad y_1 > 0$$

$$y_2 = \frac{n_2 + \sum_j \left(v_{2,j}\, \varepsilon rec_j\right)}{\sum n + \sum_j \left[\left(\sum v^{\langle j \rangle}\right) \varepsilon rec_j\right]} \qquad y_2 > 0$$

$$y_3 = \frac{n_3 + \sum_j \left(v_{3,j}\, \varepsilon rec_j\right)}{\sum n + \sum_j \left[\left(\sum v^{\langle j \rangle}\right) \varepsilon rec_j\right]} \qquad y_3 > 0$$

$$y_4 = \frac{n_4 + \sum_j \left(v_{4,j}\, \varepsilon rec_j\right)}{\sum n + \sum_j \left[\left(\sum v^{\langle j \rangle}\right) \varepsilon rec_j\right]} \qquad y_4 > 0$$

$$y_5 = \frac{n_5 + \sum_j \left(v_{5,j}\, \varepsilon rec_j\right)}{\sum n + \sum_j \left[\left(\sum v^{\langle j \rangle}\right) \varepsilon rec_j\right]} \qquad y_5 > 0$$

$$Keq_0 = \exp\left[\frac{-\sum_i \left(v_{i,0}\, gibbs_i\right)}{Rconst \cdot Temp}\right]$$

$$Keq_1 = \exp\left[\frac{-\sum_i \left(v_{i,1}\, gibbs_i\right)}{Rconst \cdot Temp}\right]$$

$$Keq_2 = \exp\left[\frac{-\sum_i \left(v_{i,2}\, gibbs_i\right)}{Rconst \cdot Temp}\right]$$

$$Keq_3 = \exp\left[\frac{-\sum_i \left(v_{i,3}\, gibbs_i\right)}{Rconst \cdot Temp}\right]$$

$$Keq_4 = \exp\left[\frac{-\sum_i \left(v_{i,4}\, gibbs_i\right)}{Rconst \cdot Temp}\right]$$

$$Keq_5 = \exp\left[\frac{-\sum_i \left(v_{i,5}\, gibbs_i\right)}{Rconst \cdot Temp}\right]$$

$$Keq_6 = \exp\left[\frac{-\sum_i \left(v_{i,6}\, gibbs_i\right)}{Rconst \cdot Temp}\right]$$

$$\prod_i \left(y_i\right)^{v_{i,0}} = \left(\frac{Press}{Press0}\right)^{-\left(\sum v^{\langle 0 \rangle}\right)} \cdot Keq_0$$

$$\prod_i \left(y_i\right)^{v_{i,1}} = \left(\frac{Press}{Press0}\right)^{-\left(\sum v^{\langle 1 \rangle}\right)} \cdot Keq_1$$

$$\prod_i \left(y_i\right)^{v_{i,2}} = \left(\frac{Press}{Press0}\right)^{-\left(\sum v^{\langle 2 \rangle}\right)} \cdot Keq_2$$

$$\prod_i \left(y_i\right)^{v_{i,3}} = \left(\frac{Press}{Press0}\right)^{-\left(\sum v^{\langle 3 \rangle}\right)} \cdot Keq_3$$

$$\prod_i \left(y_i\right)^{v_{i,4}} = \left(\frac{Press}{Press0}\right)^{-\left(\sum v^{\langle 4 \rangle}\right)} \cdot Keq_4$$

$$\prod_i \left(y_i\right)^{v_{i,5}} = \left(\frac{Press}{Press0}\right)^{-\left(\sum v^{\langle 5\rangle}\right)} \cdot Keq_5$$

$$\prod_i \left(y_i\right)^{v_{i,6}} = \left(\frac{Press}{Press0}\right)^{-\left(\sum v^{\langle 6\rangle}\right)} \cdot Keq_6$$

$ans := Minerr(y, Keq, \varepsilon rec)$

$$ans_0 = \begin{pmatrix} 0.03 \\ 0.104 \\ 8.491\times 10^{-3} \\ 0.156 \\ 0.313 \\ 0.387 \end{pmatrix} \begin{matrix} CH_4 \\ CO_2 \\ CO \\ H_2 \\ H_2O \\ C \end{matrix}$$

$$ans_1 = \begin{pmatrix} 5.599\times 10^{-4} \\ 0.163 \\ 291.584 \\ 3.43\times 10^{-3} \\ 559.789 \\ 0.313 \\ 0.011 \end{pmatrix}$$

$$ans_2 = \begin{pmatrix} 1.479 \\ 0.323 \\ 1.16 \\ 0.257 \\ 1.195 \\ 0.309 \\ 0.043 \end{pmatrix}$$

Entropy Calculation:

$$\text{enthalpyF} := \begin{pmatrix} -74.87 \cdot 1000 \\ -393.51 \cdot 1000 \\ -110.53 \cdot 1000 \\ 0 \\ -241.826 \cdot 1000 \\ 0 \end{pmatrix} \quad \frac{\text{J}}{\text{mol}} \qquad \text{enthalpyF} = \begin{pmatrix} -7.487 \times 10^4 \\ -3.935 \times 10^5 \\ -1.105 \times 10^5 \\ 0 \\ -2.418 \times 10^5 \\ 0 \end{pmatrix}$$

$$\text{Enthalpy} := \begin{bmatrix} \text{enthalpyF}_0 + \int_{25}^{\text{Temp}} \frac{(5.34 + 0.0115 \cdot \text{T})}{0.23901}\, d\text{T} \\ \text{enthalpyF}_1 + \int_{25}^{\text{Temp}} \frac{\left(10.34 + 0.00274 \cdot \text{T} - \frac{195500}{\text{T}^2}\right)}{0.23901}\, d\text{T} \\ \text{enthalpyF}_2 + \int_{25}^{\text{Temp}} \frac{(6.60 + 0.00120 \cdot \text{T})}{0.23901}\, d\text{T} \\ \text{enthalpyF}_3 + \int_{25}^{\text{Temp}} \frac{(6.62 + 0.00081 \cdot \text{T})}{0.23901}\, d\text{T} \\ \text{enthalpyF}_4 + \int_{25}^{\text{Temp}} \frac{\left(8.22 + 0.00015 \cdot \text{T} + 0.00000134\text{T}^2\right)}{0.23901}\, d\text{T} \\ \text{enthalpyF}_5 + \int_{25}^{\text{Temp}} \frac{\left(2.673 + 0.002617\text{T} - \frac{116900}{\text{T}^2}\right)}{0.23901}\, d\text{T} \end{bmatrix} \begin{matrix} \text{CH}_4 \\ \text{CO}_2 \\ \text{CO} \\ \text{H}_2 \\ \text{H}_2\text{O} \\ \text{C} \end{matrix}$$

$$\text{Enthalpy} = \begin{pmatrix} -4.515 \times 10^4 \\ -3.906 \times 10^5 \\ -8.91 \times 10^4 \\ 2.103 \times 10^4 \\ -2.159 \times 10^5 \\ -7.728 \times 10^3 \end{pmatrix}$$

$$\text{reaction1} := \sum_i \left(v_{i,0} \cdot \text{Enthalpy}_i\right)$$

$$\text{reaction2} := \sum_i \left(v_{i,1} \cdot \text{Enthalpy}_i\right)$$

$$\text{reaction3} := \sum_i \left(v_{i,2} \cdot \text{Enthalpy}_i\right)$$

$$\text{reaction4} := \sum_i \left(v_{i,3} \cdot \text{Enthalpy}_i\right)$$

$$\text{reaction5} := \sum_i \left(v_{i,4} \cdot \text{Enthalpy}_i\right)$$

$$\text{reaction6} := \sum_i \left(v_{i,5} \cdot \text{Enthalpy}_i\right)$$

$$\text{reaction7} := \sum_i \left(v_{i,6} \cdot \text{Enthalpy}_i\right)$$

$$\text{reactEnthal} := \begin{pmatrix} \text{reaction1} \\ \text{reaction2} \\ \text{reaction3} \\ \text{reaction4} \\ \text{reaction5} \\ \text{reaction6} \\ \text{reaction7} \end{pmatrix}$$

$$\text{reactEnthal} = \begin{pmatrix} 2.996 \times 10^5 \\ 6.449 \times 10^4 \\ -2.351 \times 10^5 \\ 2.351 \times 10^5 \\ -2.201 \times 10^5 \\ 7.949 \times 10^4 \\ 1.556 \times 10^5 \end{pmatrix}$$

$$\sum \text{reactEnthal} = 3.791 \times 10^5$$

$$react1 := \sum_i \left(v_{i,0} \cdot gibbs_i\right)$$

$$react2 := \sum_i \left(v_{i,1} \cdot gibbs_i\right)$$

$$react3 := \sum_i \left(v_{i,2} \cdot gibbs_i\right)$$

$$react4 := \sum_i \left(v_{i,3} \cdot gibbs_i\right)$$

$$react5 := \sum_i \left(v_{i,4} \cdot gibbs_i\right)$$

$$react6 := \sum_i \left(v_{i,5} \cdot gibbs_i\right)$$

$$react7 := \sum_i \left(v_{i,6} \cdot gibbs_i\right)$$

$$reactgibbs := \begin{pmatrix} react1 \\ react2 \\ react3 \\ react4 \\ react5 \\ react6 \\ react7 \end{pmatrix} \qquad reactgibbs = \begin{pmatrix} 4.669 \times 10^4 \\ 1.13 \times 10^4 \\ -3.539 \times 10^4 \\ 3.539 \times 10^4 \\ -3.946 \times 10^4 \\ 7.234 \times 10^3 \\ 2.815 \times 10^4 \end{pmatrix}$$

$$\sum reactgibbs = 5.392 \times 10^4$$

$$\frac{\left(\sum reactEnthal - \sum reactgibbs\right)}{Temp} = 433.522$$

The entropy is positive

The second law of modern thermodynamics states that entropy production of a system can never be negative and thus this means that the system described by this set of equations is thermodynamically viable.

Appendix 2: TEM Images

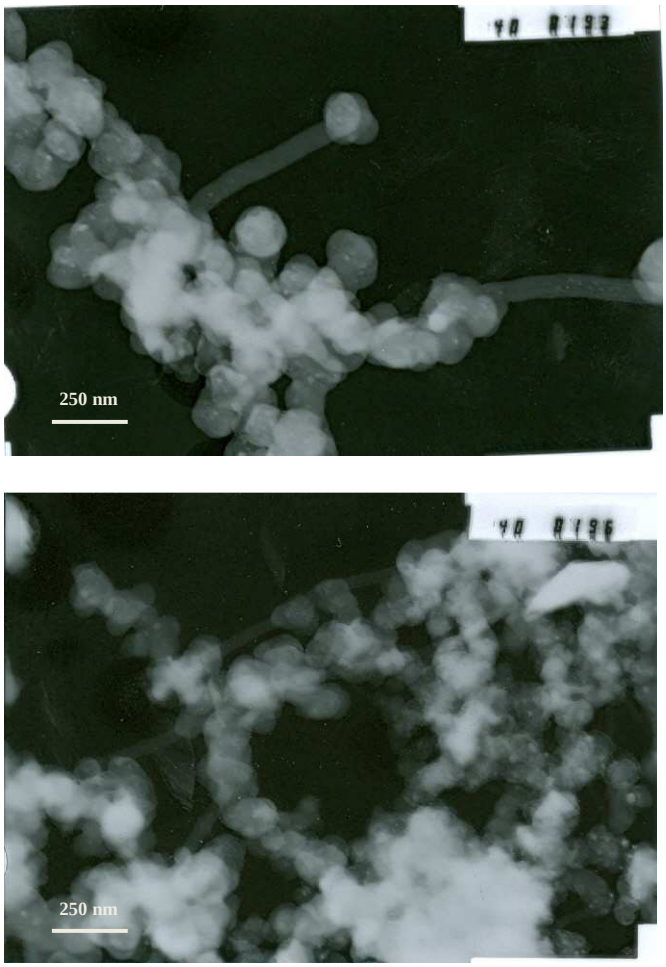

Figure 1: CNFs produced at 750°C using Lanthanum-Nickel catalyst.



Figure 2: CNFs produced at 850°C using Lanthanum-Nickel catalyst.

a) 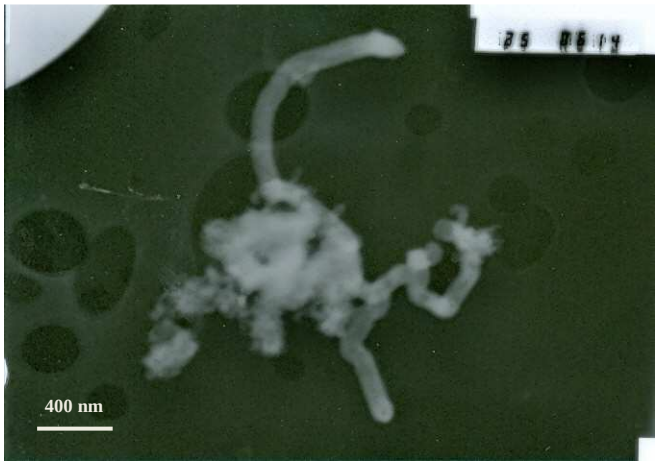

b) 

Figure 3: a) CNFs; b) possible CNT at 700°C using Lanthanum-Nickel catalyst.

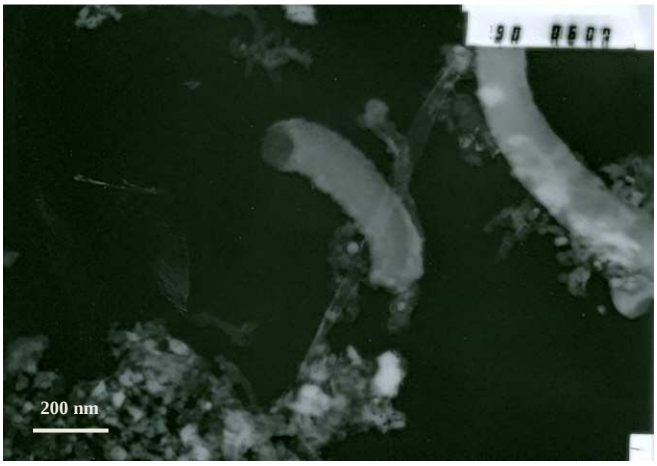

Figure 4: Hollow CNF produced at 800°C using Michmetal-Nickel catalyst.

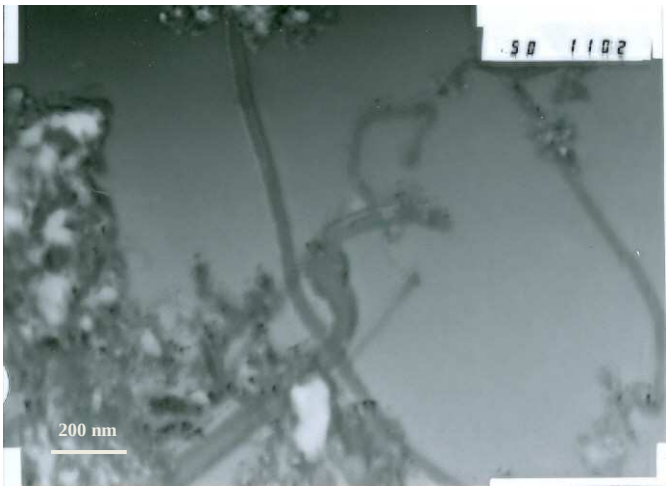

Figure 5: Very long CNTs produced at 750°C using Lanthanum-Nickel catalyst.

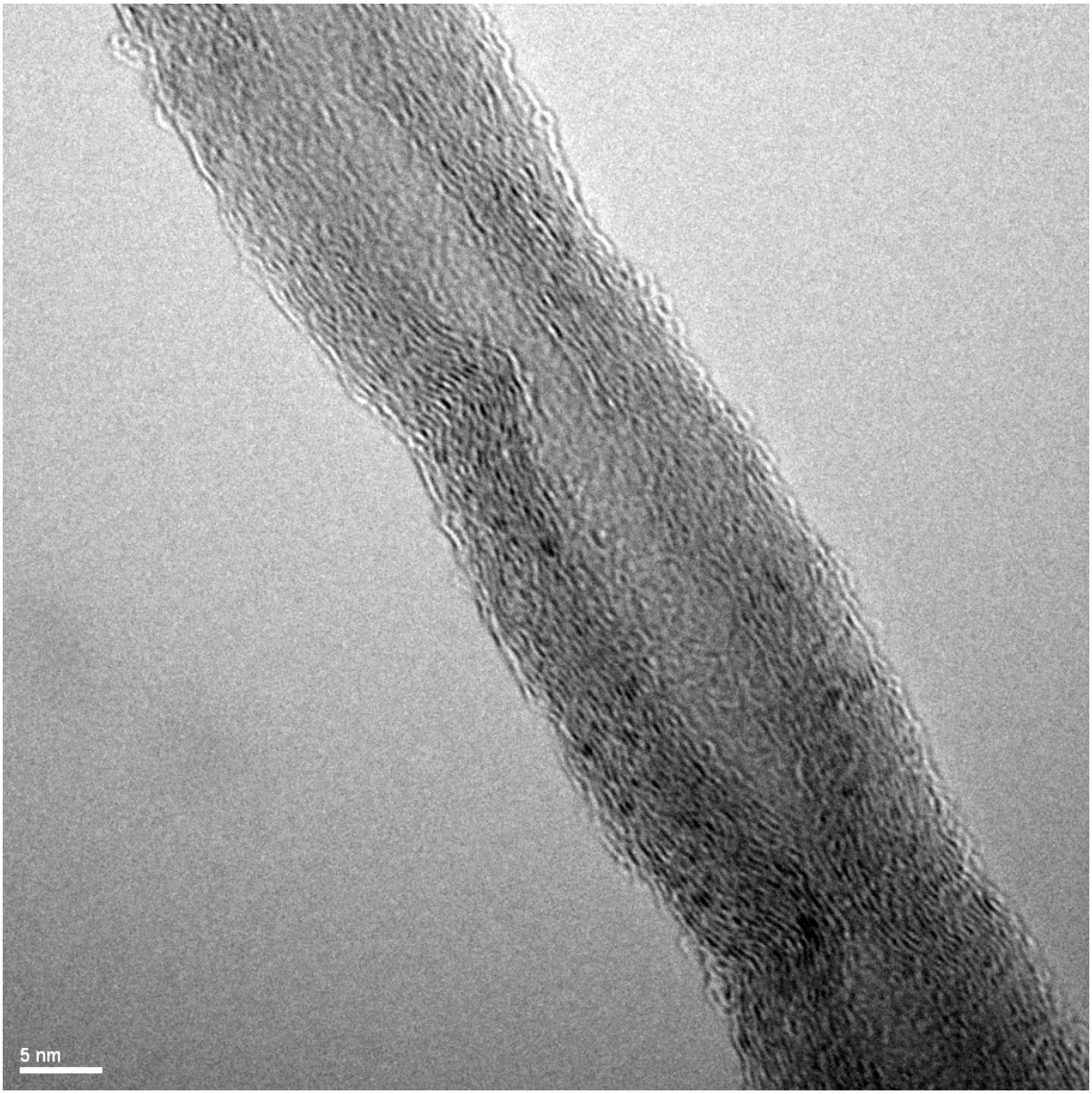

Figure 6: HRTEM image of CNTs produced in Figure 5 above.

a) 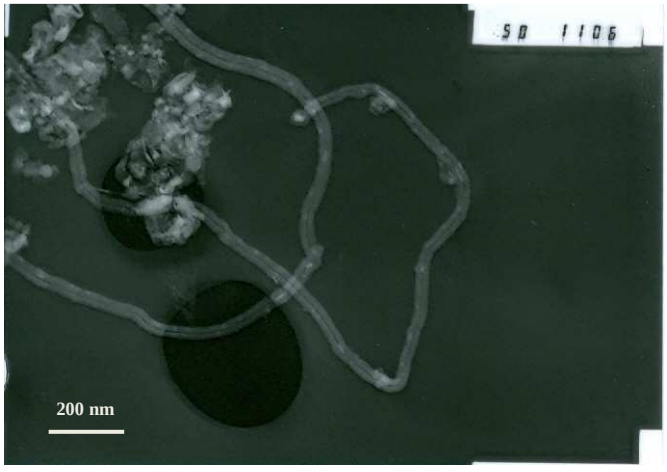

b) 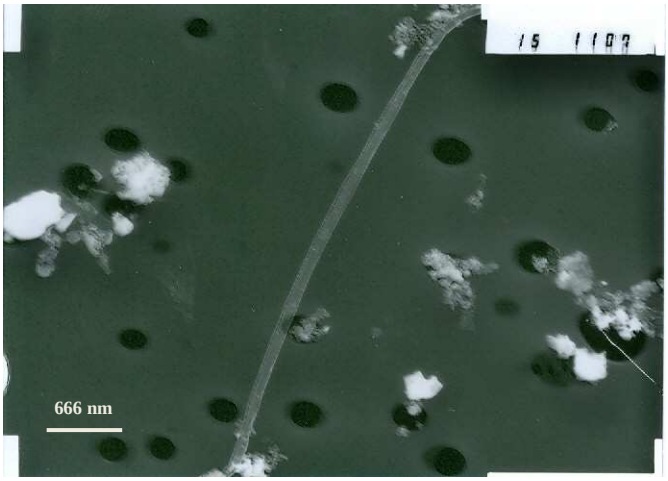

Figure 7: Long a) CNTs and b) CNF produced at 650°C using Lanthanum-Nickel.

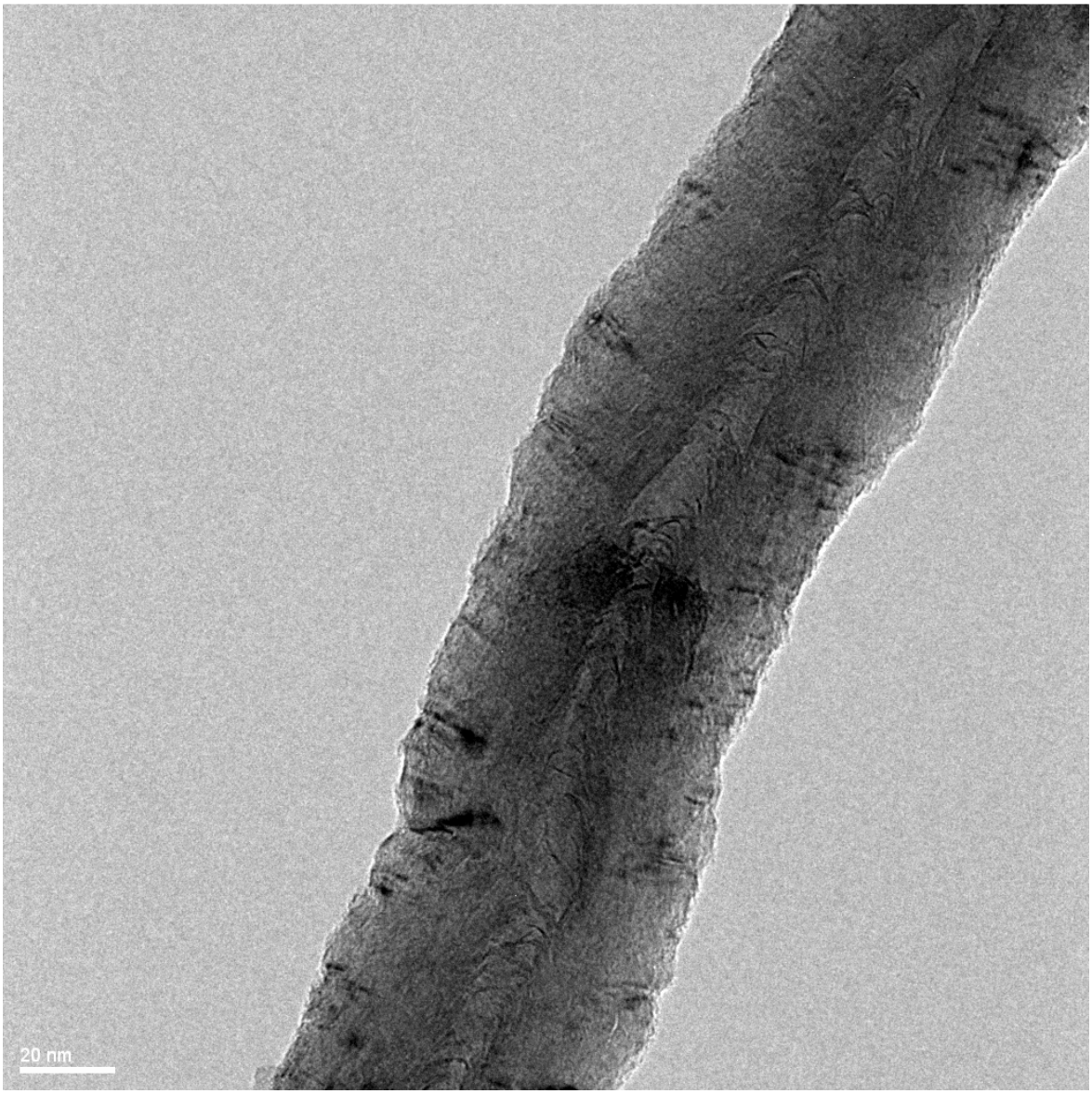

Figure 8: HRTEM image of CNT produced at 850°C using Lanthanum-Nickel alloy.

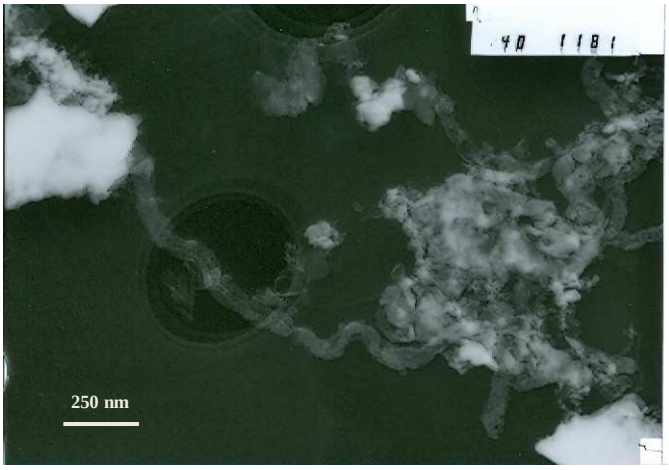

Figure 9: Disordered CNTs at 750°C during reforming with Lanthanum-Nickel.

a)
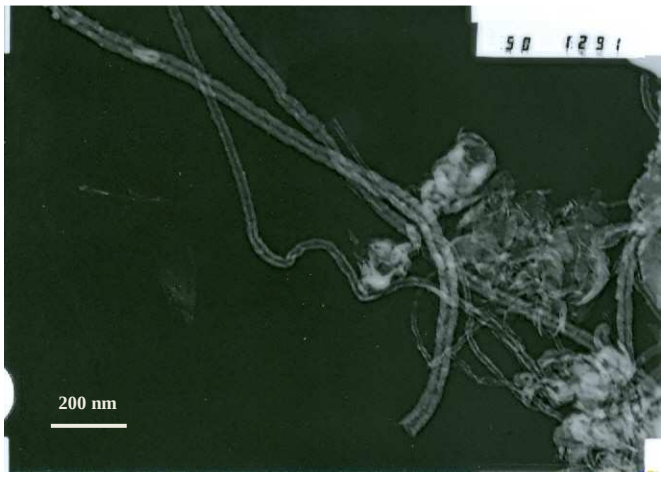

b)
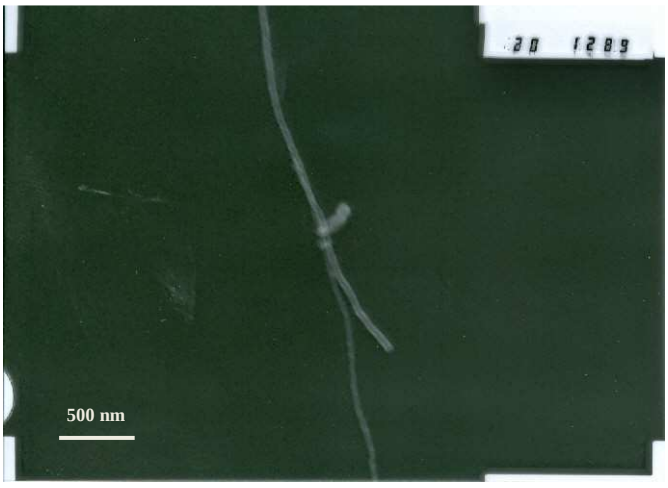

Figure 10: a) Network of CNTs b) a long CNT at 750°C during reforming with Mischmetal-Nickel.

Appendix 3: Raman Results

1)

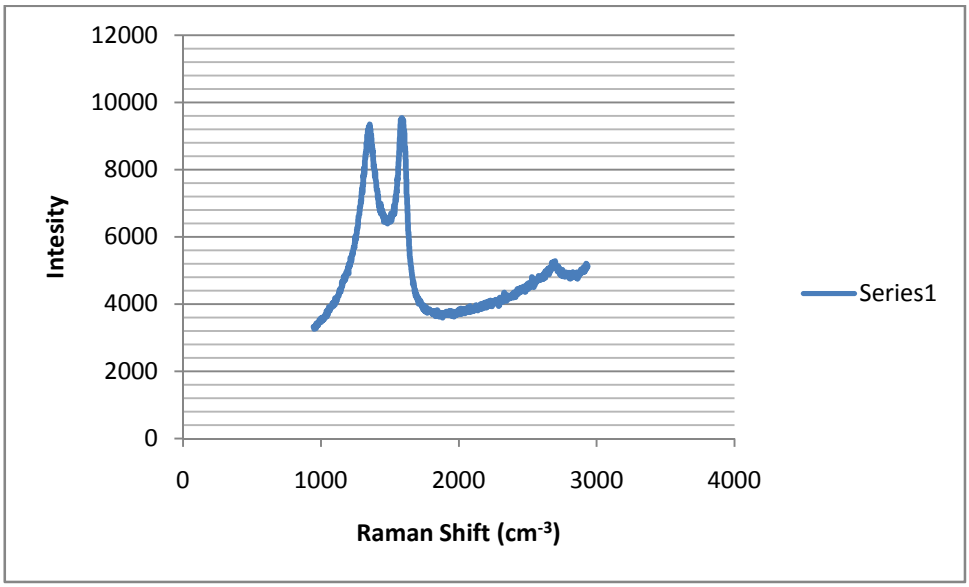

2)

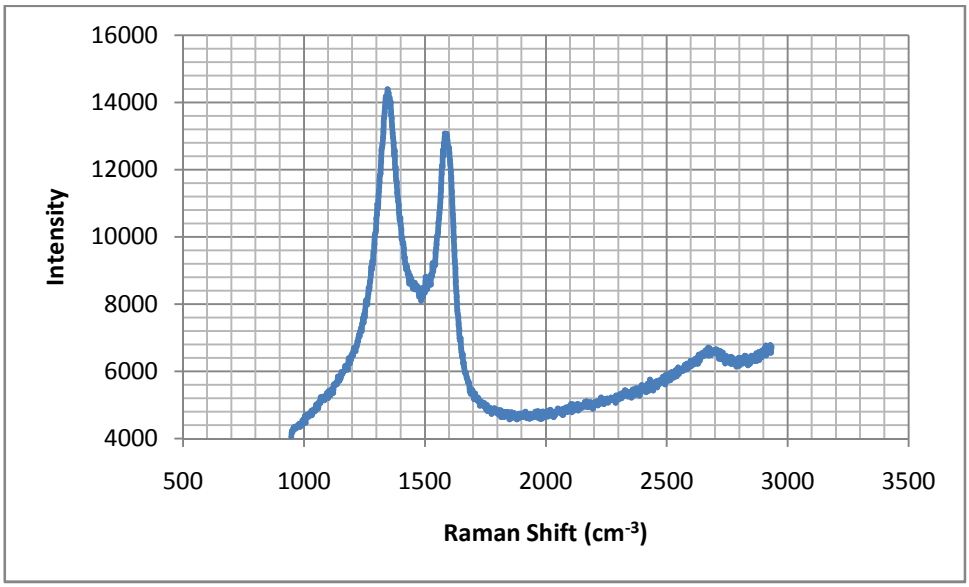

3)

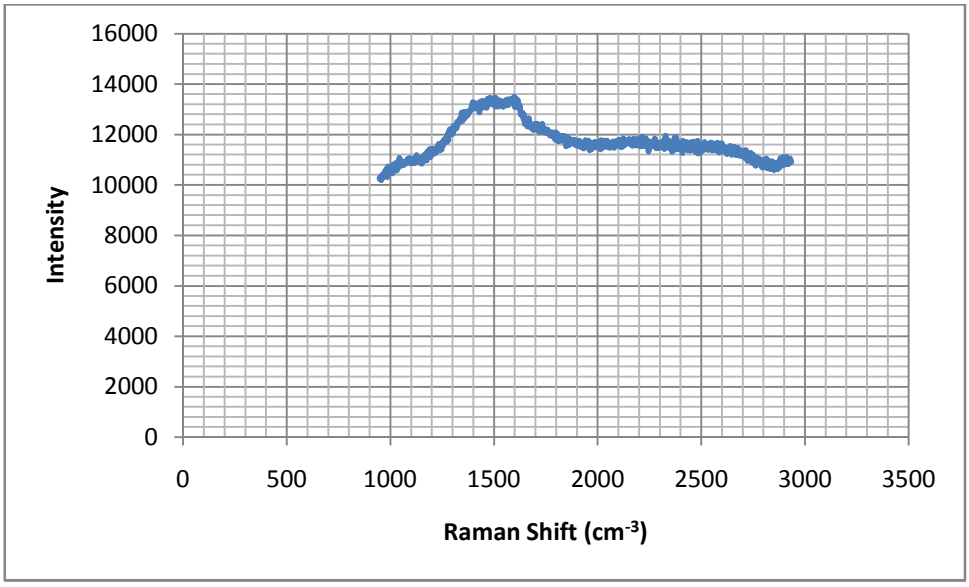
16000
14000
12000
10000
8000
6000
4000
2000
0
Intensity
0
500
1000
1500
2000
2500
3000
3500
Raman Shift (cm-3)

4)

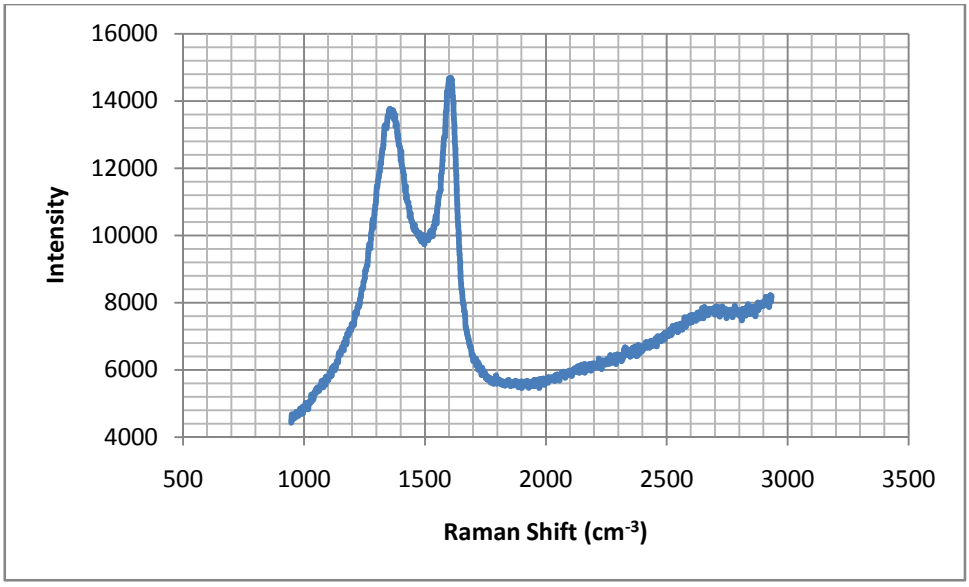
16000
14000
12000
10000
8000
6000
4000
Intensity
500
1000
1500
2000
2500
3000
3500
Raman Shift (cm-3)

5)

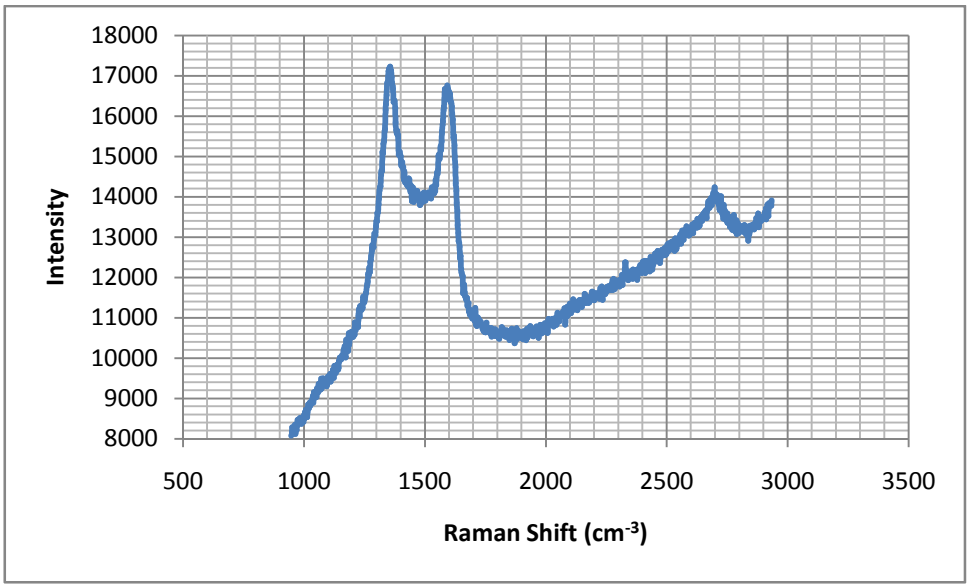
18000
17000
16000
15000
14000
13000
12000
11000
10000
9000
8000
Intensity
500
1000
1500
2000
2500
3000
3500
Raman Shift (cm-3)

6)

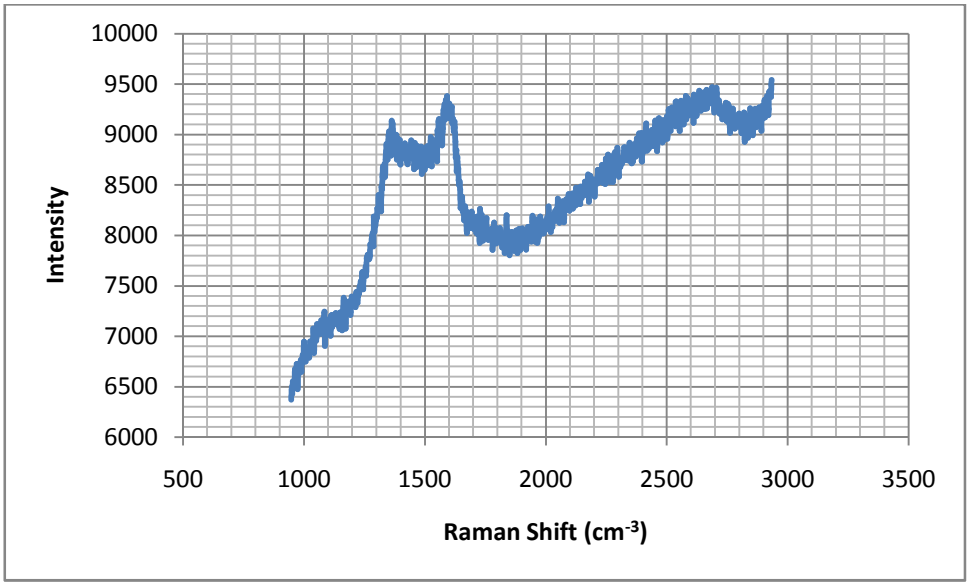
10000
9500
9000
8500
8000
7500
7000
6500
6000
Intensity
500
1000
1500
2000
2500
3000
3500
Raman Shift (cm-3)

7)

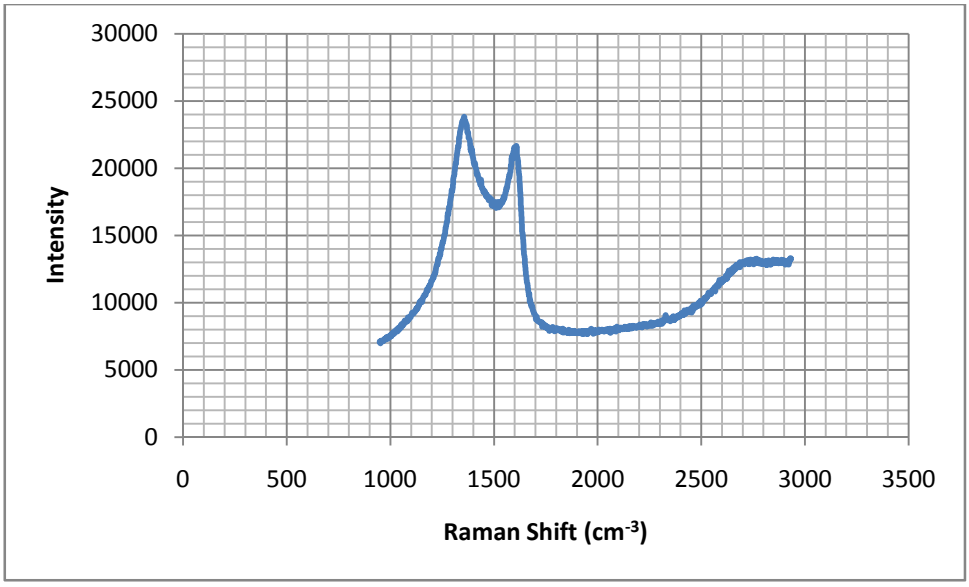
30000
25000
20000
15000
10000
5000
0
Intensity
0
500
1000
1500
2000
2500
3000
3500
Raman Shift (cm-3)

8)

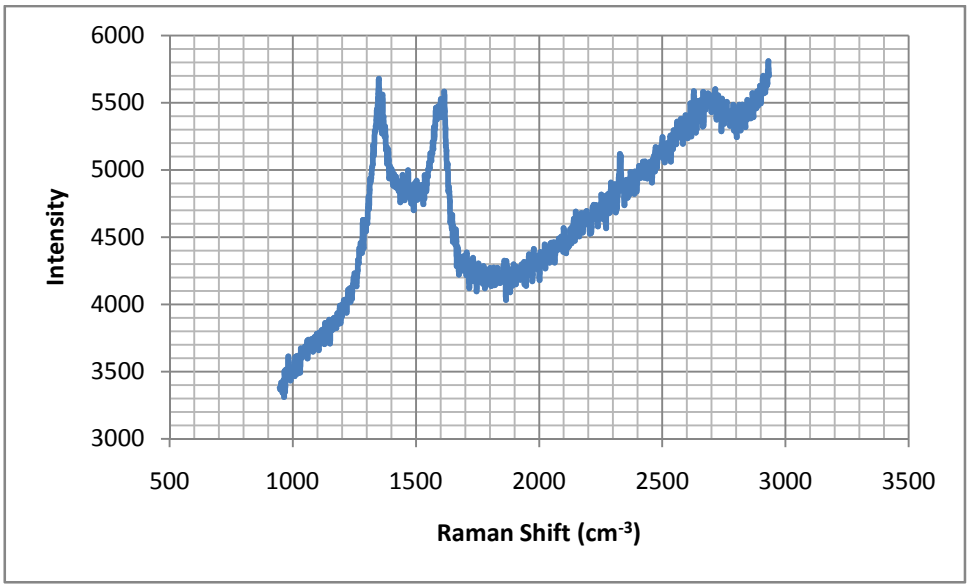
6000
5500
5000
4500
4000
3500
3000
Intensity
500
1000
1500
2000
2500
3000
3500
Raman Shift (cm-3)

9)

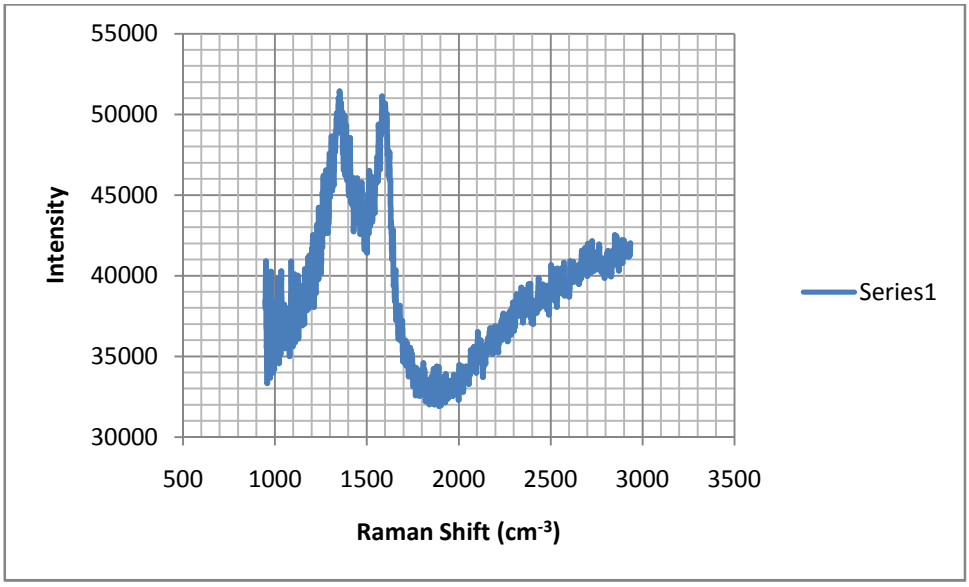
55000
50000
45000
40000
35000
30000
Intensity
500
1000
1500
2000
2500
3000
3500
Raman Shift (cm-3)
Series1

10)

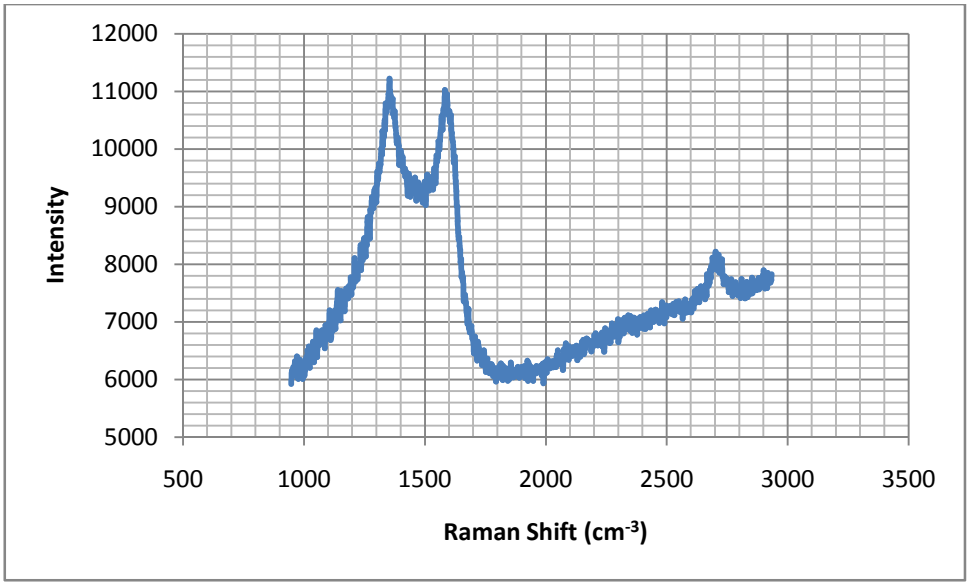
12000
11000
10000
9000
8000
7000
6000
5000
Intensity
500
1000
1500
2000
2500
3000
3500
Raman Shift (cm-3)

11)

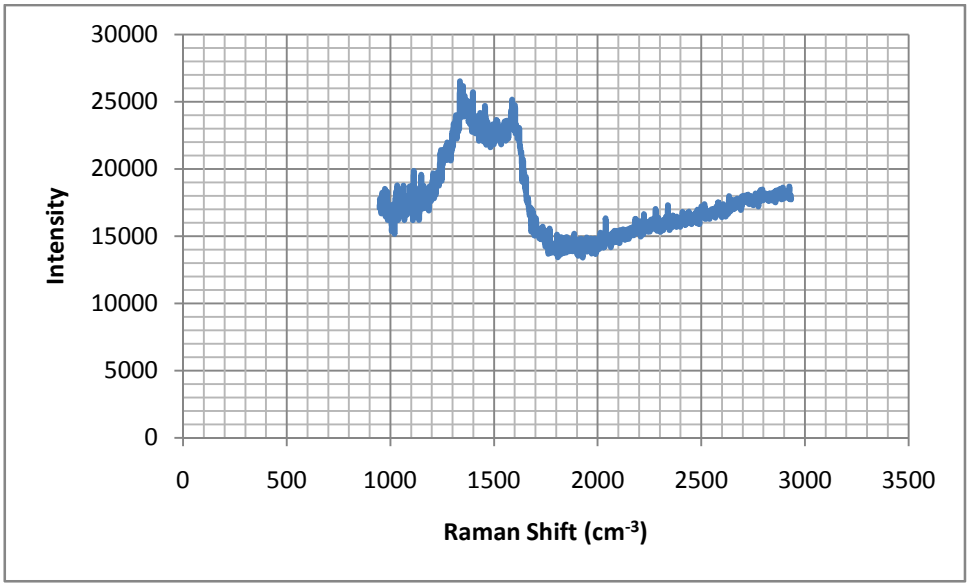
30000
25000
20000
15000
10000
5000
0
Intensity
0
500
1000
1500
2000
2500
3000
3500
Raman Shift (cm-3)

12)

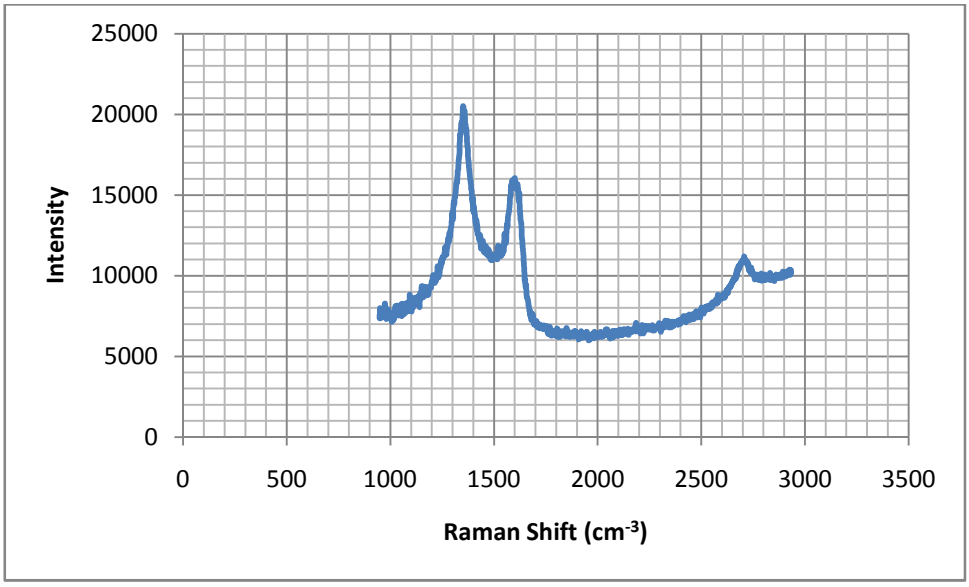

13)

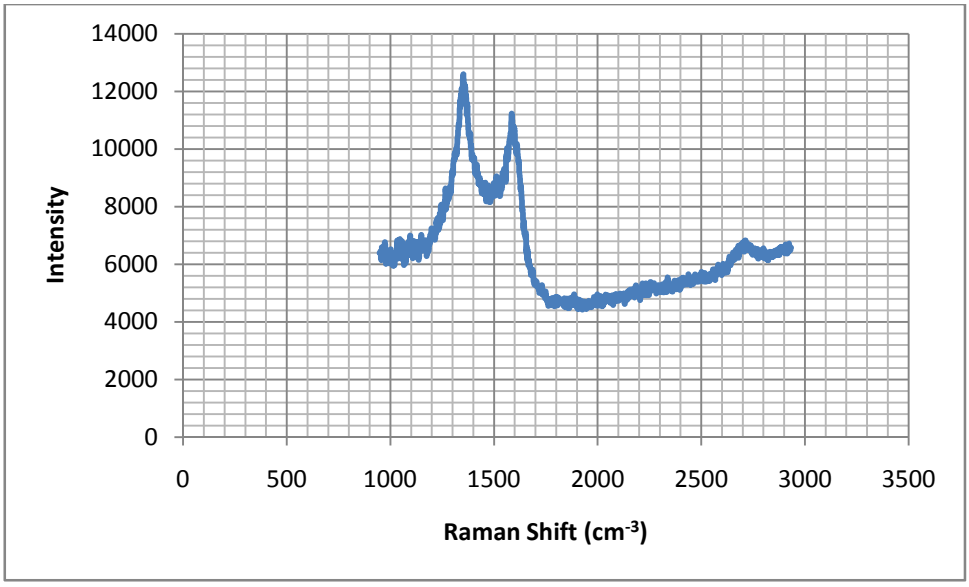

Table A. 1: Conditions at which the samples for the Raman spectrometer are produced.

No.	Gas	Catalyst	Temperature (^{o}C)	Sample tested
1	CO_2	$LaNi_5$	750	Carbon product
2	CO_2	$LaNi_5$	850	Carbon product
3	CO_2	$LaNi_5$	850	Catalyst particle
4	CO_2	1% Pt. on Alumina	750	Carbon Product
5	CO_2	$LaNi_5$	700	Carbon product

6	CO_2		$LaNi_5$	700	Catalyst particle
7	CO_2		Mischmetal-Nickel alloy	800	Carbon product
8	CO_2		Mischmetal-Nickel alloy	800	Catalyst particle
9	CH_4		$LaNi_5$	650	Carbon product
10	CH_4		$LaNi_5$	850	Carbon product
11	CH_4	&	$LaNi_5$	850	Carbon product
	CO_2				
12	CH_4	&	Mischmetal-Nickel alloy	750	Carbon product
	CO_2				
13	CH_4	&	Mischmetal-Nickel alloy	850	Carbon product
	CO_2				

Appendix 4: Data for Thermodynamic Plots

Table A. 2: Data for Figure 4.23(a)

T (K)	H2O	CO2	CO	H2	CH4
600	0.538	0.213	0.01	0.042	0.197
645	0.493	0.191	0.057	0.08	0.179
690	0.46	0.218	0.028	0.125	0.169
735	0.418	0.233	0.016	0.185	0.149
780	0.358	0.232	0.035	0.252	0.123
825	0.293	0.22	0.071	0.32	0.096
870	0.226	0.196	0.128	0.38	0.07
915	0.162	0.158	0.207	0.426	0.048
960	0.107	0.112	0.295	0.455	0.032
1005	0.065	0.069	0.374	0.471	0.021
1050	0.038	0.038	0.431	0.48	0.014
1095	0.022	0.02	0.464	0.485	0.009088
1140	0.013	0.011	0.476	0.494	0.006357
1185	0.007577	0.005116	0.487	0.496	0.004467
1230	0.004642	0.002465	0.496	0.494	0.00316
1275	0.002927	0.00166	0.497	0.496	0.002322
1320	0.001902	0.0009737	0.498	0.497	0.001738
1365	0.001271	0.0005917	0.499	0.498	0.001323
1410	0.0008709	0.0003713	0.5	0.498	0.001023
1455	0.000611	0.0002403	0.5	0.499	0.000804
1500	0.000438	0.0001596	0.5	0.499	0.00064

Table A. 3: Data for Figure 4.23(b)

T (K)	H2O	CO2	CO	H2	CH4
600	0.351	0.013	0.000159	0.11	0.525
645	0.315	0.029	0.000764	0.132	0.523
690	0.292	0.032	0.002301	0.208	0.466
735	0.263	0.035	0.006043	0.301	0.395
780	0.229	0.037	0.014	0.405	0.316
825	0.19	0.037	0.029	0.506	0.238
870	0.148	0.034	0.054	0.594	0.17
915	0.106	0.028	0.087	0.662	0.116
960	0.07	0.02	0.124	0.709	0.077
1005	0.045	0.014	0.168	0.724	0.049
1095	0.014	0.003237	0.187	0.772	0.023
1140	0.008174	0.001655	0.194	0.781	0.016
1185	0.004855	0.0008681	0.197	0.786	0.011
1230	0.002971	0.0004719	0.198	0.79	0.008078
1410	0.000557	0.00005961	0.2	0.796	0.003541
1500	0.00028	0.00002557	0.2	0.799	0.00117

Table A. 4: Data for Figure 4.23(c)

T	H2O	CO2	CO	H2	CH4
600	0.544	0.145	0.000525	0.052	0.258
645	0.505	0.155	0.00178	0.091	0.247
690	0.46	0.164	0.00521	0.145	0.226
735	0.416	0.164	0.013	0.22	0.187
780	0.349	0.171	0.03	0.286	0.163
825	0.287	0.163	0.061	0.365	0.124
915	0.159	0.118	0.179	0.483	0.062
960	0.105	0.084	0.255	0.516	0.041
1005	0.064	0.051	0.323	0.535	0.027
1050	0.037	0.029	0.373	0.538	0.024
1095	0.022	0.015	0.406	0.527	0.031
1140	0.012	0.007531	0.413	0.559	0.008144
1185	0.007439	0.003952	0.42	0.565	0.004103
1230	0.003415	0.038	0.37	0.582	0.006925
1275	0.002868	0.00122	0.426	0.567	0.003031
1320	0.001928	0.000741	0.451	0.489	0.057
1365	0.001245	0.000435	0.428	0.569	0.001727
1455	0.000596	-0.00031	0.429	0.569	0.001048
1500	0.000422	0.00012	0.433	0.554	0.012

Table A. 5: Data for Figure 4.22

Temperature	H2 fraction	CO fraction	C fraction
700	0.108	0.003045	0.404
750	0.156	0.008491	0.387
800	0.206	0.021	0.366
850	0.24	0.05	0.343
900	0.299	0.08	0.302
950	0.337	0.13	0.261
1000	0.409	0.183	0.238
1050	0.39	0.25	0.173
1100	0.405	0.305	0.133
1150	0.434	0.347	0.109
1200	0.447	0.382	0.085
1250	0.457	0.409	0.067
1300	0.465	0.429	0.053